Topological carbon materials: a new perspective

Preprint · August 2019

CITATIONS
0

READS
286

5 authors, including:

Yuan Ping Chen
Jiangsu University
115 PUBLICATIONS **1,995** CITATIONS
SEE PROFILE

Shengbai Zhang
Rensselaer Polytechnic Institute
244 PUBLICATIONS **7,914** CITATIONS
SEE PROFILE

Topological carbon materials: a new perspective

Yuanping Chen[1], Yuee Xie[1], Xiaohong Yan[1], Marvin L. Cohen[2], Shengbai Zhang[3]

[1] *Faculty of Science, Jiangsu University, Zhenjiang, 212013, Jiangsu, China*
[2]*Department of Physics, University of California at Berkeley, and Materials Sciences Division, Lawrence Berkeley National Laboratory, Berkeley, California, 94720, USA.*
[3]*Department of Physics, Applied Physics, and Astronomy Rensselaer Polytechnic Institute, Troy, New York, 12180, USA.*

Outline:

I. Introduction

Carbon, being one of the most abundant elements, has numerous one-dimensional (1D), two-dimensional (2D), and three-dimensional (3D) allotropic structures[1-3]. Although, graphite and diamond are the best known and studied carbon forms, in the past several decades, three other carbon forms, fullerenes[4], carbon nanotubes[5] and graphene[6], have become the focus of extensive research. Studies of these three carbon forms, have had a large impact on both scientific and industrial communities, and the search for new structures and applications continues[7-9]

Many important and unique properties of carbon can be attributed to its position in the Periodic Table. Each carbon atom has four valence electrons with an atomic configuration $2s^2 2p^2$. These four valence electrons can in principle be engaged in sp, sp^2 and sp^3 hybridizations to form a variety of allotropes or compounds with different bonding configurations[10]. For example, carbon can form triple bonds in the sp hybridization in graphyne, double bonds in the sp^2hybridization in graphene, and single bonds in the sp^3hybridization in diamond. Because of this rich hybridization capacity, the associated new structures, and the high potential for applications, the study of carbon materials has been a major focus of material science and condensed matter physics[11-13]

In the last decade, an active topic has emerged focusing on the topological behavior of electronic states[14-18]. Although many different phases of matter can be described well by the Landau symmetry-breaking theory where phase transitions can be traced back to changes in the order parameters going from one phase to another, phase transitions can occur without the breaking of symmetry for the phase. Many of these can be classified as topological phase transitions. A well-studied example is the topological insulator (TI)[19,20], in which the bulk solid is insulating while an edge (or surface) is conducting. Another class of materials of current interest is those featured by low-energy excitations with counterparts in high-energy physics, such as the low-energy excitations in Dirac (Weyl) semimetals[21-23]which behave just like the Dirac (Weyl) fermions. Since Lorentz symmetry is not guaranteed in condensed matter, there can be more types of fermions without counterparts in high-energy physics, and these new fermions bring new understanding to condensed matter physics[24,25]

The study on topological phases started with topological insulators (TIs), but recently it has been shifted to topological semimetals and metals (TMs)[22,26,27]. Comparing with the TIs, the TMs have additional types due to their complex topological Fermi surfaces, such as nodal points[28,29], nodal lines[30-32], and nodal surfaces[33]. All the topological phases can be characterized by some topological invariants such as Chern numbers in 2D Chern insulators[34,35], Z_2 indices in 2D and 3D topological insulators[36,37], topological charges in Weyl semimetal[38-40], and Z indices or winding numbers in topological nodal-line semimetals[41-44]. The topological invariants are usually protected by symmetries including time reversal (T), parity (P), or crystal symmetries[20,21,45]. The fundamental difference between a topological material and an ordinary material is the existence of topological states, e.g., topological surface states on the surfaces of 3D topological materials[46-48] and topological edge states on the edges of 2D materials[49-51]. The number of the topological surface/edge states are determined by the topological invariants.

At present, the study of topological physics in condensed matter often involves materials made of heavy elements to maximize spin orbit coupling (SOC))[27,52-55], which is often a prerequisite for experimentally measurable topological properties. In such materials, the time reversal operation satisfies $T^2 = -1$ [22,26]. Carbon is a counter-example. In fact, the first theoretically predicted TI is graphene[56]. However, research has since drifted away from carbon because the SOC in carbon is exceedingly small. It is well known that graphene is a Dirac semimetal[57,58], its lowest excitation is a Dirac fermion. Because of the exceptionally small SOC, on the other hand, one may treat the spin degree of freedom of graphene as a dummy variable. As such, the time reversal operation satisfies $T^2 = 1$[59]. In terms of the topological classification, the nontrivial phases in light-element materials are fundamentally different from those in heavy-element materials[60,61]. In particular, graphene should be viewed as a Weyl semimetal, instead of a Dirac semimetal. Previous studies have identified different classes of topological semimetallic carbon allotropes with Weyl points[62-67], nodal loops[68-75], and Weyl surfaces[76,77]

In this review, we first give a brief summary of the development of carbon allotropes from 1D to 3D. Next, we will discuss topological properties of carbon materials and their physical origin. Then, we will consider possible expansion of the topological study of carbon materials to other light-element

materials such as boron. Finally, we will present future prospects in pursue of topological physics within carbon allotropes.

II. Carbon structures: from one to three dimensions

In recent decades, with the development of nanotechnology, C_{60} fullerenes, carbon nanotubes, and graphene have been synthesized and have become one of the best-studied group of nanostructures[4-6]. Recently, 3D graphene networks have been proposed, and some of them, such as the carbon honeycomb[78], have been experimentally realized. With the rapid progress of science and technology in this area, it can be expected that more novel carbon materials will be realized in the foreseeable future. In the following, we will introduce typical carbon allotropes from one to three dimensions.

2.1 One dimension: polyacetylene

Polyacetylene: Based on a single-atom carbon chain, polyacetylene is one of the simplest 1D carbon systems[79]. Many 1D, 2D, and 3D carbon allotropes can be constructed by connecting polyacetylene[80-82], such as carbon nanotubes, graphene and 3D graphene networks.

Polyacetylene usually refers to an organic polymer with the repeating unit $(C_2H_2)_n$, as shown in Fig. 1. It is a long chain of carbon atoms with alternating single and double bonds between them and each carbon atom has one attached hydrogen atom. Polyacetylene may also be viewed as a polymerization of the acetylene molecules to yield a chain of repeating olefin groups. It is conceptually important, as the discovery of polyacetylene and its high conductivity upon doping helped the establishment of the field of organic conductive polymers[83]. The high electrical conductivity of polymers led to the use of organic compounds in microelectronics, which was recognized by the Nobel Prize in Chemistry in 2000[84].

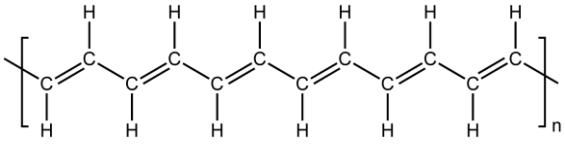

Figure 1. Atomic structure of polyacetylene.

Besides polyacetylene, there are other 1D carbon structures such as carbon threads[85], carbon

nanowires[86], graphene nanoribbons, and carbon nanotubes. The last two will be discussed later.

2.2 Two dimensions: graphene, graphyne and Kagome graphene

Graphene: Graphene is a 2D single-layer honeycomb nanosheet[87], as shown in Fig. 2(a). There is no doubt that it is one of the most important nanomaterials studied in the last several decades[88-92]. Graphene receives tremendous attention not only because it is one of the first 2D nanomaterials, but also because it possesses numerous astonishing physical and chemical properties, such as an ultrahigh electron mobility[93], a high mechanical strength[94], and a high thermal conductivity[95].

The first method used to obtain graphene is mechanical exfoliation with scotch tape[96]. The exfoliated graphene is of very high quality, but the above method is neither high-throughput nor high-yield. There have been numerous proposals to produce high-quality graphene with more efficient and scalable approaches[97-100]. Alternatives to the mechanical exfoliation may be classified into three categories: (i) chemical vapor deposition (CVD), such as the decomposition of ethylene on nickel surfaces[101], (ii) bottom-up methods to grow graphene directly from an organic precursor[102], and (iii) epitaxial growth on electrically insulating substrate such as SiC[103]. A thorough discussion of the various fabrication methods for graphene can be found elsewhere[104-106].

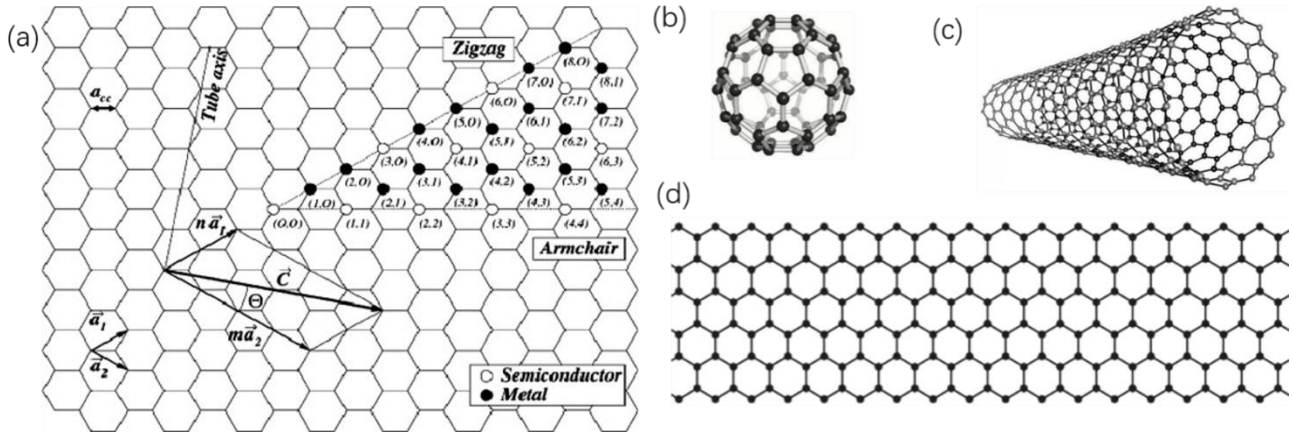

Figure 2. Graphene can be used to construct other carbon materials. (a) 2D graphene, (b) 0D fullerene, (c) 1D carbon nanotube, (d) 1D graphene nanoribbon. A 1D carbon nanotube can be obtained by rolling up a graphene along the vector $\boldsymbol{C} = n\boldsymbol{a}_1 + m\boldsymbol{a}_2$ ($\boldsymbol{a}_1$ and $\boldsymbol{a}_2$ are unit vectors).

The uniqueness of graphene in the family of carbon allotropes is that it may be viewed as the parent material from which many other carbon structures can be constructed[107-112]. For example, it can

be stacked to produce 3D graphite, rolled into a 1D carbon nanotubes [Fig. 2(b)], or wrapped to construct a 0D fullerenes [Fig. 2(c)]. Moreover, graphene can be tailored and lithographed into desired patterns[113,114].

By cutting graphene along certain directions, **1D graphene nanoribbons (GNRs)** with different edges are obtained, such as armchair-edged and zigzag-edged nanoribbons[115-118]. Figure 2(d) shows a zigzag-edged nanoribbon. The properties of GNRs can range from metallic to semiconducting according to the widths and edges. Zigzag-edged GNRs are metallic with peculiar edge states on both sides of the ribbon regardless of its widths, while the armchair-edged GNRs can be either metallic or semiconducting. An armchair-edged GNR with width $N_A = 3i+2$ (i is an integer) is metallic; otherwise it is a semiconductor. Numerous approaches have been reported to produce GNRs with various chemicophysical properties[119-122].

By rolling up a graphene, a **1D carbon nanotube** is obtained. Depending on the way the rolling is performed, there can be three different types of carbon nanotubes such as the non-chiral armchair and zigzag nanotubes and chiral nanotubes[123,124]. Usually a pair of indices (n, m) are used to describe the chiral vector $\mathbf{C} = n\boldsymbol{a_1}+m\boldsymbol{a_2}$ (where $\boldsymbol{a_1}$ *and* $\boldsymbol{a_2}$ *are unit vectors*) for a nanotube [see Fig. 2(a)][125-127]. When $m = 0$, the chiral nanotube is reduced to a zigzag nanotube, while when $n = m$, it is reduced to an armchair nanotube. According to the number of graphic layers, a nanotube can be further classified as a single-wall or multi-wall nanotube[128,129]. Figure 2(c) shows, as an example, a single-wall nanotube with a zigzag edge. Electrical conductivity of a nanotube depends on its chiral vector but is independent of its length, as determined by quantum mechanics[130-132]. All armchair and zigzag nanotubes with $n - m = 3i$ (where i is an integer) are metallic, while others are semiconducting. Carbon nanotubes show superior mechanical strength along the longitudinal direction, with the highest known tensile strength and elastic modulus among known materials[133-135]. They are also known to be the best field emitters due to their sharp tips, which can easily concentrate an electric field, enabling them to emit electrons at a low voltage[136,137]. The carbon nanotubes originally reported by Iijima were multi-wall nanotubes synthesized by arc discharge methods[138]. These days, CVD is the most promising method to produce carbon nanotubes on an industrial scale[123,139].

When two monolayer graphene are overlaid, a bilayer graphene is obtained[140-143]. There are

typically two stacking sequences between the two layers[144,145]: one is AA stacking, while the other is AB stacking. Although the interlayer coupling is van der Waals-type in nature, the interaction between the layers can have noticeable efforts on the atomic structure[145-148]. For example, the layer spacings of the AA- and AB-stackings are different. Beside the AA- and AB-stackings, bilayer graphene can have other interesting structures: in particular, different "moiré patterns" are observed, depending on the twist angle θ [149-152]. These patterns, especially those at small θ, reveal a number of exciting but also surprising physical phenomena such as novel superconductivity[153-156]. Hence, twisted bilayer graphene has been one of the most fascinating materials to study recently[157-166].

Graphyne: Graphyne is one-atom-thick planar sheets of sp and sp^2-bonded carbon atoms arranged in a crystal lattice[167]. The proposed structures of graphyne are constructed by inserting acetylene bonds in places of C-C polyacetylene single-bonds in a graphene lattice[168], see for example, the three types of graphyne in Fig. 3. There is a variety of possibilities due to the multiple arrangements of sp and sp^2 hybridized carbonatoms[67,169,170]. In addition, graphyne can be arranged either in a hexagonal or a rectangular lattice[171,172]. It has been shown theoretically that graphynes possess direction-dependent Dirac cones[168,173]. Among the graphynes with a rectangular lattice, the 6,6,12-graphyne may hold the most potential for applications[174,175]. To date, synthesized graphyne samples have shown to have a melting point of 250-300 °C[176] and a low reactivity in decomposition reactions with oxygen, heat, and light[177-180].

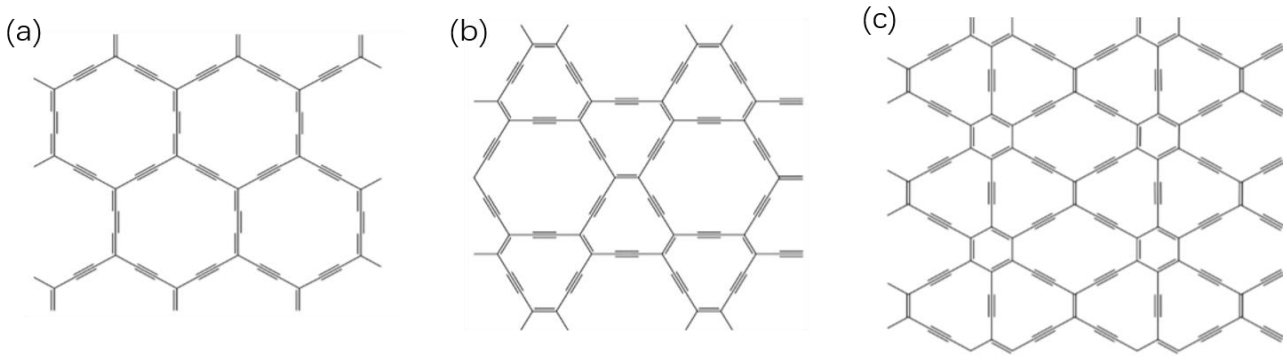

Figure 3. Three types of graphynes, (a) α-graphyne, (b) β-graphyne, and (c) 6,6,12-graphyne.

Kagome graphene[108]: Kagome graphene is a monolayer carbon sheet as shown in Fig. 4(a). It has twice as many atoms as a regular Kagome lattice. Should the bond length between two adjacent

different-colored atoms “shrinks” to zero, one recovers the regular Kagome lattice. By inserting acetylenic dimers between the neighboring triangles, a family of Kagome-like structures can be generated. For example, a Kagome graphyne containing one dimer between triangles is shown in Fig. 4(b).

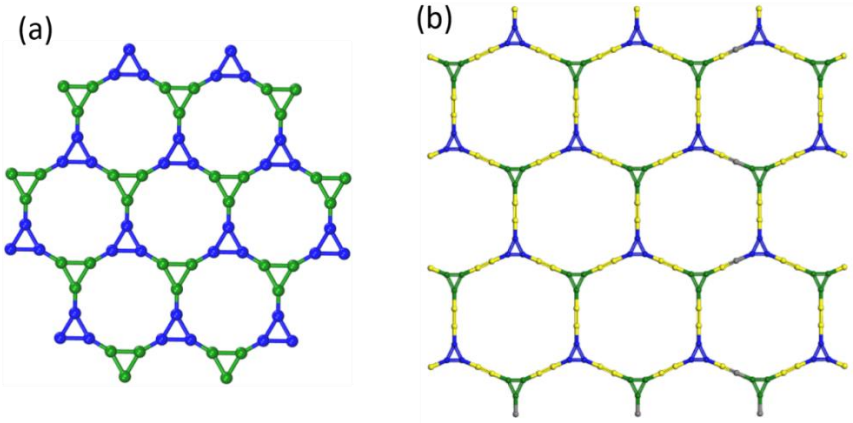

Figure 4. (a) Kagome graphene and (b) Kagome graphyne.

The lattice constant of the Kagome graphene is 5.19 Å. The bond length within a carbon triangle is 1.42 Å, while between the triangles is 1.35 Å. The former is very close to that of graphene, while the latter is between graphene and acetylene. Although the Kagome graphene contains carbon triangles, its calculated cohesive energy of 8.26 eV/atom is less than either α- or β-graphynes, 8.28 and 8.35 eV per carbon atom, respectively. Theoretical calculations indicate that the Kagome graphene and graphyne are all stable[108]. Although Kagome graphene has not been synthesized, a possible route for its experimental realization is proposed[108]. The elemental building unit of the triangular carbon rings of Kagome graphene already exists in laboratory as various cyclopropane molecules. One may thus tailor the ligand chemistry of the cyclopropanes to realize a self-assembly of the Kagome graphene. In terms of the choice of the substrate, the self-assembly process may be carried out on single-layer boron nitride sheet[108].

Graphene and Kagome graphene are made of hexagonal and triangular carbon rings, respectively. Beside the two structures, a lot of 2D carbon nanosheets, made of other (tetragonal and pentagonal) rings have also been proposed[181-186], such as T-graphene[186], penta-graphene, D-graphene and TPH-graphene. Some of them have been synthesized successfully.

2.3 Three dimension: graphene networks and carbon foams

Earlier carbon materials known in literature are 3D carbon allotropes, such as naturally occurring graphite and diamond[187,188]. Diamond crystalizes in a perfect tetrahedron structure consisting of sp^3 hybrids [Fig. 5(a)], while graphite crystalizes as a stacked graphene layers consisting of sp^2 hybrids [Fig. 5(b)]. The distinctly different atomic structures and local chemical bonding environments result in very different macroscopic appearance and physical properties between diamond and graphite[189,190]. Diamond is transparent, super hard and an ultimate abrasive, an electrical insulator, and a thermal conductor. In contrast, graphite is opaque, a very good lubricant, a good electrical conductor, and a thermal insulator. Besides, a lonsdaleite is a hexagonal allotrope of diamond, believed to form when meteoric graphite fall on to the Earth[191,192]. The great heat and stress of the impact transform the graphite into diamond, but retains its original graphite's hexagonal crystal lattice.

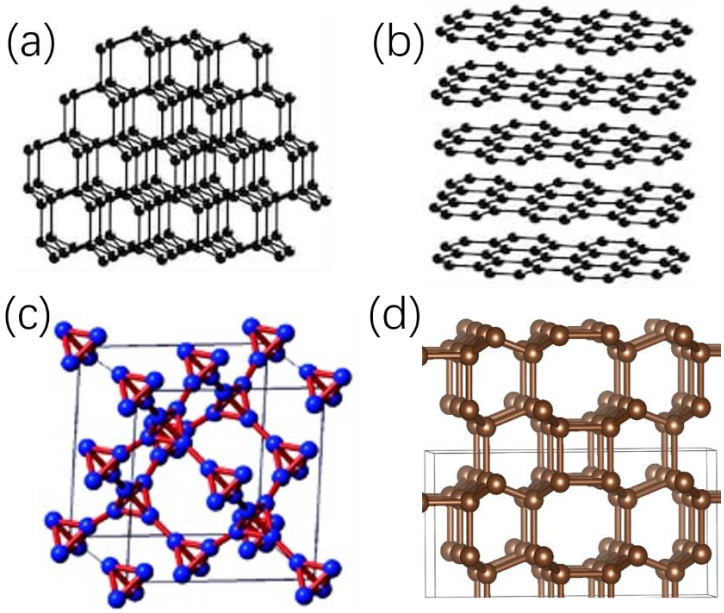

Figure 5. Atomic structures of some 3D carbon allotropes. (a) Diamond, (b) graphite, (c) T-carbon and (d) Z-carbon.

There are, however, also similarities between diamond and graphite. Noticeably, both are made of hexagonal carbon rings. While graphite is a 3D-stacked graphene layers bound by weak van der Waals interactions, diamond can also be viewed as an interlocked stacking of the graphene layers with intra-layer buckling due to the sp3 hybridization. Similar to the 2D structures, 3D carbon allotropes can also possess different types of carbon rings, such as the triangular, tetragonal, and pentagonal rings.

Based on this principle, a number of 3D carbon allotropes have been proposed[66,193-211]: for example, the T-carbon is made of triangular rings and tetrahedrons [Fig. 5(c)][201]; the Z-carbon is made of tetragonal and hexagonal rings [Fig. 5(d)][211]; the 3D pentagon carbon is made of pentagonal rings[202]; the M-, W-, H-, and S-carbons all contain some sort of distorted five and seven membered rings[203-205]. The diverse C-C bonding in these structures result in rich electronic, optical, and thermal properties[206-210].

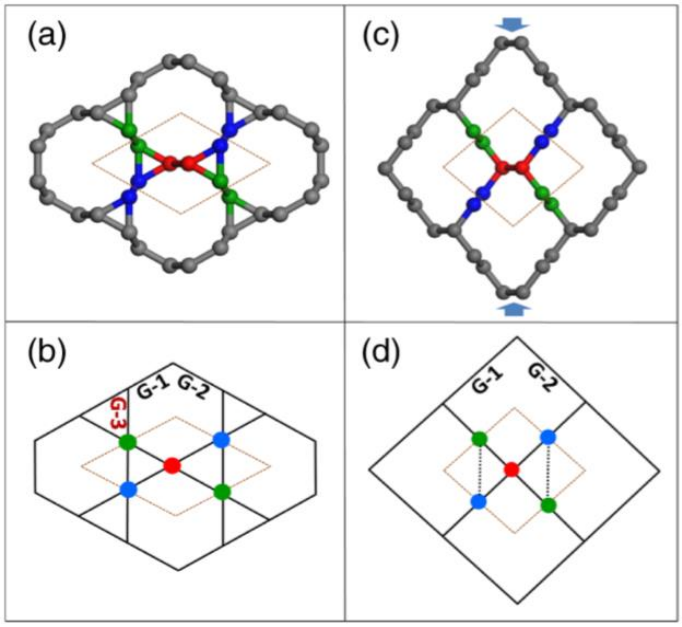

Figure 6. (a) CKL. The unit cell consists of six C atoms in the form of two linked triangles. Each pair of the (same color) atoms forms a zigzag chain in the vertical direction. (b) A schematic Kagome lattice for the CKL, where G-1, G-2, and G-3 denote three interlocked graphene sheets. Notice that each lattice point in the 2D structure here represents a zigzag chain in the perpendicular direction of the real structure. (c) and (d) Same plots for IGN. Notice the lack of G-3 in an IGN.

In all carbon allotropes, graphene is the most stable. Many more 3D carbon materials can be built out of graphene[198,204,211-217]. For example, Fig. 6(a) shows a structure formed by interpenetrating graphene layers[218]. When viewed from the top, the 3D network looks like a Kagome lattice, so it is named the carbon Kagome lattice (CKL). Its relation with the Kagome lattice is shown in Fig. 6(b). If one envisions that each infinitely long zigzag carbon chain in a CKL is collapsed to a 2D lattice point, then the two structures become identical. Although the structure consists of triangular rings (as can be seen from a top view), the CKL exhibits an exceptional stability similar to C_{60}. The reason is because the CKL is made of graphene sheets (as can be seen from a side view). A related structure is the

interpenetrated graphene networks (IGN) in Fig. 6(c)[62], which is also made of two sets of interlocked graphene sheets [see Fig. 6(d)]. One obtains the CKL from IGN by applying a compressive stress along the direction indicated by the arrows in Fig. 6(c) until the threefold coordinated sp^2 carbon atoms bind among themselves, so all the carbon bonds become sp^3.

The closely packed structures in Fig. 6 are in fact only the tip of the iceberg, as one can make a whole series of structures by replacing the colored dimers in the figure or a single row of zigzag carbon chains by GNRs of variable widths[78,219]. Here, (zigzag-edged or armchair-edged) GNRs are linked to each other either directly as in Fig. 6 or via a row of carbon atoms (see below). Figure 7 shows three carbon networks where two kinds of zigzag-edged GNRs of m rows (green) and n rows (purple) are linked together directly[219]. They have been classified as a triangular graphene network (TGN) [Fig. 7(a)], a quadrilateral graphene network (QGN) [Fig. 7(b)], and a hexagonal graphene network (HGN) [Fig. 7(c)]. By changing the widths of green and purple nanoribbons, one arrives at three families of graphene networks, TGN(m,n), QGN(m,n), and HGN(m,n).

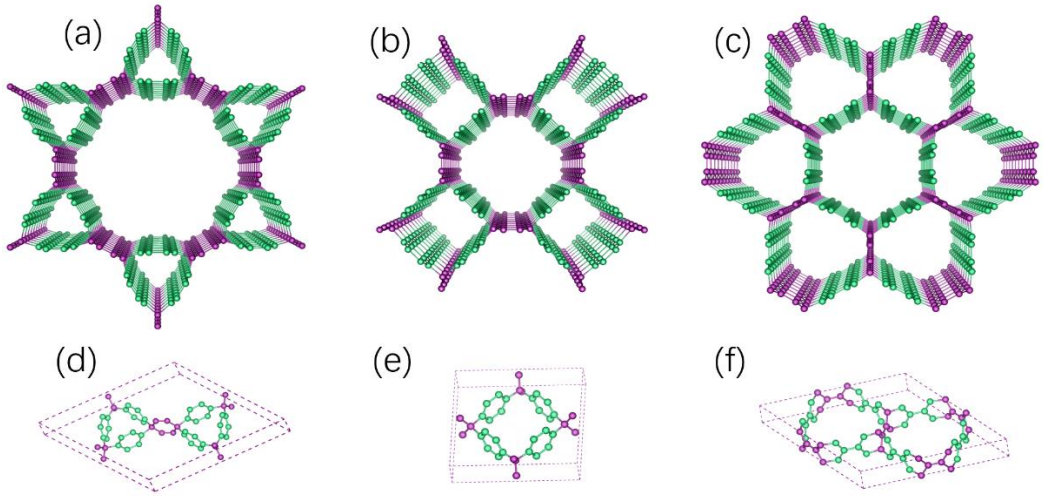

Figure 7. Graphene networks made of zigzag-edged GNRs: TGN(2,2), QGN(2,2), and HGN(2,2), by a direct link. (a-c) Top views of the networks and (d-f) tilted views of the corresponding unit cells.

The family of carbon honeycomb (CHC) represents 3D networks where the zigzag-edged nanoribbons are connected by a row of joint carbon atoms or dimers. From the top view, these structures look like honeycombs, as can been seen in Fig. 8(a). Here, again we use different colors to denote different carbon atoms: e.g., green and blue denote C1atoms with a sp^2 electronic configuration, while orange denotes the joint C2 atoms. The C1 atoms can be further divided into two subgroups, i.e.,

green and blue; together they form the zigzag chains along the c axis, while each subgroup resides on a different horizontal plane [see Figs. 8(b-c)]. The C2 atoms may form dimers to become sp^3 or remain un-dimerized and are hence sp^2. The former is termed CHC-*1*with the primitive cell shown in Fig. 8(b), while the latter is termed CHC-*1'* with a 2x primitive cell shown in Fig. 8(c) for comparison. Similar to CKLs and IGNs, one can increase the width of the nanoribbons from $n = 1$ to CHC-*n* with $n > 1$.

Krainyukova and Zubarev obtained CHC in 2016 by a deposition of vacuum-sublimated graphite where carbon was evaporated in vacuum from thin carbon rods heated by an electric current[220]. The carbon films obtained have a thickness in the range of 80-100Å. They were analyzed by means of transmission electron microscopy (TEM) [see Fig. 8(d) (left)] and low temperature high energy electron diffraction. The authors claimed that a careful and thorough analysis excludes carbon nanotubes and other carbon forms, so the only possibility is the carbon honeycomb shown in Fig. 8(d) (right). To our knowledge, this is perhaps the first experimental highly-ordered 3D carbon network made of predominantly graphene nanoribbons. With future technological improvements, we believe the theoretically-predicted carbon structures such as those in Figs. 4-7 will also be realized in the future.

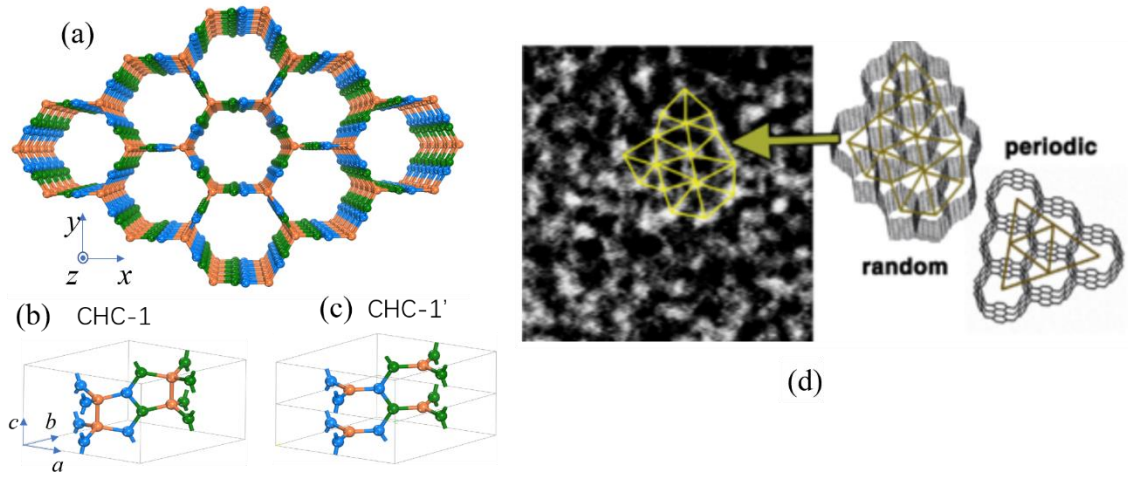

Figure 8. Carbon honeycombs. (a-c) Atomic structures: (a) CHC-1 in a top-view perspective, where the carbon atoms form a 3D honeycomb. (b) Primitive cell of CHC-1 in a side view perspective, where the green C1 and blue C1 atoms reside on different horizontal planes with respect to the c axis. Each kind of C1 atoms has a threefold rotational symmetry with respect to the axes passing through the orange connecting C2 dimers. In (a) and (b), t_0 to t_5 are the tight-binding hopping parameters. (c) An alternative to CHC-1, namely, CHC-1' in a 1×1×2 supercell where the C2 dimerization has been lifted. (d) An experimentally synthesized CHC structure (left). Both random and ordered honeycomb structures (right) have been claimed.

Besides the graphene networks or carbon foams[78,221-232], other 3D carbon allotropes that have been proposed previously include the Mackay crystals[154,205,208,209,233-248].

III. Topological phases in general

The recent studies of topological properties of materials is one of the most active research areas currently in condensed matter physics[249,250]. Beginning with topological insulators and especially the more recent studies of topological semimetals/metals (TMs) have been the subjects of a great deal of research. TMs are characterized by a topologically stable Fermi surface originating from a crossing of energy bands. Band crossings of this kind can be associated with a topological number[251-255], which may depend on the symmetries responsible for enforcing or protecting the degeneracy at the band crossing. Based on the codimension of the band crossings, three types of topological phases have been proposed[26,256,257], i.e., nodal point, nodal line, and nodal surface. In the nodal-point semimetals, the conduction and valence bands cross each other at zero-dimensional (0D) discrete points[28,258-266], which include the Weyl point[258], triple point[262-264], Dirac point[259-261], and multifold-degeneracy points[266]. In the nodal-line semimetals[267-284], the band crossings form 1D lines in momentum space, instead of discrete points. Because lines can be deformed into many different shapes (e.g., a ring or a knot), there exist diverse topological phases for the nodal lines[263,285-300], such as nodal chains, nodal links, and Hopf chains, etc. In the third type of TMs, the band crossings form a 2D surface[77,301-305], where each point is a crossing point whose dispersions are linear along the surface normal direction. The nodal surfaces can also have many variations such as being planner or spherical.

TMs can exhibit a variety of different low-energy excitations which offer a new platform for fundamental studies of novel quasiparticles which differ from the known particles in high-energy physics[305-307]. Due to the nontrivial topology of bulk and surface electronic states, TMs are expected to exhibit some novel properties[43,308-312], such as nearly flat drumhead-like surface states[308], unusual magnetoresistance[311], and a chiral anomaly[312], which have attracted attention from both theoretical and experimental perspectives. Moreover, TMs are of broad interests due to their potential applications in

chemical catalysis[313,314], quantum computation[315,316], and spintronics[317-319], to name a few. In the following, we will introduce some typical topological phases.

3.1 Topological insulators

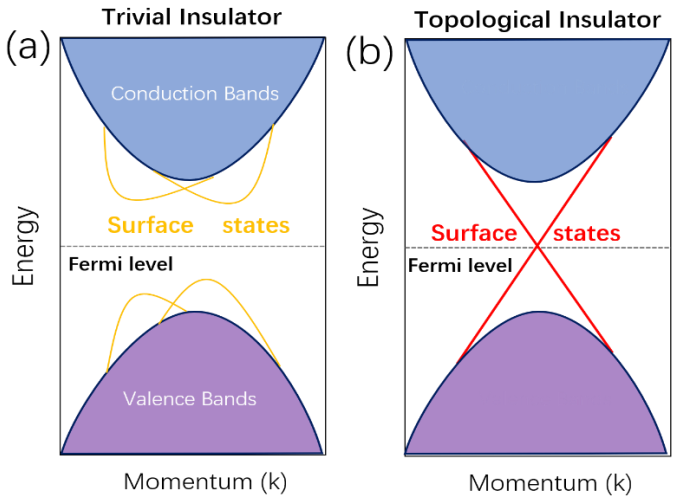

Figure 9. Comparison between (a) trivial insulator and (b) topological insulator. The surface states of trivial insulator are trivial, while those of topological insulator are protected by topological invariants.

A normal insulator has a fully occupied valence band and a fully empty conduction band, separated by a band gap. There is no state available for the conduction of electrons. Only the surface states of the insulator, see Fig. 9(a), can support such a conduction. A topological insulator is also an insulator. Similar to a normal insulator, electrons can only conduct through its surface states[18,320]. In spite of the similarities, however, there is an important difference: the conductive surface states in a TI is topologically-protected by its topological invariant to result in characteristic surface bands that continuously connect the bulk conduction with valence bands, as illustrated in Fig. 9(b)[321-323]. Due to such connections, the surface states of the TI are always conductive as they always pass the Fermi level. In contrast in a normal insulator, a sufficient surface modification can often eliminate the conductive surface states. According to the topological invariants, TIs can also be classified into a Z_2-index insulator and a Chern insulator[36,324].

3.2 Nodal-point TMs

As mentioned above, there are three classes of degenerate points in nodal-point semimetals. According to the band dispersions, these points can be further classified into type I and II[325-327].

Dirac point:

The Dirac point is the first-proposed topological element in TMs[327-334]. In a Dirac semimetal, the linear (conduction and valence) bands cross only at discrete (Dirac) point(s) of the Brillouin zone (BZ), at which the two bands have the same energy, i.e., doubly degenerate. In a 2D material, the energy dispersion near each of the critical points, according to the low-energy effective mass theory[11,335,336], takes the Dirac form, $H(\mathbf{k}) = v(k_x \sigma_x + k_y \sigma_y)$ where v is a velocity, $\boldsymbol{\sigma} = (\sigma_x, \sigma_y, \sigma_z)$ is the Pauli matrices. Note that these Dirac points are not robust, because a perturbation proportional to σ_z will inevitably open a band gap at the Dirac point.

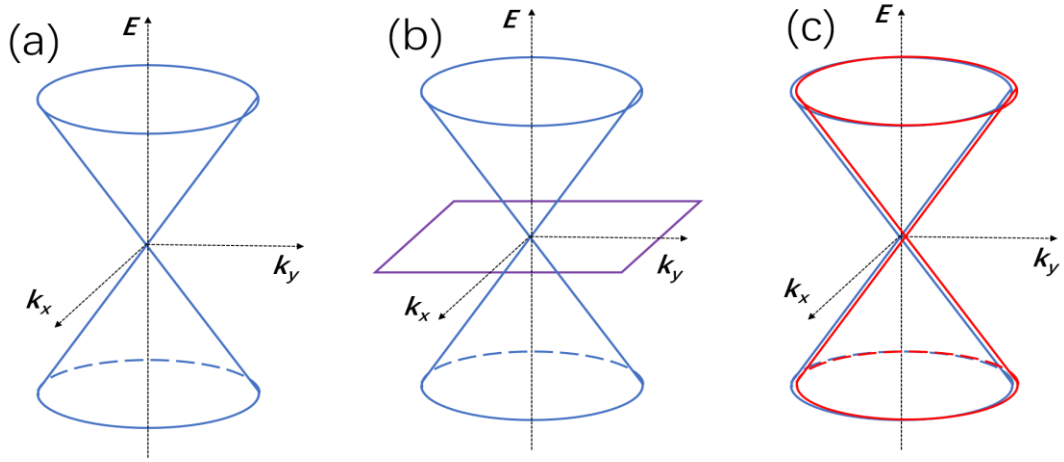

Figure 10. Three basic types of nodal points. (a) Weyl point, (b) triple point, and (c) Dirac point.

In 3D materials, the Dirac Hamiltonian can be expressed as a 4×4 matrix[115]:

$$H(\boldsymbol{k}) = v\boldsymbol{k}\cdot\boldsymbol{\sigma}\tau_x + m\tau_z = \begin{pmatrix} m & v\boldsymbol{k}\cdot\boldsymbol{\sigma} \\ v\boldsymbol{k}\cdot\boldsymbol{\sigma} & -m \end{pmatrix}, \quad (1)$$

where $\boldsymbol{k} = (k_x, k_y, k_z)$ is the momentum, and m is the mass; $\boldsymbol{\sigma}$ and $\boldsymbol{\tau} = (\tau_x, \tau_y, \tau_z)$ are both Pauli matrices. When the sign of m is changed, the topology of the ground state transitions from a normal insulator to a topological insulator. At the critical point of the transition ($m = 0$), the Hamiltonian is gapless at $\boldsymbol{k} = 0$, corresponding to a point node with fourfold-degeneracy and linear dispersion[337]. Therefore, a 3D Dirac semimetal exists at the transition between a topological and a normal insulator phase[25,244]. It is robust only when protected by an additional space-group symmetry[47,338-343]. Figure 10(c) shows the Dirac point for a massless Dirac equation. In most cases, however, the Dirac semimetal only acts as a parent state of a 3D topological insulator - it turns into either a 3D strong topological insulator or a 3D

topological crystalline insulator where the Dirac point acquires a mass gap, because of a symmetry breaking.

Weyl point:

In Eq. (1), when $m = 0$, the Dirac Hamiltonian decouples into two separated Weyl equations given by $\pm v\boldsymbol{k}\cdot\boldsymbol{\sigma}$. Each Weyl equation describes a two-component chiral Weyl fermion with chirality ± 1[47,344,345]. In general, a two-component Weyl fermion described by the Weyl equation arises when two non-degenerate energy bands in a solid touch at a point k_0 in momentum space [see Fig. 10(a)][346-350]. Clearly, this cannot happen when Kramers degeneracy holds at every momentum $\boldsymbol{k}$. Therefore, time (T) and parity (P) symmetry cannot be simultaneously satisfied; at least one of them must be broken[351-355]. In this sense, Weyl-point TMs may only occur in noncentrosymmetric or magnetic materials. The topology of Weyl fermions follows from the fact that Weyl points are monopoles of momentum-space Berry curvature[356-358]. Therefore, in a system with only chiral Weyl fermions, the Weyl points must come in pairs of opposite monopole charges[38,347,359]. This explains, for instance, why the massless Dirac equation [cf. Eq. (1)] decouples into two Weyl equations with opposite chirality. The opposite monopole charges act as the point sources and sinks of the Berry curvature field. When a Weyl-point TMs has surfaces in real space, there must be a surface state connecting each pair of Weyl points in the momentum space, which appears in the surface energy dispersion plot as a Fermi arc[347,360,361].

Triple point:

In solid state systems, three-, six-, and even eight-fold band crossings can be observed which yields low-energy fermionic excitations that cannot be described by a Dirac or Weyl equation[266,362-364]. Instead, their dispersions have to be described by a more general Hamiltonian[365]. The departure from the (low-energy) description of familiar relativistic free fermions (i.e., Dirac and Weyl fermions) is a consequence of the less-restrictive nature of crystal symmetry. On the other hand, it allows for the realization of more low-energy fermions (which otherwise do not exist). These TMs, characterized as "multifold" (i.e. three-, six-, and eight-fold) fermions are symmetry-enforced semimetals, as their very existence relies on the fundamental constraints originated from the space group symmetry[366], possibly

combined with T symmetry. For example, a crystal having a threefold rotational axes and point-group symmetry C_{3v} can be a "triple-point" semimetal[367-372]. The origin of the triple-point semimetals is rooted in the band inversion between a single and doubly degenerate bands (see Fig. 10(b)). There exist unique physical phenomena associated with these quasiparticles[263,264,343,362,373,374], such as the occurrence of topological surface Fermi arcs, transport anomalies and topological Lifshitz transitions.

3.3 Nodal-line TMs

In 3D, two bands can cross each other along a closed curve or at a surface at discrete Dirac or Weyl points, as discussed above. When it is a curve, the curve is called a nodal line[375-383], which may either take the form of an extended line running across the Brillouin zone (BZ), whose ends meet at the BZ boundary[267], or wind into a closed loop inside the first BZ[381], or even form a chain consisting of several connected loops (nodal chains)[299]. Topological semimetals with such line crossings are called topological nodal-line semimetal[384-389]. The ideal Fermi surface of a nodal-line TMs is a nodal line or a self-enclosed ring at half-filling, which may be obtained only if there is a particle-hole or a chiral symmetry that pins all the points of the nodal line exactly at the Fermi energy. Along the line or ring, the nodal line should be flat or dispersionless. As such, many-body effects, such as long-ranged Coulomb interactions and topological superconductivity[267,390,391], may exist in nodal-line TMs. Nodal-line degeneracies can take place when energy bands of different crystal symmetries cross along a rotational axis, or on a mirror- or glide-invariant plane of the BZ[295,392-395]. In addition, nodal lines can also occur as a result of band topology, in which the nodal lines are associated with a topological invariant[396-398]. A variety of topological nodal-line semimetals have been identified with distinct characteristics (unique to each class) such as topological invariants, degeneracy at the band crossing, Fermi surface geometry, and the linking structure of the multiple nodal lines[399-403].

Compared with nodal-point semimetals, nodal-line semimetals have more subtypes because a line can deform in many ways, such as forming a ring or a knot[294,404-406]. If there are two or more lines/rings of different origins in momentum space, they can construct even more topological phases[407-414]. Figure 11 depicts several basic topological elements made of nodal rings. For example, Fig. 11(a) is an isolated nodal ring; Figs. 11(b-c) are intersecting nodal rings (INRs), in which all the rings share a

common center; Fig. 11(d) is a nodal chain, where the nodal rings contact each other in a sequential manner and extend across the BZ to form a chain; Figs. 11(e-f) show nodal link and Hopf link, respectively, in which the nodal rings are topologically linked together. Note that one of the rings in the Hopf link crosses the boundaries of the BZ, making it distinct from the standard nodal link in Fig. 11(e).

For nodal-line semimetals, there are surface states which appear inside the projections of the nodal line states. These surface states are also very flat and are hence dubbed the 'drumhead' states[342,370,379,415,416]. They can be considered as a higher-dimension analogy to the flat band on the zigzag edge of graphene. However, these surface states are not topologically protected; a small change on the surface may destroy their 'flatness' or even push them into the bulk continuum. Due to the lack of a surface signature, people turn to use bulk probes for nodal-line semimetals: for example, the special behaviors of these materials in quantum oscillation have been predicted and measured[273]. There are also zero modes in the spectrum of Landau levels[385,417], leading to a peak in the density of states at the Fermi level.

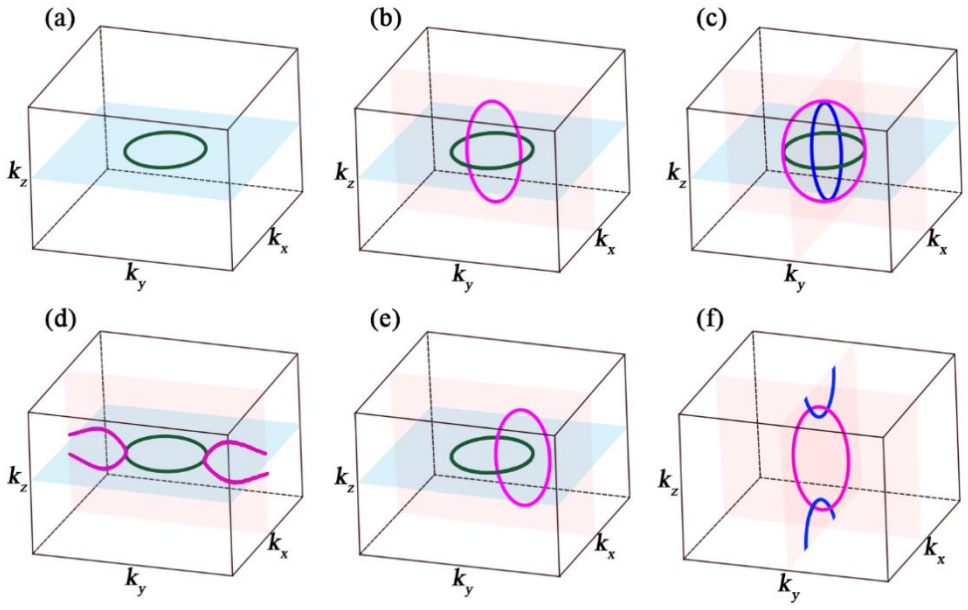

Figure 11. Topological elements consisting of nodal lines (or nodal rings). (a) An isolated nodal ring; (b-c) intersecting nodal rings (INRs) of two and three rings, respectively; (d) a nodal chain; (e) nodal link, and (f) Hopf link.

3.4 Nodal-surface TMs

Besides points and lines, band crossing in a 3D BZ can also take the form of a 2D nodal surface[76,77,304,418,419]. On such a surface, each point is a crossing point of two linear bands in the direction normal to the surface. The nodal surface is distinct from the ordinary Fermi surface, because the coarse-grained quasiparticles excited from a nodal surface have an intrinsic pseudospin degree of freedom (representing the two crossing bands), behaving effectively like a 1D massless Dirac fermions along the direction normal to the surface, and may therefore have interesting physical properties.

In the absence of the SOC, there are two different classes of symmetry-protected nodal surfaces[420]. The first class, shown in Fig. 12(a), is protected by the space-time inversion symmetry and sublattice symmetry, and is characterized by a Z_2 topological index. The second class is guaranteed by a combination of a twofold screw-rotational symmetry and the time-reversal symmetry. It is noteworthy that the band structures of the two classes are distinctly different due to their qualitatively different physical origins. Nodal surfaces in the first class have the nontrivial Z_2 topological charge, and therefore appear in pairs in the BZ, conforming the Nielsen-Ninomiya no-go theorem[421,422]. Those in the second class exist, due mainly to the two-fold nonsymmorphic symmetry. In contrast to the first class, however, the second class exists alone in the BZ, instead of in pairs and hence without the topological charge. The topological uniqueness of the second class has been revealed in Ref. [304].

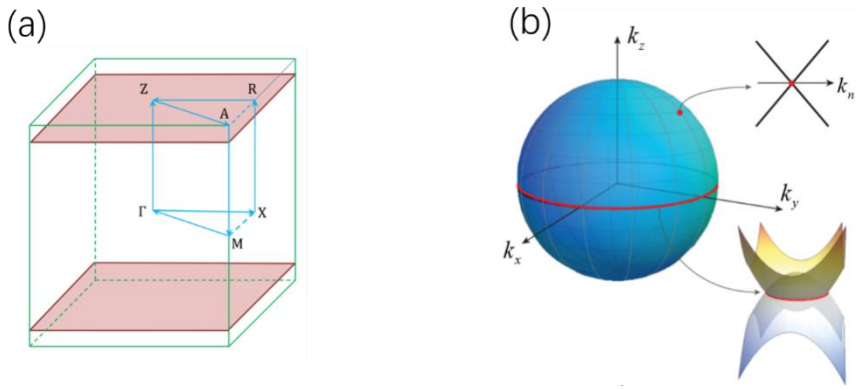

Figure 12. (a) A planner and (b) a spherical nodal surface.

The nodal surfaces can be planar surfaces or have a spatial shape such as forming a sphere[418], as depicted in Fig. 12(b). Around the surfaces, low-energy quasiparticles can be described by an effective

Hamiltonian[77]

$$H(k_z) = \tau_z v k' \sigma_z, \quad (2)$$

where $k' = k - k_0$ is the wave vector component normal to the nodal surface with k_0 the vertical distance from the surface to the center of the BZ, v is the Fermi velocity, and σ_z (the Pauli matrix) denotes the two bands crossing at the surface. In addition, nodal surface could also be a tube, a crossbar or any other surfaces.

IV Topological properties of carbon

4.1 Orbital physics in the graphene-based structures

Electrons in an isolated atom are characterized by their charge, spin, and orbital character[423]. When these atoms form a solid, mutual interactions and entanglements of these can lead to the determination of material properties. One can manipulate one or more of the above to achieve desired goals. For example, charge is associated with electrical conductivity and spin with magnetism[424]. Usually, electrons in the outer-shell orbitals are most important to most of the physical and chemical properties of a solid. Due to the orthogonality requirement in quantum mechanics, different atomic orbitals must have different wave functionsshapes[425]. For instance, while an *s* orbital is spherical and an even function with respect to the origin, the next higher-energy *p* orbitals are non-spherical and odd functions with respect to the origin. The spherical symmetry of an atom determines that there are only three such *p* orbitals degenerate in energy, which form the basis for the topological properties of carbon. From an electronic structure point of view, within the tight-binding model[426,427], all the band structures are determined by the interplay between the *s* and *p* orbitals of the valence electrons inside the crystal and the spatial symmetry of the crystal.

Carbon has six electrons, of which the four outer-shell electrons $2s^2 2p^2$ are the valence electrons. A carbon atom can thus have sp, sp^2, or sp^3 hybridization to form a variety of allotropes of different bonding configurations[428]. Graphene may be viewed as a 2D π-conjugated material, in which the sp^2-hybridized carbon atoms are arranged such that they form a 2D hexagonal lattice composed of

benzenoid rings[429] [see Fig. 13(a)]. On the other hand, its delocalized π-conjugated electrons in the hexagonal lattice yield a unique band dispersion, i.e., a Dirac dispersion near the Fermi level (E_F)[430,431]. This is important for our discussion, because in most graphene-based 3D structures, the electronic properties are dominated by atomic *p* orbitals similar to the p_z orbital in graphene[69,77,78,432,433]. For example, Fig. 13(b) shows the wavefunctions of electrons near the E_F in a 3D IGN[62], where the p_z orbitals of graphene become p_x and p_y orbitals if we take the perpendicular direction out of page as the *z* axis. Other lattices can also accommodate the p_z orbitals of graphene in a similar manner to produce rich physical properties as the interactions among these orbitals will be lattice- and atomic structure-dependent[77,434]. To envision such situations, especially when the relative phases between neighboring orbitals matter, it makes sense to treat these *p* orbitals as a rank-1 tensor (or vector) with a clearly-defined polarity (e.g., pointing from its negative lobe to positive lobe), in analogy to a spin vector[435,436]. If these vectors are placed in a Kagome lattice (such as in the CKL discussed earlier), the so-called "spin frustration" will occur[218]. In other words, these *p* orbitals will not be able to arrange themselves to yield a long-range "antiferromagnetic" ordering in their respective phases[185].

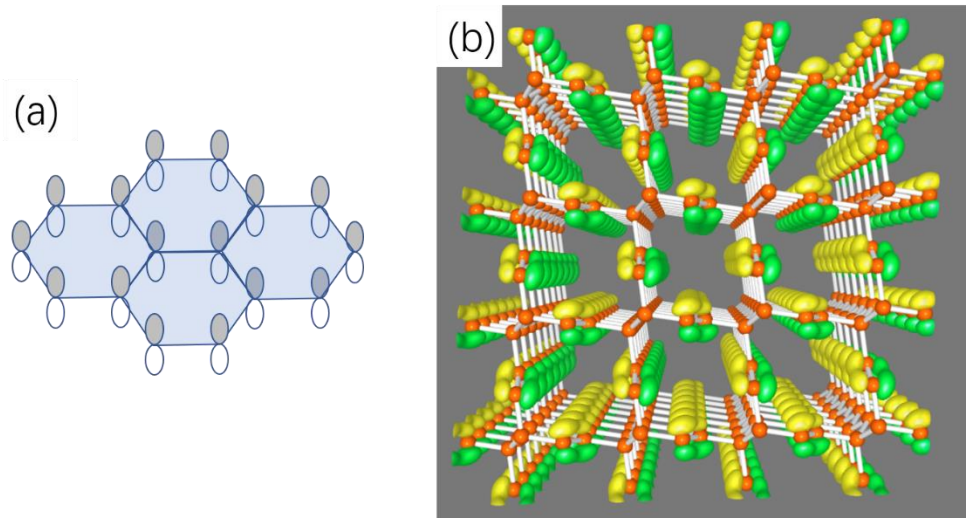

Figure 13. (a) An in-phase p_z orbital configuration in graphene. (b) The distribution of *p* orbitals in an IGN.

4.2 Topological properties of graphene nanoribbon junctions and carbon nanotubes

Graphene nanoribbon junctions: Like graphene, the electronic structure of 1D GNR has

interesting topological properties[437-442]. The exact electronic topology is, however, determined by the spatial symmetry and termination at the edges. Hence, GNRs of different widths, edge shapes, and end termination geometries belong to different topological classes[437].

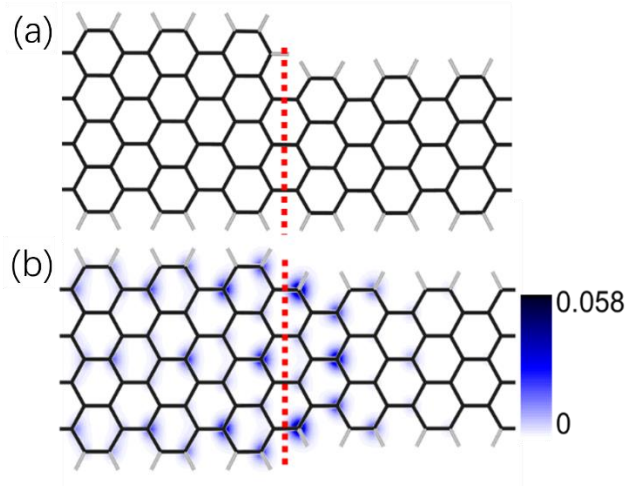

Figure 14. Heterojunctions formed between two topologically (a) equivalent and (b) inequivalent $N = 9$ and $N = 7$ armchair GNRs (9AGNR/7AGNR). Red dashed lines denote the interfaces. The carbon-carbon and carbon-hydrogen bonds are colored black and gray, respectively. The color scale shows the charge density of the localized midgap junction state. The charge density is integrated along the out-of-plane direction [in units of $1/(\text{a.u.})^2$].

Joining two GNRs of different topological classes leads to localized junction states at their interfaces[442]. Here, the bulk-boundary correspondence in armchair GNR heterojunctions is shown, which are experimentally accessible by bottom-up synthesis with precursor molecules. Figure 14(a) show two possible types of junctions formed by an $N = 7$ armchair GNR and an $N = 9$ armchair GNR. For the nonsymmetric junction, both $N = 7$ and $N = 9$ armchair GNR segments have a zigzag termination, and they are topologically equivalent. As a result, no localized junction states can be found at the interface. For the symmetric junction [Fig. 14(b)], however, the termination of the $N = 7$ armchair GNR changes, so the two GNRs become topologically inequivalent. As a result, one localized junction state emerges in the band gap[442].

Carbon nanotubes: Most carbon nanotubes can be nontrivial one-dimensional topological insulators in the absence of a magnetic field and are characterized by a Z-topologically invariant winding number[443,444]. This number determines the number of edge states localized at the ends of the tube ends. When applying a magnetic field along the tube axis, on the other hand, a topological phase

transition could take place at which the band gap closes except for the armchair nanotubes for which so such a transition can occur. This phase transition enables the identification in experiment of the topology of the nanotubes before the gap closure[445].

4.3 Dirac points in 2D carbon sheets

Graphene is perhaps the most well-known 2DDirac material with two Dirac points located at K and K' points of the BZ, energy E_F, as shown in Fig. 15(a) for K[167,446,447]. Near the E_F, electrons behave as if they have no mass, resulting in energies that are proportional to the momentum of the electrons. There have been different classes of materials possessing such distinctive electronic properties: besides graphene, noticeably the high-temperature *d*-wave superconductors[448,449] and topological insulators[249,450].

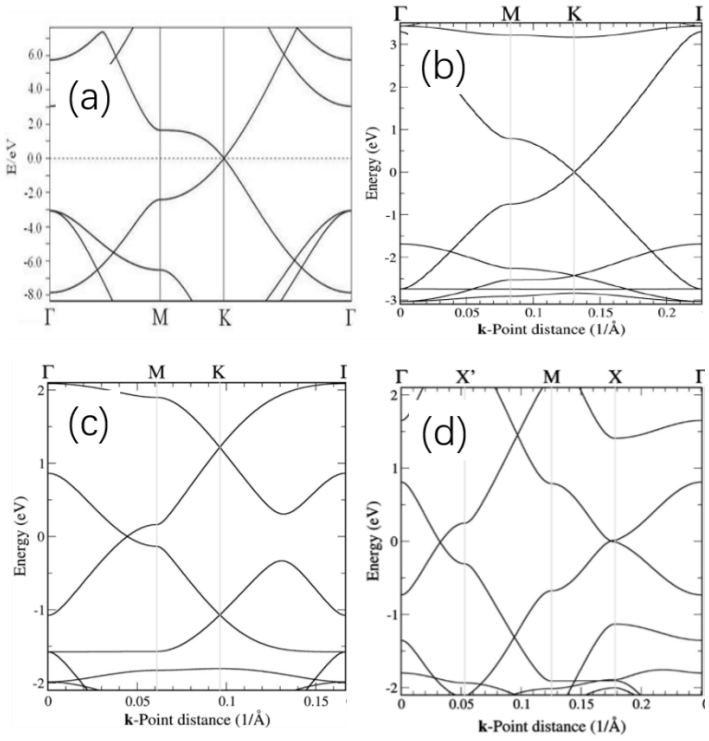

Figure 15. Band structures of graphene and graphyne: (a) graphene, (b) α-graphene, (c) β-graphyne, and (d) 6,6,12-graphyne. All exhibit characteristic Dirac points at E_F.

In this regard, it is worth noting that the three graphynes in Fig. 3 are also Dirac materials[451-454], as can be seen in Figs. 15(b-d). By examining Fig. 3, we conclude that the introduction of the triply-bonded *sp* carbon atoms do not affect the Dirac cones, which originate from the sp^2 carbon networks.

Thus, similar to graphene, Fig. 15(b) shows that hexagonal α-graphyne has a nearly isotropic electric property near the E_F at K point[167]. However, such an isotropy is lost when the symmetry of the crystal is altered as in the case of β- and 6,6,12-graphynes where the Dirac points do not reside at any high symmetry points of the BZ[167]. In the case of rectangular 6,6,12-graphyne, the symmetry change even alters the relative energy positions between the Dirac point along X'- Γ and that along X-M[167]. This energy shifts make one Dirac cone slightly above the E_F, while the other slightly below the E_F, which enables a self-doping of the graphyne to result in spontaneous electron and hole pockets. This self-doping effect can be further tuned by applying an in-plane strain.

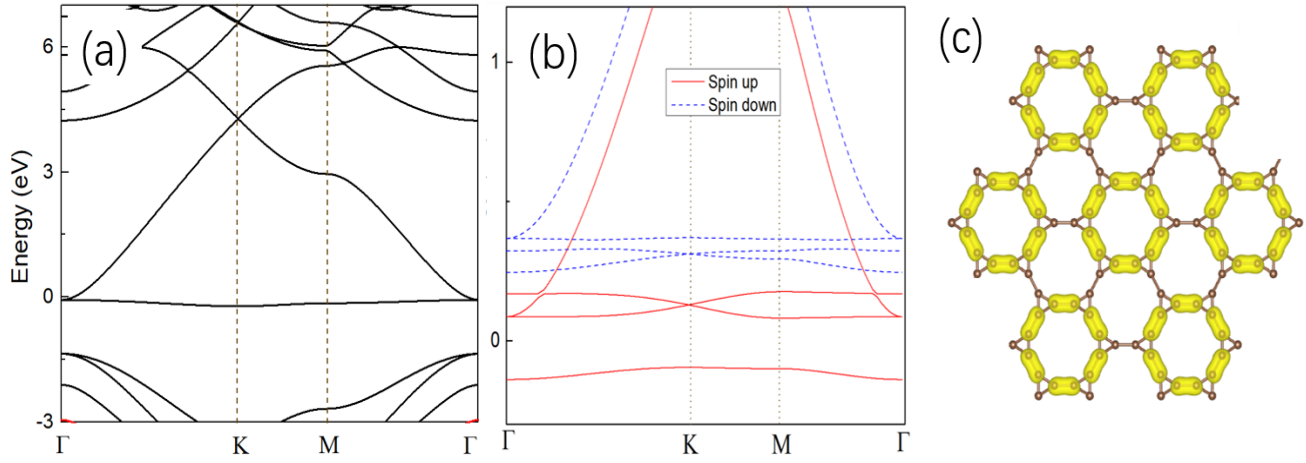

Figure 16. (a) Band structure of the Kagome graphene in Fig. 4(a). (b) Band structure of the Kagome graphene in the $\sqrt{3} \times \sqrt{3}$ supercell as a result of hole doping with a filling factor for the flat band of 1/6. (c) Charge density contour for states in the occupied flat band in panel (b), showing a Wigner crystallization.

In a Kagome lattice in Fig. 4(a), there exist the so-called Kagome bands, each of which consists of two Dirac bands plus a flat band as can be seen in Fig. 16(a)[108]. Here, the flat band appears right below the E_F. The two Dirac bands, which connect the flat band at the Γ point, cross each other at the K point, forming a Dirac point but at a considerably higher energy. The flat band is fully occupied while the two Dirac bands are empty. Interaction in a flat band is magnified due to the divergence in the density of states, which gives rise to a variety of many-body phenomena such as ferromagnetism, Wigner crystallization, and anomalous quantum Hall effect[108]. Upon hole doping, the flat bands will split into spin-polarized bands of different energies to result in a flat-band ferromagnetism [see Fig. 16(b)]. In particular, at a half filling $\nu = \frac{1}{2}$, the splitting reaches the maximum value of 768 meV. At

smaller fillings, e.g., when $\nu = \frac{1}{6}$, on the other hand, a Wigner crystal spontaneously forms, as shown in Fig. 16(c), where the electrons form closed loops localized on the grid points of a regular triangular lattice[108]. As expected, it breaks the translational symmetry of the original Kagome lattice.

4.4 Topological properties of 3D carbon allotropes

Dirac/Weyl loops and points in IGN

Figure 17(a) shows that each primitive cell of an IGN contains six C atoms, which form two separate obtuse triangles symmetrically placed with respect to the inversion center of the cell[62]. Chemically, the six atoms also belong to two different groups: the two near the inversion center (marked grey) are fourfold coordinated; and the other four (marked red) are threefold coordinated.

In the band structure in Fig. 17(b), linear dispersions near the E_F along the Γ-Z, Y-T, and Y'-T' symmetry lines are observed. A closer examination of the BZ in Fig. 17(c) reveals that the linear band crossings take place along two closed loops traversing the BZ in the (110) mirror invariant plane around $k_c = \pm 0.45\pi/c$, as shown in Fig. 17(d). The two loops are in fact time-reversal and inversion images of each other.

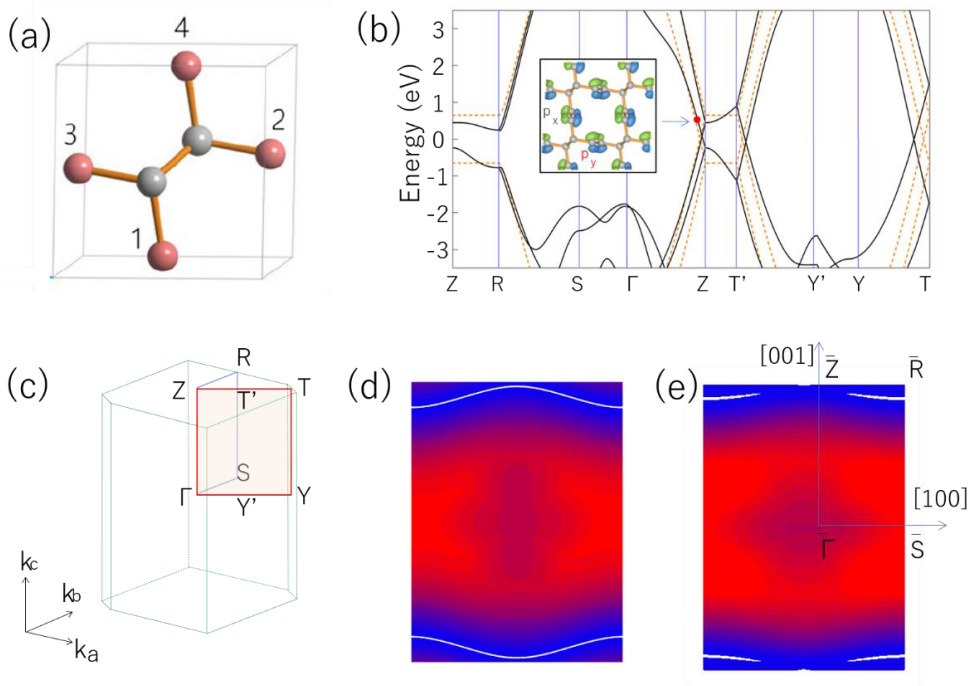

Figure 17. Electronic structure of IGN. (a) Primitive cell, (b) energy dispersion, (c) the first BZ, (d) Dirac/Weyl loops on the $k = k_a = k_b$ surface, and (e) Fermi arcs between Weyl points.

A charge analysis [see inset of Fig. 17(b)] reveals that the bands near E_F are mainly made of the p_x and p_y orbitals of the π-bonds, spatially located on only one type of the atoms, i.e., the four (orange) peripheral carbon atoms in Fig. 17(a)[62]. Thus, the local atomic structure, the linear dispersion, and the π-bond character of the states are all reminiscent of the 2D graphene. If we ignore the small dispersion along $k = k_a = k_b$ in Fig. 17(d), the energy spectrum near E_F may be viewed as derived from a superposition of non-interacting 2D graphene sheets stacked in the [110] direction.

To capture energy dispersions near the E_F, one may construct a minimal tight-binding model that includes the four peripheral carbon atoms with one p orbital each (either p_x or p_y depending on the locations)[62],

$$\mathcal{H}(\boldsymbol{k}) = \begin{bmatrix} 0 & Q(\boldsymbol{k}) \\ Q^{\dagger}(\boldsymbol{k}) & 0 \end{bmatrix}, \qquad \text{with } Q(\boldsymbol{k}) = \begin{bmatrix} f_{14} & f_{13} \\ f_{24} & f_{23} \end{bmatrix}, \tag{3}$$

where $f_{ij}(\boldsymbol{k}) = \sum_{\mu} t_{ij} e^{-i\boldsymbol{k}\cdot\boldsymbol{d}_{ij}^{\mu}}$, $i,j \in \{1,2,3,4\}$ are the site labels in Fig. 17(a), t_{ij} is the hopping strength between sites i and j, $\boldsymbol{d}_{ij}^{\mu}$ is the vector directed from j to i, and μ runs over all equivalent lattice sites under translation. The spectrum of the energy band is symmetric about zero energy because of the presence of a chiral (sublattice) symmetry $\mathcal{C} = \sigma_z \otimes \sigma_0$ in Eq. (3), such that $\mathcal{C}H\mathcal{C}^{-1} = -H$ is independent of $\boldsymbol{k}$, where σ_α are the Pauli matrices. It is easy to show that zero-energy states would appear if the following two conditions are met: (1) $k_a = k_b$ and (2) $\cos(k_c c/2) = \sqrt{t_{13}t_{24}/(4t_{14}t_{23})}$. The first condition restricts the zero-energy states to the mirror invariant plane, whereas the second one further restricts them onto two separate loops at $\pm K_c = (2/c)\arccos[\sqrt{t_{13}t_{24}/(4t_{14}t_{23})}]$.

The inversion symmetry of the IGN may be destroyed by inserting (chemically inert) helium atoms into the interstitial sites or holes in Fig. 17(a), with a filling of one He per primitive cell[62]. This will result in four Weyl-like points. We use the phrase Weyl-like here, because in our discussions the

spin degree of freedom never enters due to the exceedingly small spin-orbit coupling of carbon. Once the Weyl-like points are created, they are topologically protected by the Chern number of any constant-energy surface enclosing these points. If we have an open system with surfaces, surface Fermi arcs must emerge, connecting the surface-projected Weyl-like points of opposite chirality. This is indeed the case as can be seen in Fig. 17(e) where the Fermi arcs on the (100) surface are shown[62].

Classification of nodal rings: the case for armchair graphene networks

Figure 18(a) shows an atomic structure of the carbon networks formed by connecting armchair GNRs, named AGNW-(m,n)[451]. Variations in m and n produce a series of networks. At the shared atomic lines are the gray atoms, which are all sp^3 hybridized, while inside the nanoribbons are the unshared blue C_1 and pink C_2atoms, which are all sp^2 hybridized. The space groups of AGNW-(3,2) and (1,2) are both IMMA with a mirror plane M_z normal to the z axis.

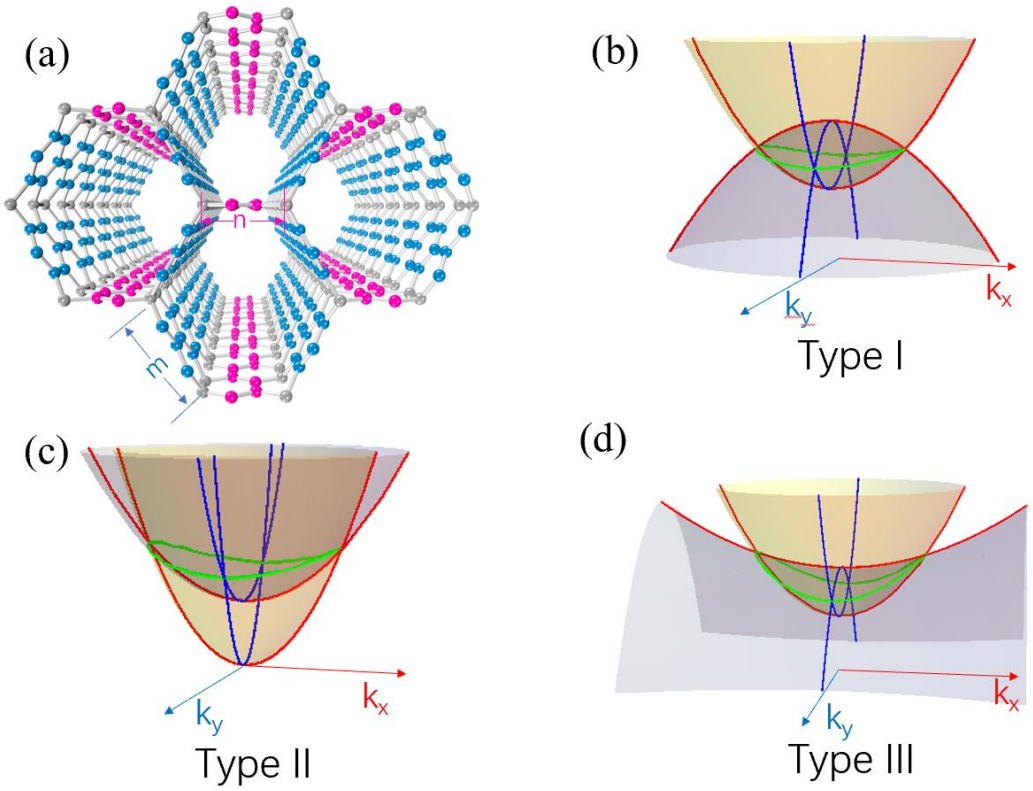

Figure 18. (a) Atomic structure of AGNW-(m,n), (b) type-I, (c) type-II, and (d) type-III nodal rings. All three types can be found in AGNW-(3,2) and (1,2) under a strain.

First-principles calculations of AGNW-(3,2) and (1,2) reveal three different types of nodal rings, whose characteristic energy dispersions are schematically shown in Figs. 18(b-d)[451]. Both type-I and II rings may be viewed as a crossing line between two paraboloids as indicated by the green lines in Figs. 18(b-c). The opening of the paraboloids is always along the energy axis, either positive or negative: if they are in the opposite directions, one gets a type-I ring, if they are in the same direction, however, one gets a type-II ring, in accordance with the definitions of type-I and II Dirac points. On the other hand, a type-III ring emerges when a crossing between a paraboloid and a saddle surface takes place, as shown in Fig. 18(d), in which along k_y the Dirac point is type-I but along k_x the Dirac point is type-II.

Since the classification only requires knowledge on the curvature of the energy bands, it can be straightforwardly obtained by a k•p model up to quadratic terms in k, in this case at the Γ point[451]:

$$H(\boldsymbol{k}) = \begin{bmatrix} A_1 k_x^2 + B_1 k_y^2 & iCk_z \\ -iCk_z & \Delta + A_2 k_x^2 + B_2 k_y^2 \end{bmatrix}, \tag{4}$$

where Δ is the band gap, and A_1, B_1, A_2, B_2, and C are band parameters obtained by fitting to the DFT results. By a change in the signs of these parameters, all three types of nodal rings (discussed above) are obtained.

Note that the electron hole pockets arising from the Hamiltonian in Eq. (4) exhibit a rich variety of patterns, which can serve as a platform to study fundamental electronic and magnetic properties of the rings such as anisotropy in electron/hole transport and collapse of Landau levels[451]. It is known that the nodal rings are subject to a (Lifshitz) phase transition, through which the electron hole pockets gradually evolve from one to the other – a phenomenon that may be used to study electron-hole friction and strongly-correlated Coulomb interactions in the flat-band region as a result of the transition[452].

Interlocking nodal chains

Dirac/Weyl surfaces

Three types of graphene networks, TGN(2,2), QGN(2,2), and HGN(2,2), have been discussed in

Fig. 7[77]. All of them are TMs with nodal-surfaces. Here, we will take the simplest case, QGN(2,2) in Fig. 19(a), to explain the electronic properties for all of them. One observes from the band structure in Fig. 19(b) that linear crossings at the Weyl-like points appear along each of the symmetry lines, Γ-Z, A-M, and X-R in the BZ, which are in fact the E_F. There are three of them, all marked on in the inset of Fig. 19(b) as red dots. Interestingly, all three points have a common $k_z = 0.39\pi/c$. In other words, they all lie on a flat Weyl surface, denoted in the inset by the pink-red plane. Because of time reversal symmetry, there should be another Weyl surface at $k_z = -0.39\ \pi/c$. It should be noted that here the Fermi surface passing the Weyl points is different from that of an ordinary metal in the sense that the low-energy quasiparticles here must be described by a two-component Weyl spinors[77].

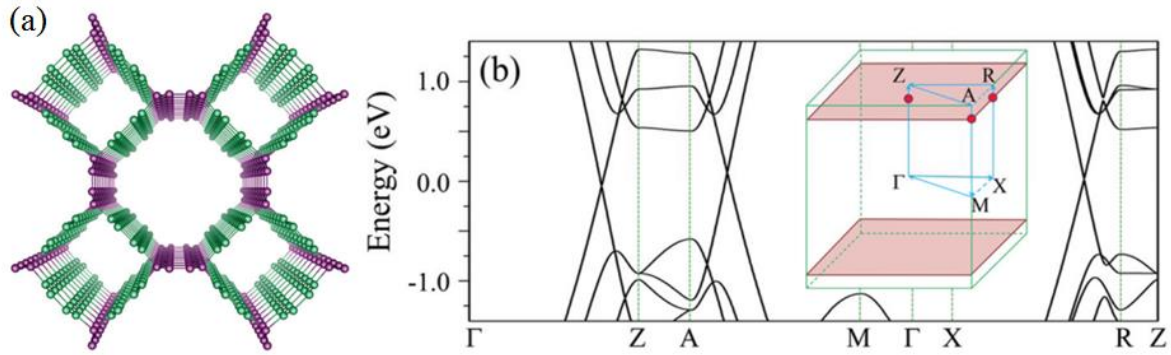

Figure 19. QGN(2,2). (a) Atomic structure and (b) energy dispersion near the Fermi level, where the pink-red-color-shaded planes are Weyl surfaces in the BZ.

The existence of Weyl surfaces in graphene networks can be explained by orbital-orbital interactions[77]. In particular, the electronic states near the E_F originate from green-color nanoribbons in Fig. 19(a), which, together with the purple-color corner carbon atoms, may be viewed as deformed nanotubes with a square cross section, separated by the purple-color nanoribbons which have no contribution to the electronic states near the E_F. As such, the network can be viewed as a 3D bundle of carbon nanotubes. It is known that the nanotubes are 1D Weyl semimetals with a linearly crossing at E_F in their respective band structures[455]. It turns out that, when forming the carbon networks, the inter-tube coupling between the σ electrons in the *x-y* plane is rather strong, leading to significant dispersions, but that between the π electrons in the same *x-y* plane is negligible. The latter leads to the Weyl surfaces in the *x-y* plane, which are almost dispersionless, as can be seen in the inset in Fig. 19(b).

The Weyl surface is usually unstable unless it is protected by symmetry and/or topology. In the current case, the stability of the Weyl surface is guaranteed by sublattice symmetries originated from crystalline mirror symmetries along the *x* and *y* axes, inherent to the structure, or a combination of the two. Such carbon systems, due to a negligible spin-orbit coupling, fall within the BDI topological class with a 0D $\mathbb{Z}_2$ topological invariant defined at any point in the BZ with a local gap[456-458]. The $\mathbb{Z}_2$ invariant just indicates whether the gap is inverted or not, when referenced to the normal band ordering in the atomic limit. In the graphene networks, the band gap is inverted ($\mathbb{Z}_2 = 1$) near the central region of the BZ, while un-inverted ($\mathbb{Z}_2 = 0$) near the Z-point at the boundary of the BZ. The Weyl surfaces, which separates these two regions of different band topologies, cannot be gapped, as long as the sublattice symmetry is maintained[77].

Triple points and linked nodal rings in 3D pentagon carbon networks

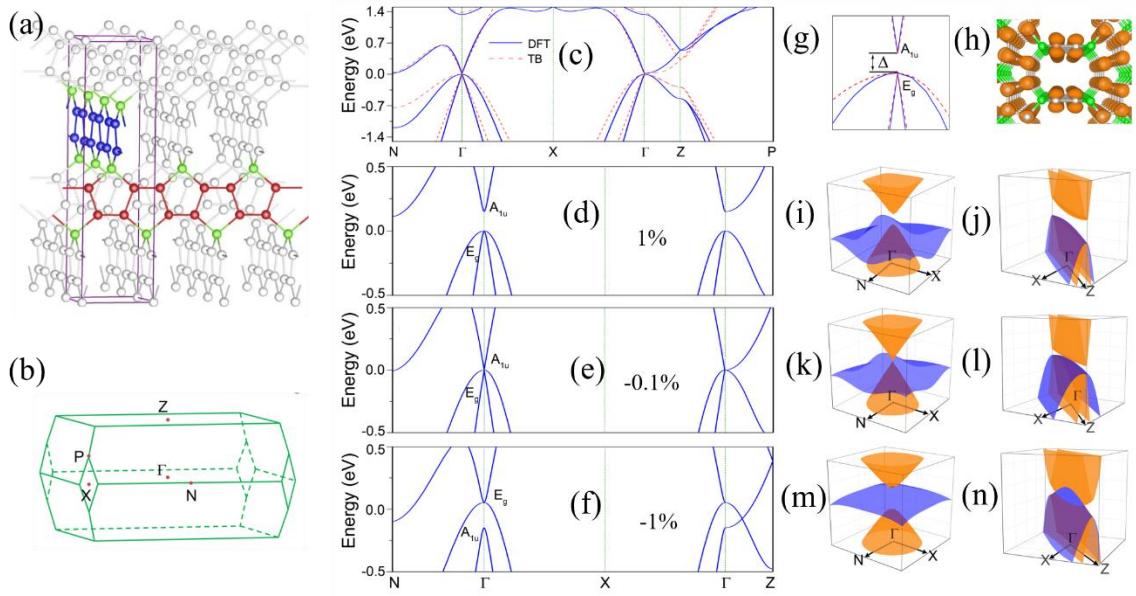

Figure 20. (a) Atomic structure and (b) the first BZ of a 3D pentagon carbon. (c) The corresponding band structure by DFT (black lines) and TB (red dashed lines), and (d-f) the band structures of 3D pentagon carbon under 1%, 0.1% and 1% uniaxial strain along z-direction. (g) The zoom-in view of band structure around the Γ point in (c) along N-G-X. The two degenerate valence bands at Γ belong to the 2D irreducible representation E_g, and the lowest conduction band belongs to the one-dimensional A_{1u} representation. (h) The charge density distribution for states near the Fermi level in (c), indicating these states are mainly from *p* orbitals of the sp^2 hybridized atoms. (i-n) The 3D band structures on the N-G-X and the X-G-Z planes corresponding to (d-f), respectively.

Another class of carbon allotropes are the 3D pentagon carbon networks, one of which is shown

in Fig. 20(a)[202]. It can be viewed as being formed by interlinking two orthogonal arrays of pentagonal-ring nanoribbons (red and blue, respectively), which are then stacked along the z direction. Upon linking, the two nanoribbons share one atom marked by green in Fig. 20(a). Similar to most of the 3D carbon networks, in the pentagon lattice, there are two kinds of carbon atoms, i.e. the sp^2-hybridized red and blue atoms and the sp^3-hybridized green atoms. The structure has the nonsymmorphic D_{4h}^{19} space group (No. 141, $I4_1/AMD$), of which an important symmetry element is the screw $\overline{C}_{4z}$, which is a four-fold rotation along z, followed by a factional translation of $c\hat{z}/4$, where c is the lattice parameter in the z direction[202].

The pentagon carbon networks are unique in topological physics because they produce a series of topological fermions beyond the usual Dirac and Weyl fermions[260,344]. For example, the band structure in Fig. 20(c) shows that, under equilibrium, the network is a narrow-gap semiconductor. At Γ point and near E_F, there are two degenerate valence band states (heavy-hole and light-hole) and a single conduction band state only 21.4-meV higher in energy. In the vicinity of Γ, the light-hole valence band and the conduction band nearly cross linearly. The degeneracy of the two valence band states is a result of symmetry as they both belong to the 2D irreducible representation E_g of the D_{4h} group. In contrast, the conduction band state belongs to the 1D A_{1u} representation of the D_{4h} group. The two valence bands remain degenerate along Γ-Z (i.e., along the k_z-axis). This is because there is a smaller group C_{4v} along the screw axis, such that the 2D representation does not split. From an analysis of the wavefunctions and projected density of states (PDOS), one see that the band-edge states are mainly derived from the π orbitals of sp^2 carbon atoms.

Since the band gap is small, applying a tensile strain can increase the gap to produce a semiconductor, while a compressive strain can close the gap towards a semimetal [Figs. 20(d-f)]. Of particular interest is the latter case when the band gap between the A_{1u} singlet and E_g doublet at Γ is closed, i.e., at the transition point. Due to the different symmetry characters, however, A_{1u} and E_g cannot hybridize with each other, which leads to the formation of the triplet point at Γ, as shown in Fig. 20(e)[202]. Figures 20(i-n) present 3D band structures on the N-G-X and the X-G-Z planes corresponding to Figs. 20(d-f), respectively. Figure 21(a) exhibits the topological triplet point in the first BZ.

After the transition point, if one applies strain further, the band order at Γ becomes inverted, while

the order at Z remains the same. Such a band topology implies that the two bands must now cross each other between Γ and ±Z. Furthermore, because the two bands belong to different representations along the screw-axis, they must cross in a linear manner, with two triply-degenerate points: one on each side of Γ as shown in Fig. 21(b). Therefore, the metallic phase of the pentagon carbon networks represents a novel TM phase with a pair of triply-degenerate band-crossing points near E_F.

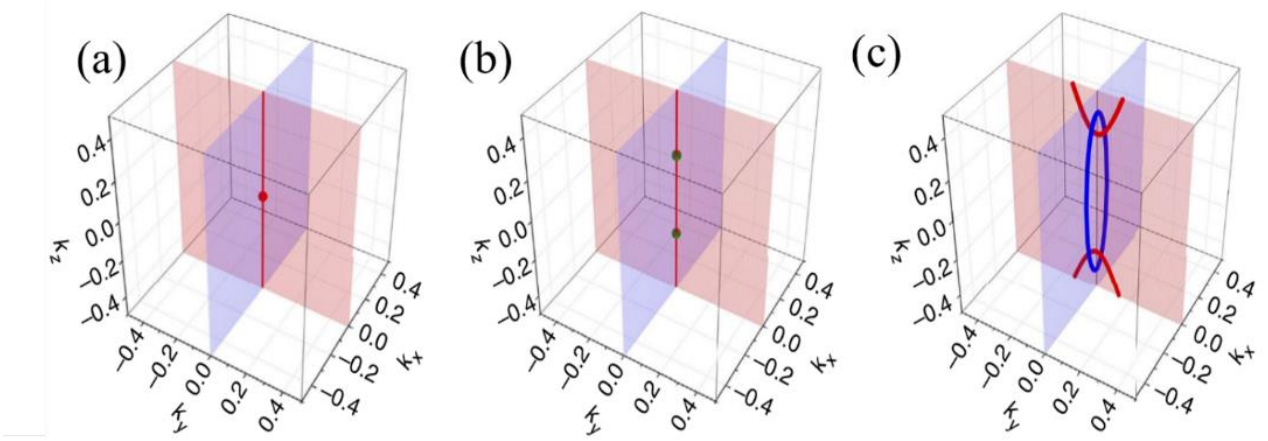

Figure 21. Schematic of the band-crossing evolution in reciprocal space, from (a) a single isospin-1 triplet fermion point at the BZ center, to (b) two triply degenerate fermion points along k_z-axis (one on each side of Γ point), further to (c) two inter-connected (Hopf link) Weyl loops (with one Weyl loop being centered at Γ point, while the other loop crossing the first Brillouin zone boundary). In (a-b), the red line along the k_z-axis marks the (twofold) band degeneracy line protected by the fourfold screw-rotational symmetry. Note that the dispersion transverse to this line (that is, in k_x–k_y plane) is of quadratic type (which can be observed from Fig. 20).

To describe the above topological quantum phase transition near the band edges, a **k·p** model at Γ up to quadratic order is sufficient[202]:

$$H(\mathbf{k}) = (C + D_1 k_z^2 + D_2 k_\perp^2) + \begin{bmatrix} \Delta + B_1 k_z^2 + B_2 k_\perp^2 & -iAk_x & -iAk_y \\ iAk_x & 0 & B_3 k_x k_y \\ iAk_y & B_3 k_x k_y & 0 \end{bmatrix}, \quad (5)$$

where the coefficients A, B_1, B_2, C, D_1, D_2, and Δ are determined by fitting the DFT results. At the transition point, $\Delta = 0$, the three bands cross at a single point. To see what happens qualitatively, we may keep only the k-linear terms in Eq. (5). The following equation will result:

$$\mathcal{H}(\mathbf{k}) = A\mathbf{k} \cdot \boldsymbol{\lambda}, \quad (6)$$

where $\mathbf{k} = (k_x, k_y, 0)$, and

$$\lambda_x = \begin{bmatrix} 0 & -i & 0 \\ i & 0 & 0 \\ 0 & 0 & 0 \end{bmatrix}, \qquad \lambda_y = \begin{bmatrix} 0 & 0 & -i \\ 0 & 0 & 0 \\ i & 0 & 0 \end{bmatrix}, \qquad \lambda_z = \begin{bmatrix} 0 & 0 & 0 \\ 0 & 0 & -i \\ 0 & i & 0 \end{bmatrix}$$

are three of the eight Gell-Mann spin-1 matrices[459], describing isospin-1 triplet fermions moving in the *xy*-plane[202,362]. The fermions are helical with a well-defined helicity of ± 1 or 0, corresponding to the eigenvalues of a helicity operator $\mathbf{k} \cdot \boldsymbol{\lambda}/k$. The two branches with a helicity of ±1 are massless, while the one with a helicity of 0 has a flat dispersion (= infinite mass).

Passing the critical point, the isospin-1 triplet splits into two triply-degenerate points at $k_z = \tau K_c$, respectively, where $\tau = \pm$ and $K_c = \sqrt{-\Delta/B_1}$ according to Eq. (5). Note that to reproduce the DFT band structure in Fig. 20(e), one must have $\Delta < 0$ and $B_1 > 0$. The linearized model of Eq. (5) in this case becomes[202]:

$$H_\tau(\mathbf{q}) = \begin{bmatrix} 2\tau(B_1 + D_1)K_c q_z & -iAq_x & -iAq_y \\ iAq_x & 2\tau D_1 K_c q_z & 0 \\ iAq_y & 0 & 2\tau D_1 K_c q_z \end{bmatrix}, \qquad (7)$$

where the wave vector $\mathbf{q}$ is measured from the crossing point. One notes that in the direction perpendicular to the screw axis, i.e. in the q_x-q_y plane, the dispersion is the same as that for the isospin-1 triplet fermion in Eq. (6). In other words, the triply-degenerate fermions basically inherit the structure of the triplet fermion but acquire one more degree of freedom, i.e., motion along the *z*-direction. Meanwhile, their helicities are no longer strictly defined.

We stress that the two fermions discussed here, i.e., the isospin-1 triplet fermion and triply-degenerate fermion, are new quasiparticles. Unlike the Dirac and Weyl fermions, these fermions do not have a direct analogue in relativistic quantum field theory. Also, the isospin-1 triplet fermion point is not topologically protected, except that it marks the onset of a quantum phase transition. In contrast, the two triply-degenerate fermion points are protected by the nontrivial band topology as a result of the fourfold screw axis.

If one breaks the screw-rotational symmetry, the double-degeneracy of the E band will be lifted and the triply-degenerate fermions will disappear. However, the original A and E bands still have different characters under the mirror operations, $\mathrm{M_{xz}}$ and $\mathrm{M_{yz}}$. As such, crossings between each of the split E band and the A band in the mirror-invariant k_x-k_z and k_y-k_z planes will still be protected, as long as the respective mirror symmetry is intact. For instance, by an additional uniaxial strain along

x or along diagonal in the x-y plane, the resulting band crossings form two orthogonal concatenated Weyl loops with the topology of a Hopf-link. As an example, consider a tensile strain along x. Figure 21(c) shows that one Weyl loop is centered at Γ point lying in the k_x-k_z plane, while the other is centered at Z point lying in the k_y-k_z plane. It needs to be emphasized that a band crossing here only results in Weyl loop fermions, but not Weyl fermions, because the inversion symmetry is still intact. It should also be noted that there is no symmetry to pin these Weyl loops at a fixed energy, and indeed, along a loop the energy varies[202].

Nexus network in carbon honeycomb structures

The CHC structures in Fig. 8 also exhibit exotic fermions, as can be seen in Fig. 22, where Fig. 22(a) shows the band structure of CHC-1 along $\Gamma - A$ (in the k_z-direction)[434]. At position α (k_z = 0.07 π/c and E = 0.50 eV), the green and black bands cross. Again, here we will treat the real spin as a dummy variable because of its negligibly-small spin-orbit coupling. As such, the green band is a doublet, while the black band is singlet. Therefore, α is a triply degenerate point (TP).

There is another TP at k_z = - 0.07 π/c, due to the inversion symmetry[249]. The (green) doublet is a topological nodal line, which connect the two TPs. Due to the crossing at the TPs, however, the solid and dotted (green) doublets belong to different band index: solid = (-1, 0) and dotted = (0, +1), respectively. As can be seen in the schematic plot in Fig. 22(b), the solid nodal lines connect the TPs from the interior of k_z, while the dotted nodal lines connect the TPs from the exterior, namely, passing BZ boundaries in the k_z direction. Moreover, Fig. 22(b) shows that there are three mirror planes $k_y = 0, \pm\sqrt{3}k_x$ and hence there are three sets (denoted by different colors) of equivalent nodal lines 120° apart from each other. To zoom in, Fig. 22(d) shows the (0, +1) nodal lines in one mirror plane (k_y = 0), which form a nexus network. This is a standard connectivity for a nexus phase where the two TPs [to be denoted as nexus points (NPs)] are connected by four solid nodal lines, as well as by four dotted nodal lines.

Seen from Fig. 22(e), there are four (0, +1) nodal lines between the two NPs[434]. Considering periodicity of the BZ, all the lines are actually linked each other and form a closed path. Therefore, the

two NPs are not only connected by a straight line throng Γ (corresponding to the solid green line in Fig. 22(a)), but also by a curved line. The curved line, which goes from one TP through β, Γ, β′ and to the other TP, winds along the entire BZ torus as shown in Fig. 22(e). This kind of connectivity between the two NPs is called winding connectivity. The solid lines in Fig. 22(b) show schematically the NPs and the connecting (0, +1) nodal lines in the first BZ, which form a novel 3D nexus network.

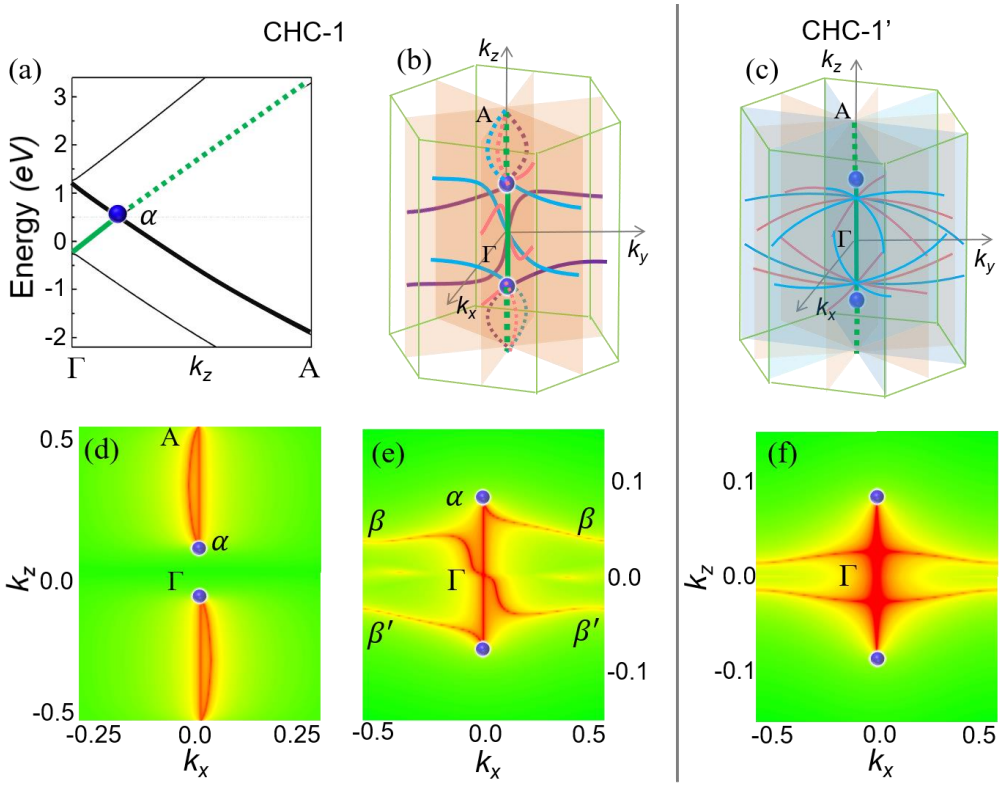

Figure 22. Topological properties of CHC-1 (a, b, d, e) and CHC-1' (c, d). (a) Band structure of CHC-1 along Γ − A consisting of a green doublet and a black singlet band near the E_F. The blue point α is a TP at which the doublet and singlet cross each other. The doublet is the nodal line. Going from Γ to A and before the TP, the nodal line (green solid line) is made of two lower bands, denoted as (-1, 0). After the TP, however, the nodal line (green dotted line) is made of two higher bands, denoted as (0, +1). From the point of view of topology, however, they are two different classes of nodal lines. (b) Schematic illustration of the nexus network of CHC-1 in the first BZ. Solid lines correspond to the (-1, 0) nodal lines, while dotted lines correspond to the (0, +1) nodal lines. Orange planes are three mirror planes. (c) Schematic illustration of nodal lines of CHC-1′ in the first BZ. Here due to the structural change, the nexus network in (b) is replaced by two simple sets of nodal lines along Γ − A. However, additional nodal lines (ANLs) emerge primarily in the k_x-k_y plane (i.e., being "planar"): besides the planar nodal lines associated with three (orange) mirror planes, there is equal number of planar nodal lines associated with three (light-blue) glide planes. They intersect with the nodal lines along Γ − A at k_x-k_y plane. Due to crystal symmetry, these planar nodal lines are also symmetric with respect to k_z axis. (d) Contour map of the energy difference on the k_y = 0 mirror plane of the (0, +1) bands for CHC-1. Red lines are where the energy difference is zero,

i.e., on the nodal lines. The map shows a standard connectivity between the two TPs (also known as NPs). (e) Same as in (d) of the (-1, 0) bands. The zoomed-in view for k_z = (-0.2, 0.2) shows a winding connectivity between the two NPs. (f) Same as in (e) of the (-1, 0) bands for CHC-1′. The zoomed-in view shows that the nodal lines from the two TPs intersect with two ANLs.

When carbon dimerization in CHC-1 [see the orange atoms in Fig. 8(b)] is removed, the structure becomes CHC-*1'* in Fig. 8(c). To see the effect of the de-dimerization, the couture map of CHC-1' is plotted in Fig. 22(f) for $k_y = 0$ in a 1×1×2 supercell to match that of CHC-1. The map reveals a pair of triple points at $k_z = \pm 0.07\ \pi/2c'$ (where c' is the lattice constant of CHC-*1'*), which are connected by the (-1, 0) nodal line. Interestingly, besides the nodal line along k_z, two additional nodal lines along k_x can be seen around $k_z = \pm 0.02\ \pi/2c'$. Here, the structure has a 6-fold screw rotation symmetry. There are therefore 5 additional pairs of equivalent nodal lines on the two mirror planes $k_y = \pm\sqrt{3}k_x$ and on three glide planes $k_x = 0, \pm\sqrt{3}k_y$. The total number of nodal lines not crossing the TPs are therefore 12, as schematically illustrated in Fig. 22(c).

Constrained by the symmetry group and the time reversal symmetry for a spinless system, one obtains a 3×3 $\mathrm{k}\cdot\mathrm{p}$ model around the Γ point[434]:

$$H(\boldsymbol{k}) = \begin{bmatrix} A_1 k_\parallel^2 + B_1 cosk_z + C_1 & \alpha k_+ sink_z + \beta k_-^2 & Dk_- \\ \alpha k_- sink_z + \beta k_+^2 & A_1 k_\parallel^2 + B_1 cosk_z + C_1 & -Dk_+ \\ Dk_+ & -Dk_- & A_2 k_\parallel^2 + B_2 cosk_z + C_2 \end{bmatrix}, \quad (8)$$

where $k_\pm = k_x \pm ik_y$, $k_\parallel^2 = k_x^2 + k_y^2$, and $A_{1,2}$, $B_{1,2}$, $C_{1,2}$, D, α,β are real constants. When $\alpha = \beta = 0$, it describes the triple point phase. When $\alpha = 0$ and $\beta \neq 0$, it describes the triple points and nodal lines phase. Therefore, the effect of the $\beta k_\pm^2$ term is to generate additional nodal lines on the mirror/glide planes. While the effect of the $\alpha k_\pm sink_z$ term is splitting the trivial line in the triple point phase, as this term decreases the structural symmetry. When $\beta = 0$ and $\alpha \neq 0$, it describes a standard nexus-point phase. The nexus network is generated only in the case of $\alpha \neq 0$ and $\beta \neq 0$. This illustrates that the nexus network is a result of the interactions between the standard nexus point phase and additional nodal lines. Note that the $\mathrm{k}\cdot\mathrm{p}$ Hamiltonian above not only reproduces the nexus network in CHC-1, but can also be used to generate other nexus networks which may exist in other real materials as detailed in Ref. [321].

So far, various topological phases have been found in 3D carbon allotropes, from (Dirac, Weyl and triple) nodal points to nodal lines/rings/chains to nodal surfaces. We should also point out that topological phases in 3D carbon allotropes have also been discussed in the studies of Bernal graphite[460], Mackey-Terrones crystal[248], body-centered orthorhombic C_{16}[70] , body-centered tetragonal C_{16}[69] and *m*-C_8[73].

4.5 Extension to boron and beyond

The topological classification of carbon allotropes different from the conventional topological materials is primarily originated from the negligible spin-orbit coupling in carbon materials. Generally speaking, materials consist of light elements should have the same topological classification[461]. For example, the Dirac points or nodal line also can be found in boron, silicon and germanium allotropes[462-467].

Very recently, Feng *et al.* discovered the Dirac fermion in β_{12} boron sheet with the aid of angle-resolved photoemission spectroscopy and first-principle calculations[465]. Chen et al. set out to determine whether a monolayer boron sheet with Dirac fermions was experimentally feasible, and they identified a new boron monolayer consisting of hexagon as well as rhombus stripes[463]. The boron monolayer, which has been called hr-sB, has an exceptional stability and unique Dirac fermions, as shown in Fig. 23(a). Dirac nodal lines and tilted semi-Dirac cones coexist around the E_F, and the Dirac points in the nodal lines are crossed by two linear bands corresponding to two 1D channels in the hexagon and rhombus stripes, respectively. The tilted semi-Dirac cones are present at the tilted axis and anisotropic band crossings, which produces a new kind of Dirac fermions. The unique electronic properties, as a result of the special bonding characteristics, indicate that this boron monolayer may be a good superconductor[463].

By means of systematic first principles computations, Chen et al. also discovered another stable 3D boron allotrope, namely 3D-α' boron, which is a nodal-chain semimetal as shown in Fig. 23(b)[462]. In momentum space, six nodal lines and rings contact each other and form a novel spindle nodal chain [Fig. 23(c)]. The band structure in Fig. 23(d) and PDOS in Fig. 23(e) indicate that the electronic properties of the 3D-α' boron are also dominated by π bonds, similar to the case in 3D graphene

networks. This 3D-α' boron can be formed by stacking 2D wiggle α' boron sheets, which are also nodal-ring semimetals. In addition, our chemical bond analysis revealed that the topological properties of the 3D and 2D boron structures are related to the π bonds between boron atoms, although the bonding characteristics are qualitatively different from those in 2D and 3D carbon structures[462,463].

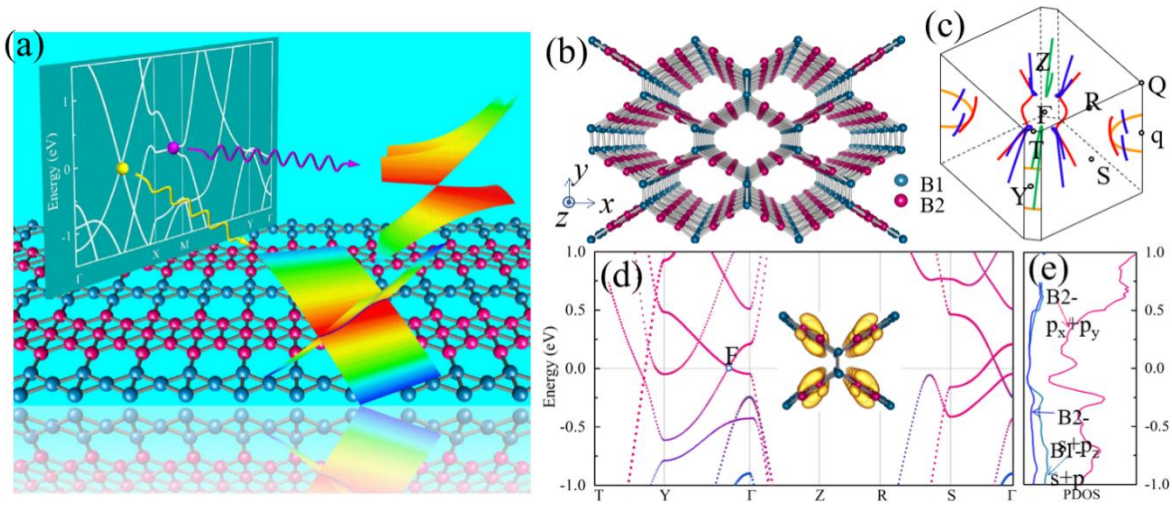

Figure 23. (a) A single layer boron sheet hr-sB possessing Dirac nodal line and tilted Dirac cone. (b) Atomic structure of a boron allotrope 3D-α' boron, which can be formed by stacking 2D wiggle α' boron sheets. (c) Nodal lines in the first BZ of 3D-α' boron. (d-e) Band structures and PDOS of 3D-α' boron, respectively. The inset in (d) shows a charge density for a state at point F.

Silicon and germanium are both belong to group IV elements in the periodic table, same as carbon. Thus, they often have similar physical properties. For example, in the absence of SOC, monolayer freestanding silicene and germanene are both Dirac semimetals[468-471], same as graphene. Because of the relatively heavier cores as well as a structural buckling, however, silicene and germanene have much larger SOCs than that of graphene. As a result, silicene and germanene are both topological insulators[472-474]. Beside the monolayer structure, other silicon and germanium allotropes have also been proposed. Some of them also show topological properties[475-484]. For example, in the absence of SOC, a 2D monolayer T-Ge[485], made of periodic squares and octagons, is a nodal-line semimetal, whose nodal loops are protected by a combination of the spatial inversion P and time reversal T

symmetries. When SOC is considered, it is still a nodal line semimetal, although a small gap is opened along the nodal loop, which is characterized by a nontrivial Z2 invariant and by the existence of topological edge states at the boundaries. Moreover, the nodal-line semimetal states are robust against biaxial strains. Another 2D monolayer silicon allotrope in the literature[486], named Si-Cmma, is also a nodal loop semimetal in the absence of SOC. The nodal loop, protected by a glide mirror, belongs to AI + R within the Altland-Zirnbauer symmetry classes. As to 3D structures, silicene networks similar to the graphene networks with non-trivial topological properties[468,487,488], such as so called cubic diamond Si, AHT-Si24 and VFI-Si36, have also been proposed.

V. Final remarks

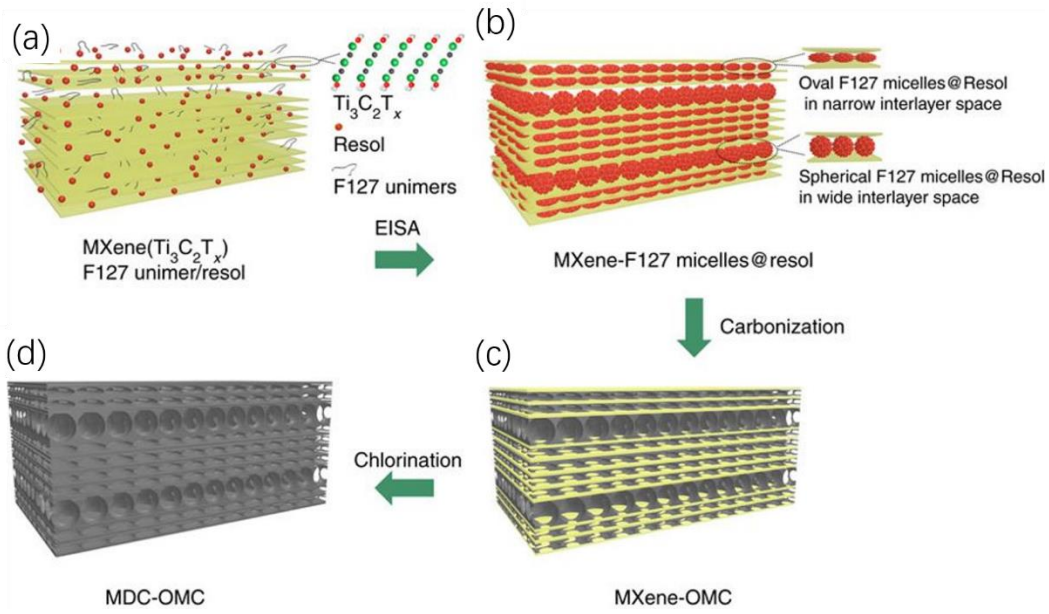

Figure 24. Preparation of the (a) MXene/F127 unimer/resol mixture, (b) MXene-F127 micelles@resol composite, (c) MXene-OMC composite and (d) MDC-OMC composite.

(1) While most of the 3D carbon structures discussed here have not been experimentally synthesized thus far, except for the CHCs, we note that the advancement in MXene-derived carbon [Fig. 24][123] and MOF-derived carbon [Fig. 25][139,338,489] may hold the key for the eventual experimental

realization of 3D topological carbon materials, as such processes may maximally maintain the atomic structures of the carbon skeleton or its derivatives in an orderly fashion. This is especially encouraging given the fact that there are many thousands of MOFs and COFs available to explore. Even the variety of the MXene is considerable. One the flip side, the large variety also calls for a future theoretical investigation of the exotic topological properties of the MOF- and MXene-derived carbon networks and their potential applications.

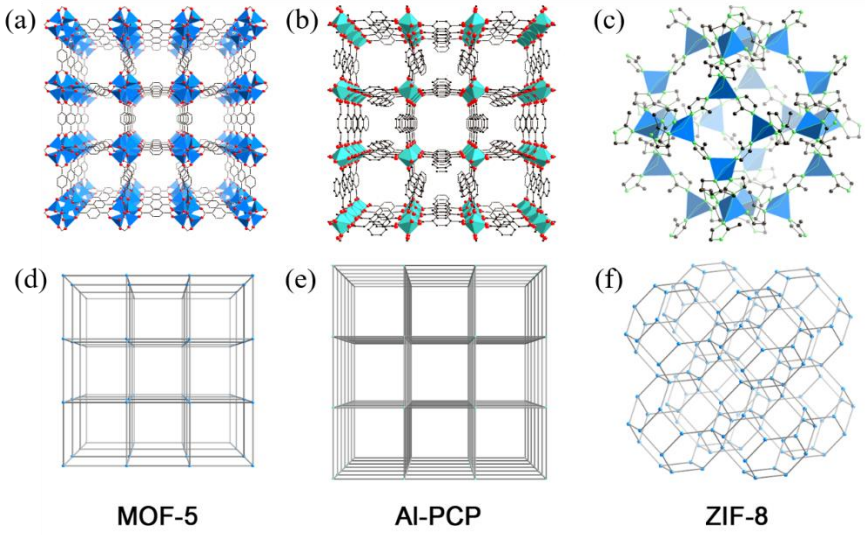

Figure 25. Crystal structures (a-c) and simplified framework structures (d-f) of MOF-5 (Zn4O(1,4-benzenedicarboxylate)3; left), Al-PCP (Al(OH)(1,4-naphthalenedicarboxylate); middle), and ZIF-8 (Zn(2-methylimidazolate)2; right).

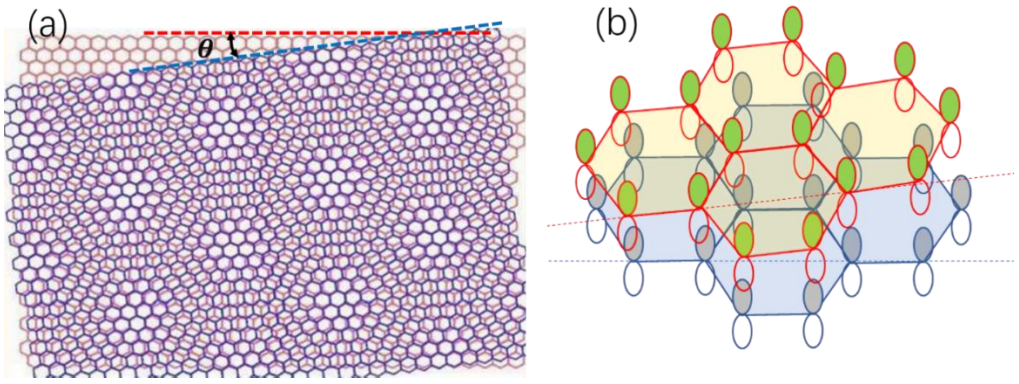

Figure 26. (a) Twisted bilayer graphene, where θ is the twisted angle. (b) A schematic view of p_z orbitals in twisted bilayer graphene.

(2) We note the recent significant surge in the interest and study of twisted graphene[154,490-497]. In retrospect, twisted graphene shares the same orbital physics as the carbon networks elaborated on in

this review article. In particular, both start with the non-trivial orbital topology that manifest as the Dirac cones of a single-layer graphene. However, twisting results in a (more complex) Moiré pattern of the p_z orbitals (see Fig. 26) than what we have here. It has been speculated that in the twisted graphene bilayer a strong interlayer resonance leads to an in-plane localization and hence a flat band[165,498,499]. We, however, feel that the physics of the twisted graphene may resemble the flat band physics of monolayer carbon Kagome lattice discussed in Secs. 2.2 and 4.3, although the exact origin for the wavefunction phase cancelation may differ. Recently, it has been experimentally shown that Kagome lattice indeed form as a result of twisting of a silicene bilayer [Fig. 27], in spite that the twist angle is considerably larger than what has been reported for the twisted graphene bilayer[352].

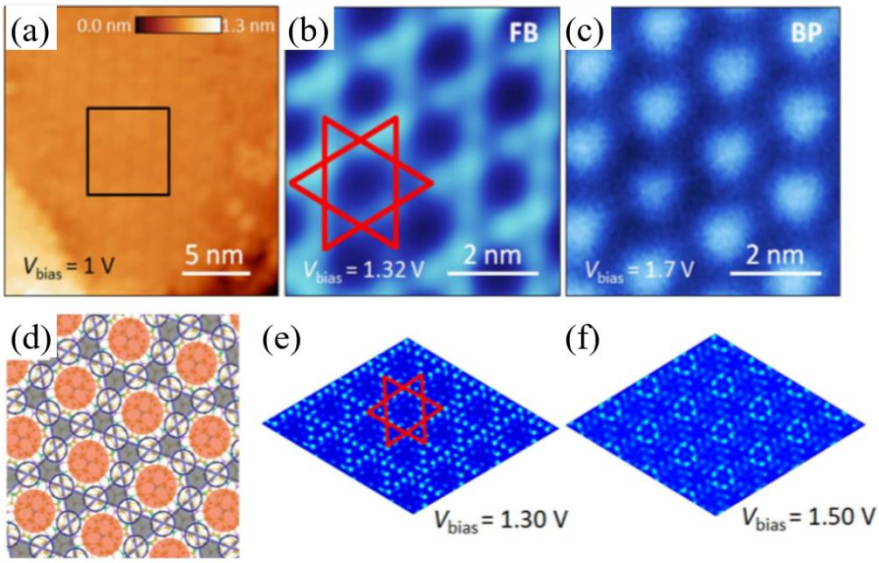

Figure 27. Kagome lattice in twist silicene bilayers.

(3) Besides the topological properties discussed here, which are also known as the first order, recently higher-order TIs has also attracted considerable interests. While the higher orders are classified by different Chern numbers from the first order, physically they represent an expansion of the gaped states at the expense of the gapless states. For example, for a 3D bulk, in the first order, the gapless states cover all the surfaces. In the second order, the gapless states only cover all the edges. On the other hand, in the third order, the gapless states cover only all the corners. For a 2D bulk, in contrast, the first order is featured by gapless edge states, while the second order is featured by gapless corner states. It has been proposed that some of the graphynes discussed earlier are in fact the first

second-order TIs [Fig. 28]. If this is true and since the materials are already been synthesized, they could be the first example of second-order TIs to be experimentally synthesized. Hence, not only the very first-order TI was born in a carbon material, i.e., the graphene, but the second-order TL was born also in a carbon material.

(4) Last but not least, we would like to stress the vital importance of understanding the topological physics in carbon materials, not only because of the unique position of carbon in many technologically-important applications, but also because of its cleanest topological electronic states. Here, only one p orbital participates in the topologically nontrivial gapless states over a wide energy gap of almost 10 eV. In contrast in most of the known topological materials, not only the composition of the gapless states is more than one, but also topological trivial states often dominate over the energy spectrum near the Fermi level. No wonder their silent topological properties must wait for nearly 80 years after the birth of quantum mechanics and 20 years after the quantum Hull effect to be uncovered. Hence, from the point of views of both applications and a thorough understanding of the band topology in condensed matter, we ought to fabricate 3D carbon networks in high quality and characterize them, and the time has come.

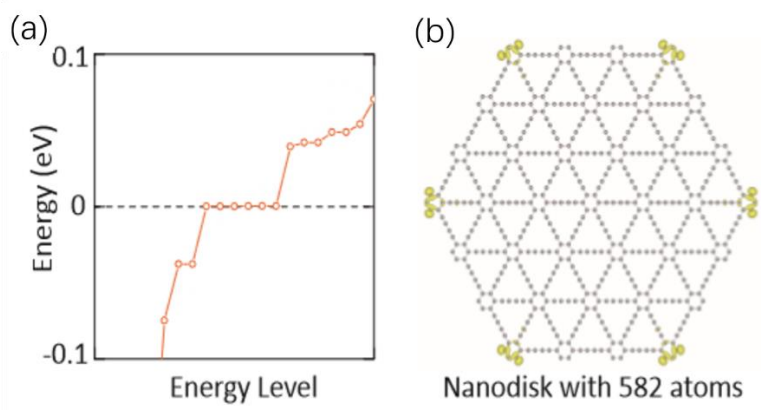

Figure 28. Corner states in graphdiyne. (a) Energy spectrum of the hexagonal-shaped GDY nanodisk shown in (b). The energy levels are plotted in ascending order. (b) also shows the charge distribution of the six zero energy modes, demonstrating that they are localized at corners.

In summary, we have reviewed topological properties and topological phenomena in carbon structures. One can expect that other materials made of light elements possess similar exotic characteristics. In addition, for materials having a larger SOC, if they have the same topological class as the light-element structures in the absence of the SOC, the effects of the SOC may go beyond just

opening band gaps at the band crossings possibly leading to new topological phases unexplored so far. While the review has been focused on topological phases of carbon materials, we can expect that the topological phases will influence other physical properties.

ACKNOWLEDGEMENTS

YPC acknowledges support by the National Natural Science Foundation of China (No. 11874314). MLC acknowledges support from the National Science Foundation Grant No. DMR-1508412 and from the Theory of Materials Program at the Lawrence Berkeley National Lab funded by the Director, Office of Science and Office of Basic Energy Sciences, Materials Sciences and Engineering Division, U.S. Department of Energy under Contract No. DE-AC02-05CH11231. SBZ acknowledges support by U.S. Department of Energy under Grant No. DE-SC0002623.

References

1 Falcao, E. H. & Wudl, F. Carbon allotropes: beyond graphite and diamond. *Journal of Chemical Technology & Biotechnology: International Research in Process, Environmental & Clean Technology* **82**, 524-531 (2007).

2 Zhang, Q., Huang, J. Q., Qian, W. Z., Zhang, Y. Y. & Wei, F. The road for nanomaterials industry: A review of carbon nanotube production, post‐treatment, and bulk applications for composites and energy storage. *Small* **9**, 1237-1265 (2013).

3 Zhang, R.-S. & Jiang, J.-W. The art of designing carbon allotropes. *Frontiers of Physics* **14**, 13401 (2019).

4 Balch, A. L. & Winkler, K. Two-component polymeric materials of fullerenes and the transition metal complexes: A bridge between metal–organic frameworks and conducting polymers. *Chemical reviews* **116**, 3812-3882 (2016).

5 Terrones, M. *et al.* Graphene and graphite nanoribbons: Morphology, properties, synthesis, defects and applications. *Nano today* **5**, 351-372 (2010).

6 Allen, M. J., Tung, V. C. & Kaner, R. B. Honeycomb carbon: a review of graphene. *Chemical reviews* **110**, 132-145 (2009).

7 Yu, L., Shearer, C. & Shapter, J. Recent development of carbon nanotube transparent conductive films. *Chemical reviews* **116**, 13413-13453 (2016).

8 Bonaccorso, F. *et al.* Graphene, related two-dimensional crystals, and hybrid systems for energy conversion and storage. *Science* **347**, 1246501 (2015).

9 Geim, A. K. Graphene: status and prospects. *science* **324**, 1530-1534 (2009).

10 Belenkov, E. A. & Greshnyakov, V. A. Classification schemes for carbon phases and nanostructures. *New Carbon Materials* **28**, 273-282 (2013).

11 Neto, A. C., Guinea, F., Peres, N. M., Novoselov, K. S. & Geim, A. K. The electronic properties of graphene. *Reviews of modern physics* **81**, 109 (2009).

12 Katsnelson, M. I. Graphene: carbon in two dimensions. *Materials today* **10**, 20-27 (2007).

13 Balandin, A. A. Thermal properties of graphene and nanostructured carbon materials. *Nature materials* **10**, 569 (2011).

14 Manna, K., Sun, Y., Muechler, L., Kübler, J. & Felser, C. Heusler, Weyl and Berry. *Nature Reviews Materials*, **3**, 244-256 (2018).

15 Yu, R., Fang, Z., Dai, X. & Weng, H. Topological nodal line semimetals predicted from first-principles calculations. *Frontiers of Physics* **12**, 127202 (2017).

16 Tokura, Y., Yasuda, K. & Tsukazaki, A. Magnetic topological insulators. *Nature Reviews Physics*, **1**, 124-143 (2019).

17 Hasan, M. Z. & Kane, C. L. Colloquium: topological insulators. *Reviews of modern physics* **82**, 3045 (2010).

18 Rachel, S. Interacting topological insulators: a review. *Reports on Progress in Physics* **81**, 116501 (2018).

19 Ren, Y., Qiao, Z. & Niu, Q. Topological phases in two-dimensional materials: a review. *Reports on Progress in Physics* **79**, 066501 (2016).

20 Qi, X.-L. & Zhang, S.-C. Topological insulators and superconductors. *Reviews of Modern Physics* **83**, 1057 (2011).

21 Chiu, C.-K., Teo, J. C., Schnyder, A. P. & Ryu, S. Classification of topological quantum matter with symmetries. *Reviews of Modern Physics* **88**, 035005 (2016).

22 Armitage, N., Mele, E. & Vishwanath, A. Weyl and Dirac semimetals in three-dimensional solids. *Reviews of Modern Physics* **90**, 015001 (2018).

23 Gao, H., Venderbos, J. W., Kim, Y. & Rappe, A. M. Topological Semimetals from first-principles. *arXiv preprint arXiv:1810.08186* (2018).

24 Qi, X.-L., Li, R., Zang, J. & Zhang, S.-C. Inducing a magnetic monopole with topological surface states. *Science* **323**, 1184-1187 (2009).

25 Alicea, J. New directions in the pursuit of Majorana fermions in solid state systems. *Reports on progress in physics* **75**, 076501 (2012).

26 Fang, C., Weng, H., Dai, X. & Fang, Z. Topological nodal line semimetals. *Chinese Physics B* **25**, doi:10.1088/1674-1056/25/11/117106 (2016).

27 Yan, B. & Felser, C. Topological Materials: Weyl Semimetals. *Annual Review of Condensed Matter Physics* **8,** 337-354 (2017).

28 Soluyanov, A. A. *et al.* Type-ii weyl semimetals. *Nature* **527**, 495 (2015).

29 A, A. D. *et al.* Dissipative quantum hall effect in graphene near the Dirac point. *Physical review letters* **98**, 196806 (2007).

30 Yang *et al.* Symmetry demanded topological nodal-line materials. *Advances in Physics: X* **3**, 263-296 (2018).

31 Liang, Z. *et al.* Discovery of a novel spin-polarized nodal ring in a two-dimensional HK lattice. *Nanoscale* **10**, 20748-20753 (2018).

32 Yan, Q. *et al.* Experimental discovery of nodal chains. *Nature Physics* **14,** 461-464 (2018).

33 Zhang, X. *et al.* Nodal loop and nodal surface states in the Ti3Al family of materials. *Physical Review B* **97,** 235150 (2018).

34 Sticlet, D., Piéchon, F., Fuchs, J.-N., Kalugin, P. & Simon, P. Geometrical engineering of a two-band Chern insulator in two dimensions with arbitrary topological index. *Physical Review B* **85,** 165456 (2012).

35 Zhao, L., J, B. E., Heng, F. & M, L. A. Fractional Chern insulators in topological flat bands with higher Chern number. *Physical review letters* **109,** 186805 (2012).

36 Yamakage, A., Imura, K.-I., Cayssol, J. & Kuramoto, Y. Interfacial charge and spin transport in Z2 topological insulators. *Physical Review B* **83,** 125401 (2011).

37 H-M, G. & M, F. Three-dimensional topological insulators on the pyrochlore lattice. *Physical review letters* **103,** 206805 (2009).

38 Jiang, J.-H. Tunable topological Weyl semimetal from simple-cubic lattices with staggered fluxes *Physical Review A* **85,** 033640 (2012).

39 Zyuzin, A. A. & Burkov, A. A. Topological response in Weyl semimetals and the chiral anomaly *Physical Review B* **86,** 115133 (2012).

40 Sukhachov, P. O., Gorbar, E. V., Shovkovy, I. A. & Miransky, V. A. Electronic Properties of Strained Double‐Weyl Systems. *Annalen der Physik* **530,** 1800219 (2018).

41 Moors, K., Zyuzin, A. A., Zyuzin, A. Y., Tiwari, R. P. & Schmidt, T. L. Disorder-driven exceptional lines and Fermi ribbons in tilted nodal-line semimetals. *Physical Review B* **99,** 1-5 (2019).

42 Wang, H., Ruan, J. & Zhang, H. Non-Hermitian nodal-line semimetals with an anomalous bulk-

boundary correspondence. *Physical Review B* **99,** 075130 (2019).

43 Yu, R., Weng, H., Fang, Z., Dai, X. & Hu, X. Topological Node-Line Semimetal and Dirac Semimetal State in Antiperovskite Cu3PdN *Physical review letters* **115,** 036807 (2015).

44 Tateishi, I. & Matsuura, H. Face Centered Cubic SnSe as a Z 2 Trivial Dirac Nodal Line Material. *Journal of the Physical Society of Japan* **87,** 073702 (2018).

45 Hung, L.-Y. & Wen, X.-G. Universal symmetry-protected topological invariants for symmetry-protected topological states. *Physical Review B* **89,** 075121 (2014).

46 Su-Yang, X. *et al.* Observation of Fermi arc surface states in a topological metal. *Science* **347,** 294-298 (2015).

47 Wan, X., Turner, A. M., Vishwanath, A. & Savrasov, S. Y. Topological semimetal and Fermi-arc surface states in the electronic structure of pyrochlore iridates. *Physical Review B* **83,** 205101 (2011).

48 Deng, K. *et al.* Experimental observation of topological Fermi arcs in type-II Weyl semimetal MoTe. *Nature Physics* **12,** 1105-1110 (2016).

49 Hafezi, M., Mittal, S., Fan, J., Migdall, A. & Taylor, J. M. Imaging topological edge states in silicon photonics. *Nature Photonics* **7,** 1001-1005 (2013).

50 Vaezi, A., Liang, Y., Ngai, D. H., Yang, L. & Kim, E.-A. Topological Edge States at a Tilt Boundary in Gated Multilayer Graphene. *Physical Review X* **3,** 021018 (2013).

51 Yin, L.-J., Jiang, H., Qiao, J.-B. & He, L. Direct imaging of topological edge states at a bilayer graphene domain wall. *Nature Communications* **7,** 11760 (2016).

52 Yan, B. & Zhang, S.-C. Topological materials. *Reports on Progress in Physics* **75**, 096501 (2012).

53 Ando, Y. Topological insulator materials. *Journal of the Physical Society of Japan* **82**, 102001 (2013).

54 Bansil, A., Lin, H. & Das, T. Colloquium: Topological band theory. *Reviews of Modern Physics* **88**, 021004 (2016).

55 Klemenz, S., Lei, S. & Schoop, L. M. Topological Semimetals in Square-Net Materials. *Annual Review of Materials Research* **49,** 185-206 (2019).

56 Kane, C. L. & Mele, E. J. Z 2 topological order and the quantum spin Hall effect. *Physical review letters* **95**, 146802 (2005).

57 Novoselov, K. S. *et al.* Two-dimensional gas of massless Dirac fermions in graphene. *nature* **438**, 197 (2005).

58 Park, C.-H., Yang, L., Son, Y.-W., Cohen, M. L. & Louie, S. G. Anisotropic behaviours of massless Dirac fermions in graphene under periodic potentials. *Nature Physics* **4**, 213 (2008).

59 Heikkilä, T. T. & Volovik, G. E. Nexus and Dirac lines in topological materials. *New Journal of Physics* **17**, 093019 (2015).

60 Levin, M. & Stern, A. Fractional topological insulators. *Physical review letters* **103**, 196803 (2009).

61 Analytis, J. G. *et al.* Two-dimensional surface state in the quantum limit of a topological insulator. *Nature Physics* **6**, 960 (2010).

62 Chen, Y. *et al.* Nanostructured carbon allotropes with Weyl-like loops and points. *Nano letters* **15**, 6974-6978 (2015).

63 Tan, L. Z., Park, C.-H. & Louie, S. G. New dirac fermions in periodically modulated bilayer graphene. *Nano letters* **11**, 2596-2600 (2011).

64 Wang, Z. *et al.* Phagraphene: a low-energy graphene allotrope composed of 5–6–7 carbon rings with distorted dirac cones. *Nano letters* **15**, 6182-6186 (2015).

65 Park, M., Kim, Y. & Lee, H. Design of 2D massless Dirac fermion systems and quantum spin Hall insulators based on sp–sp^2 carbon sheets. *npj Computational Materials* **4**, 54 (2018).

66 Liu, Y., Lu, M. & Zhang, M. First-principles study of a novel superhard s p 3 carbon allotrope. *Physics Letters A* **378,** 3326-3330 (2014).

67 Zhang, L. *et al.* Highly anisotropic Dirac fermions in square graphynes. *The journal of physical chemistry letters* **6**, 2959-2962 (2015).

68 Wang, J.-T., Chen, C. & Kawazoe, Y. Topological nodal line semimetal in an orthorhombic graphene network structure. *Physical Review B* **97**, 245147 (2018).

69 Cheng, Y. *et al.* Body‐Centered Tetragonal C16: A Novel Topological Node‐Line Semimetallic Carbon Composed of Tetrarings. *small* **13**, 1602894 (2017).

70 Wang, J.-T. *et al.* Body-centered orthorhombic c 16: A novel topological node-line semimetal. *Physical review letters* **116**, 195501 (2016).

71 Liu, J., Li, X., Wang, Q., Kawazoe, Y. & Jena, P. A new 3D Dirac nodal-line semi-metallic graphene monolith for lithium ion battery anode materials. *Journal of Materials Chemistry A* **6**, 13816-13824 (2018).

72 Feng, X. *et al.* Monoclinic C16: sp2-sp3 hybridized nodal-line semimetal protected by PT-symmetry. *Carbon* **127**, 527-532 (2018).

73 Sung, H.-J., Kim, S., Lee, I.-H. & Chang, K. J. Semimetallic carbon allotrope with a topological nodal line in mixed sp-spsp 2-sp 3 bonding networks. *NPG Asia Materials* **9**, e361 (2017).

74 Lin, Y., Zhao, Z., Strobel, T. A. & Cohen, R. Interpenetrating graphene networks: Three-dimensional node-line semimetals with massive negative linear compressibilities. *Physical Review B* **94**, 245422 (2016).

75 Zhong, C. *et al.* Two-dimensional honeycomb borophene oxide: strong anisotropy and nodal loop transformation. *Nanoscale* **11**, 2468-2475 (2019).

76 Qie, Y., Liu, J., Wang, S., Sun, Q. & Jena, P. Tetragonal C 24: a topological nodal-surface semimetal with potential as an anode material for sodium ion batteries. *Journal of Materials Chemistry A* **7**, 5733-5739 (2019).

77 Zhong, C. *et al.* Towards three-dimensional Weyl-surface semimetals in graphene networks. *Nanoscale* **8**, 7232-7239 (2016).

78 Gao, Y. *et al.* Electron and phonon properties and gas storage in carbon honeycombs. *Nanoscale* **8**, 12863-12868 (2016).

79 Su, W. P., Schrieffer, J. & Heeger, A. J. Solitons in polyacetylene. *Physical review letters* **42**, 1698 (1979).

80 Iijima, S. Helical microtubules of graphitic carbon. *nature* **354**, 56 (1991).

81 Terrones, H. *et al.* New metallic allotropes of planar and tubular carbon. *Physical review letters* **84**, 1716 (2000).

82 Liu, A. Y., Cohen, M. L., Hass, K. & Tamor, M. Structural properties of a three-dimensional all-sp 2 phase of carbon. *Physical Review B* **43**, 6742 (1991).

83 Chiang, C. K. *et al.* Electrical conductivity in doped polyacetylene. *Physical review letters* **39**, 1098 (1977).

84 Shirakawa, H. Nobel lecture: the discovery of polyacetylene film—the dawning of an era of conducting polymers. *Reviews of Modern Physics* **73**, 713 (2001).

85 Guo, X., Lee, W. H., Alvarez, N., Shanov, V. N. & Heineman, W. R. Detection of trace zinc by an electrochemical microsensor based on carbon nanotube threads. *Electroanalysis* **25**, 1599-1604 (2013).

86 Tang, Y. *et al.* Synthesis and characterization of amorphous carbon nanowires. *Applied physics letters* **75**, 2921-2923 (1999).

87 Li, D. & Kaner, R. B. Graphene-based materials. *Science* **320**, 1170-1171 (2008).

88 Meyer, J. C. *et al.* The structure of suspended graphene sheets. *Nature* **446**, 60 (2007).

89 Kim, K. S. *et al.* Large-scale pattern growth of graphene films for stretchable transparent electrodes. *nature* **457**, 706 (2009).

90 Novoselov, K. S. *et al.* Room-temperature quantum Hall effect in graphene. *Science* **315**, 1379-1379 (2007).

91 Du, X., Skachko, I., Barker, A. & Andrei, E. Y. Approaching ballistic transport in suspended graphene. *Nature nanotechnology* **3**, 491 (2008).

92 Zhu, Y. *et al.* Carbon-based supercapacitors produced by activation of graphene. *science* **332**, 1537-1541 (2011).

93 Hwang, E., Adam, S. & Sarma, S. D. Carrier transport in two-dimensional graphene layers. *Physical review letters* **98**, 186806 (2007).

94 Liu, Y. & Chen, X. Mechanical properties of nanoporous graphene membrane. *Journal of Applied Physics* **115**, 034303 (2014).

95 Balandin, A. A. *et al.* Superior thermal conductivity of single-layer graphene. *Nano letters* **8**, 902-907 (2008).

96 Novoselov, K. S. *et al.* Electric field effect in atomically thin carbon films. *science* **306**, 666-669 (2004).

97 Hernandez, Y. *et al.* High-yield production of graphene by liquid-phase exfoliation of graphite. *Nature nanotechnology* **3**, 563 (2008).

98 Chia, J. S. Y. *et al.* A novel one step synthesis of graphene via sonochemical-assisted solvent exfoliation approach for electrochemical sensing application. *Chemical Engineering Journal* **249**, 270-

278 (2014).

99 Huang, N., Lim, H., Chia, C. H., Yarmo, M. A. & Muhamad, M. Simple room-temperature preparation of high-yield large-area graphene oxide. *International journal of nanomedicine* **6**, 3443 (2011).

100 Chen, W., Yan, L. & Bangal, P. R. Preparation of graphene by the rapid and mild thermal reduction of graphene oxide induced by microwaves. *Carbon* **48**, 1146-1152 (2010).

101 Rostrup-Nielsen, J. & Trimm, D. L. Mechanisms of carbon formation on nickel-containing catalysts. *Journal of Catalysis* **48**, 155-165 (1977).

102 Chae, S. J. *et al.* Synthesis of large‐area graphene layers on poly‐nickel substrate by chemical vapor deposition: wrinkle formation. *Advanced materials* **21**, 2328-2333 (2009).

103 Al-Temimy, A., Riedl, C. & Starke, U. Low temperature growth of epitaxial graphene on SiC induced by carbon evaporation. *Applied Physics Letters* **95**, 231907 (2009).

104 Chen, W. & Yan, L. Preparation of graphene by a low-temperature thermal reduction at atmosphere pressure. *Nanoscale* **2**, 559-563 (2010).

105 Reina, A. *et al.* Large area, few-layer graphene films on arbitrary substrates by chemical vapor deposition. *Nano letters* **9**, 30-35 (2008).

106 Gomez De Arco, L. *et al.* Continuous, highly flexible, and transparent graphene films by chemical vapor deposition for organic photovoltaics. *ACS nano* **4**, 2865-2873 (2010).

107 Crespi, V. H., Benedict, L. X., Cohen, M. L. & Louie, S. G. Prediction of a pure-carbon planar covalent metal. *Physical Review B* **53**, R13303 (1996).

108 Schmidt, O. G. & Eberl, K. Nanotechnology: Thin solid films roll up into nanotubes. *Nature* **410**, 168 (2001).

109 Zhang, X. *et al.* Synthesis and characterization of a graphene–C60 hybrid material. *Carbon* **47**, 334-337 (2009).

110 Mandal, B., Sarkar, S., Pramanik, A. & Sarkar, P. Theoretical prediction of a new two-dimensional carbon allotrope and NDR behaviour of its one-dimensional derivatives. *Physical Chemistry Chemical Physics* **15**, 21001-21006 (2013).

114 Charlier, J.-C., Gonze, X. & Michenaud, J.-P. First-principles study of the electronic properties of

graphite. *Physical Review B* **43**, 4579 (1991).

112 Dresselhaus, M., Dresselhaus, G. & Saito, R. Physics of carbon nanotubes. *Carbon* **33**, 883-891 (1995).

113 Barone, V., Hod, O. & Scuseria, G. E. Electronic structure and stability of semiconducting graphene nanoribbons. *Nano letters* **6**, 2748-2754 (2006).

114 Yang, X. *et al.* Two-dimensional graphene nanoribbons. *Journal of the American Chemical Society* **130**, 4216-4217 (2008).

115 Brey, L. & Fertig, H. Electronic states of graphene nanoribbons studied with the Dirac equation. *Physical Review B* **73**, 235411 (2006).

116 Zheng, H., Wang, Z., Luo, T., Shi, Q. & Chen, J. Analytical study of electronic structure in armchair graphene nanoribbons. *Physical Review B* **75**, 165414 (2007).

117 Jaskólski, W., Ayuela, A., Pelc, M., Santos, H. & Chico, L. Edge states and flat bands in graphene nanoribbons with arbitrary geometries. *Physical Review B* **83**, 235424 (2011).

118 Liao, W., Zhou, G. & Xi, F. Optical properties for armchair-edge graphene nanoribbons. *Journal of Applied Physics* **104**, 126105 (2008).

119 Hu, J., Ruan, X. & Chen, Y. P. Thermal conductivity and thermal rectification in graphene nanoribbons: a molecular dynamics study. *Nano letters* **9**, 2730-2735 (2009).

120 Baringhaus, J. *et al.* Exceptional ballistic transport in epitaxial graphene nanoribbons. *Nature* **506**, 349 (2014).

121 Bai, J. *et al.* Very large magnetoresistance in graphene nanoribbons. *Nature nanotechnology* **5**, 655 (2010).

122 Koch, M., Ample, F., Joachim, C. & Grill, L. Voltage-dependent conductance of a single graphene nanoribbon. *Nature nanotechnology* **7**, 713 (2012).

123 Francesco, M. & Antonio, S. First-principles investigations on the functionalization of chiral and non-chiral carbon nanotubes by Diels-Alder cycloaddition reactions. *Physical chemistry chemical physics* **11,** 563-567 (2009).

124 Otani, M., Okada, S. & Oshiyama, A. Energetics and electronic structures of one-dimensional fullerene chains encapsulated in zigzag nanotubes. *Physical Review B* **68,** 125424 (2003).

125 Calvaresi, D. M., Quintana, P. M., Rudolf, P. P., Zerbetto, P. F. & Prato, P. M. Rolling up a Graphene Sheet *ChemPhysChem* **14,** 3447-3453 (2013).

126 Mahan, G. D. & Jeon, G. S. Flexure modes in carbon nanotubes. *Physical Review B* **70,** 075405 (2004).

127 Lim, H. E. *et al.* Growth of carbon nanotubes via twisted graphene nanoribbons. *Nature Communications* **4,** 2548 (2013).

128 Zheng, L. X. *et al.* Ultralong single-wall carbon nanotubes. *Nature Materials* **3,** 673-676 (2004).

129 Schönenberger, C., Bachtold, A., Strunk, C., Salvetat, J.-P. & Forró, L. Interference and Interaction in multi-wall carbon nanotubes. *Applied Physics A Materials Science & Processing* **69,** 283-295 (1999).

130 Charlier, J.-C. & Lambin, P. Electronic structure of carbon nanotubes with chiral symmetry. *Physical Review B* **57,** 15037-15039 (1998).

131 Yevtushenko, O. M., Slepyan, G. Y., Maksimenko, S. A., Lakhtakia, A. & Romanov, D. A. Nonlinear Electron Transport Effects in a Chiral Carbon Nanotube. *Physical review letters* **79,** 1102-1105 (1997).

135 Jain, N., Harsh & Sinha, R. K. Analysis of Electrical Conductance of Carbon Nanotubes. *Advanced Materials Research* **827,** 109-114 (2009).

133 Wei, C., Cho, K. & Srivastava, D. Tensile strength of carbon nanotubes under realistic temperature and strain rate. *Physical Review B* **67,** 115407 (2003).

134 Ogata, S. & Shibutani, Y. Ideal tensile strength and band gap of single-walled carbon nanotubes. *Physical Review B* **68,** 165409 (2003).

135 Sammalkorpi, M., Krasheninnikov, A., Kuronen, A., Nordlund, K. & Kaski, K. Mechanical properties of carbon nanotubes with vacancies and related defects. *Physical Review B* **70,** 1-8 (2004).

136 Song, Y. *et al.* Study of film thickness effect on carbon nanotube based field emission devices. *Journal of Alloys and Compounds* **816,** 152648 (2020).

147 Kwang, H. *et al.* Carbon and metal nanotube hybrid structures on graphene as efficient electron field emitters. *Nanotechnology* **27,** 275301 (2016).

138 Shi, Z. *et al.* Mass-production of single-wall carbon nanotubes by arc discharge method. *Carbon* **37,** 1449-1453 (1999).

139 Su, M., Zheng, B. & Liu, J. A scalable CVD method for the synthesis of single-walled carbon nanotubes with high catalyst productivity. *Chemical Physics Letters* **322,** 321-326 (2000).

140 Yingying, W. *et al.* Stacking-dependent optical conductivity of bilayer graphene. *ACS nano* **4,** 4074-4080 (2010).

141 Tabert, C. J. & Nicol, E. J. Dynamical conductivity of AA-stacked bilayer graphene. *Physical Review B* **86,** 075439 (2012).

142 Huang, Y. C., Chang, C. P. & Lin, M. F. Magnetoabsorption spectra of bilayer graphene ribbons with Bernal stacking. *Physical Review B* **78,** 115422 (2008).

143 Sanderson, M., Ang, Y. S. & Zhang, C. Klein tunneling and cone transport in AA-stacked bilayer graphene. *Physical Review B* **88,** 245404 (2013).

144 Ho, J. H., Lu, C. L., Hwang, C. C., Chang, C. P. & Lin, M. F. Coulomb excitations in AA- and AB-stacked bilayer graphites. *Physical Review B* **74,** 085406 (2006).

145 Kumar, S. & Ajay. Quasi-particle spectrum and density of electronic states in AA- and AB-stacked bilayer graphene. *The European Physical Journal B* **86,** 111 (2013).

146 Gong, X. & Mele, E. J. Stacking textures and singularities in bilayer graphene. *Physical Review B* **89,** 121415 (2014).

147 Chang, X., Ge, Y. & Dong, J. M. Ripples of AA and AB stacking bilayer graphenes. *The European Physical Journal B* **78,** 103-109 (2010).

148 Tao, W., Qing, G., Yan, L. & Kuang, S. A comparative investigation of an AB- and AA-stacked bilayer graphene sheet under an applied electric field: A density functional theory study. *Chinese Physics B* **21,** 069301 (2012).

149 Rafi, B. & H, M. A. Moire bands in twisted double-layer graphene. *Proceedings of the National Academy of Sciences of the United States of America* **108,** 12233-12237 (2011).

150 Uchida, K., Furuya, S., Iwata, J.-I. & Oshiyama, A. Atomic corrugation and electron localization due to Moiré patterns in twisted bilayer graphenes. *Physical Review B* **90,** 155451 (2014).

151 Jacek B Jasinski, Santoshrupa Dumpala, Gamini Sumanasekera, Mahendra K Sunkara & Ouseph, P. J. Observation and interpretation of adjacent Moire patterns of different shapes in bilayer graphene. *Applied Physics Letters* **99,** 073104 (2011).

152 Bistritzer, R. & MacDonald, A. H. Moiré butterflies in twisted bilayer graphene. *Physical Review B* **84,** 035440 (2011).

153 Matthew, Y. *et al.* Tuning superconductivity in twisted bilayer graphene. *Science (New York, N.Y.)***363,** 1059-1064 (2019).

154 Yuan, C. *et al.* Unconventional superconductivity in magic-angle graphene superlattices. *Nature* **556,** 43-50 (2018).

155 L, S. A. *et al.* Emergent ferromagnetism near three-quarters filling in twisted bilayer graphene. *Science (New York, N.Y.)* **365,** 605-608 (2019).

156 J, G. & T, S. Kohn-Luttinger Superconductivity in Twisted Bilayer Graphene. *Physical review letters* **122,** 026801 (2019).

157 Grigory, T., Jura, K. A. & Ashvin, V. Origin of Magic Angles in Twisted Bilayer Graphene. *Physical review letters* **122,** 106405 (2019).

158Alexander, K. *et al.* Maximized electron interactions at the magic angle in twisted bilayer graphene. *Nature* **572,** 95-100 (2019).

159 Yoo, H. *et al.* Atomic and electronic reconstruction at the van der Waals interface in twisted bilayer graphene. *Nature Materials* **18,** 448-453 (2019).

160 Mele, E. J. Commensuration and interlayer coherence in twisted bilayer graphene. *Physical Review B* **81,** 161405 (2010).

161 Morell, E. S., Correa, J. D., Vargas, P., Pacheco, M. & Barticevic, Z. Flat bands in slightly twisted bilayer graphene: Tight-binding calculations. *Physical Review B* **82,** 121407 (2010).

162 Moon, P. & Koshino, M. Optical absorption in twisted bilayer graphene. *Physical Review B* **87,** 205404 (2013).

163 Cocemasov, A. I., Nika, D. L. & Balandin, A. A. Phonons in twisted bilayer graphene. *Physical Review B* **88,** 035428 (2013).

164 W, H. R., Houlong, Z., Lola, B., G, H. R. & Jiwoong, P. Angle-resolved Raman imaging of interlayer rotations and interactions in twisted bilayer graphene. *Nano letters* **12,** 3162-3167 (2012).

165 Koshino, M. *et al.* Maximally Localized Wannier Orbitals and the Extended Hubbard Model for Twisted Bilayer Graphene. *Physical Review X* **8,** 031087 (2018).

166 Moon, P. & Koshino, M. Energy spectrum and quantum Hall effect in twisted bilayer graphene. *Physical Review B* **85,** 195458 (2012).

167 Malko, D., Neiss, C., Vines, F. & Görling, A. Competition for graphene: graphynes with direction-dependent dirac cones. *Physical review letters* **108**, 086804 (2012).

168 Puigdollers, A. R., Alonso, G. & Gamallo, P. First-principles study of structural, elastic and electronic properties of α-, β-and γ-graphyne. *Carbon* **96**, 879-887 (2016).

169 Kim, H., Kim, Y., Kim, J. & Kim, W. Y. Computational searching for new stable graphyne structures and their electronic properties. *Carbon* **98**, 404-410 (2016).

170 Perkgöz, N. K. & Sevik, C. Vibrational and thermodynamic properties of α-, β-, γ-, and 6, 6, 12-graphyne structures. *Nanotechnology* **25**, 185701 (2014).

171 Yin, W.-J. *et al.* R-graphyne: a new two-dimensional carbon allotrope with versatile Dirac-like point in nanoribbons. *Journal of Materials Chemistry A* **1**, 5341-5346 (2013).

172 Nulakani, N. V. R. & Subramanian, V. A theoretical study on the design, structure, and electronic properties of novel forms of graphynes. *The Journal of Physical Chemistry C* **120**, 15153-15161 (2016).

173 Malko, D., Neiss, C. & Görling, A. Two-dimensional materials with Dirac cones: Graphynes containing heteroatoms. *Physical Review B* **86**, 045443 (2012).

174 Ni, Y. *et al.* The transport properties and new device design: the case of 6, 6, 12-graphyne nanoribbons. *Nanoscale* **5**, 4468-4475 (2013).

175 Ding, H., Bai, H. & Huang, Y. Electronic properties and carrier mobilities of 6, 6, 12-graphyne nanoribbons. *AIP Advances* **5**, 077153 (2015).

176 Shabalin, I. L. in *Ultra-high temperature materials I* 7-235 (Springer, 2014).

177 Kang, J., Li, J., Wu, F., Li, S.-S. & Xia, J.-B. Elastic, electronic, and optical properties of two-dimensional graphyne sheet. *The Journal of Physical Chemistry C* **115**, 20466-20470 (2011).

178 Kang, B., Liu, H. & Lee, J. Y. Oxygen adsorption on single layer graphyne: a DFT study. *Physical Chemistry Chemical Physics* **16**, 974-980 (2014).

179 Mortazavi, B., Shahrokhi, M., Rabczuk, T. & Pereira, L. F. C. Electronic, optical and thermal properties of highly stretchable 2D carbon Ene-yne graphyne. *Carbon* **123**, 344-353 (2017).

180 Ouyang, T. *et al.* Thermal transport in graphyne nanoribbons. *Physical Review B* **85**, 235436

(2012).

181 Ram, B. & Mizuseki, H. Tetrahexcarbon: A two-dimensional allotrope of carbon. *Carbon* **137**, 266-273 (2018).

182 Karaush, N. N., Baryshnikov, G. V. & Minaev, B. F. DFT characterization of a new possible graphene allotrope. *Chemical Physics Letters* **612**, 229-233 (2014).

183 Wang, X.-Q., Li, H.-D. & Wang, J.-T. Prediction of a new two-dimensional metallic carbon allotrope. *Physical Chemistry Chemical Physics* **15**, 2024-2030 (2013).

184 Yi, W.-c., Liu, W., Botana, J., Liu, J.-y. & Miao, M.-s. Microporosity as a new property control factor in graphene-like 2D allotropes. *Journal of Materials Chemistry A* **6**, 10348-10353 (2018).

185 Chen, Y. *et al.* Ferromagnetism and Wigner crystallization in kagome graphene and related structures. *Physical Review B* **98**, 035135 (2018).

186 Liu, Y., Wang, G., Huang, Q., Guo, L. & Chen, X. Structural and electronic properties of T graphene: a two-dimensional carbon allotrope with tetrarings. *Physical review letters* **108**, 225505 (2012).

187 Cohen, M. L. Calculation of bulk moduli of diamond and zinc-blende solids. *Physical Review B* **32**, 7988 (1985).

188 Bernal, J. D. The structure of graphite. *Proceedings of the Royal Society of London. Series A, Containing Papers of a Mathematical and Physical Character* **106**, 749-773 (1924).

189 Mounet, N. & Marzari, N. First-principles determination of the structural, vibrational and thermodynamic properties of diamond, graphite, and derivatives. *Physical Review B* **71,** 205214 (2005).

190 Kennedy, C. S. & Kennedy, G. C. The equilibrium boundary between graphite and diamond. *Journal of Geophysical Research* **81,** 2467-2470 (1976).

191 Clifford Frondel & Marvin, U. B. Lonsdaleite, a Hexagonal Polymorph of Diamond. *Nature* **214,** 587-589 (1967).

192 Péter, N. *et al.* Lonsdaleite is faulted and twinned cubic diamond and does not exist as a discrete material. *Nature communications* **5,** 5447 (2014).

193 Jian-Tao, W., Changfeng, C., Enge, W. & Yoshiyuki, K. A new carbon allotrope with six-fold helical chains in all-sp2 bonding networks. *Scientific reports* **4,** 4339 (2014).

194 Diudea, M. V., Nagy, C. L. & Ilić, A. Diamond D5, a Novel Class of Carbon Allotropes. *Carbon Materials: Chemistry and Physics,* 273–289 (2011).

195 Burchfield, L. A., Fahim, M. A., Wittman, R. S., Delodovici, F. & Manini, N. Novamene: A new class of carbon allotropes. *Heliyon* **3,** e00242 (2017).

196 Chun-Yao, N., Xin-Quan, W. & Jian-Tao, W. K6 carbon: a metallic carbon allotrope in sp3 bonding networks. *The Journal of chemical physics* **140,** 054514 (2014).

197 Li, D. *et al.* Modulated T carbon-like carbon allotropes: an ab initio study. *RSC Advances* **4,** 17364-17369 (2014).

198 Selli, D., Baburin, I. A., Martoňák, R. & Leoni, S. Superhard sp3 carbon allotropes with odd and even ring topologies. *Physical Review B* **84,** 161411-1-161411-5 (2011).

199 Chaoyu, H. *et al.* Four superhard carbon allotropes: a first-principles study. *Physical chemistry chemical physics : PCCP* **14,** 8410-8414 (2012).

200 Komatsu, K., Fujiwara, K., Tanaka, T. & Murata, Y. The fullerene dimer C 120 and related carbon allotropes. *Carbon* **38,** 1529-1534 (2000).

201 Xian-Lei, S., Qing-Bo, Y., Fei, Y., Qing-Rong, Z. & Gang, S. T-carbon: a novel carbon allotrope. *Physical review letters* **106,** 155703 (2011).

202 Zhong, C. *et al.* Three-dimensional Pentagon Carbon with a genesis of emergent fermions. *Nature Communications* **8,** 15641 (2017).

203 Li, Q. *et al.* Superhard Monoclinic Polymorph of Carbon. *Physical Review Letters* **102,** 175506-17510 (2009).

204 Jian-Tao, W., Changfeng, C. & Yoshiyuki, K. Low-temperature phase transformation from graphite to sp3 orthorhombic carbon. *Physical review letters* **106,** 075501 (2011).

205 He, C. *et al.* New superhard carbon phases between graphite and diamond. *Solid State Communications* **152,** 1560-1563 (2012).

206 Ramdas, A., Rodriguez, S., Grimsditch, M., Anthony, T. & Banholzer, W. Effect of isotopic constitution of diamond on its elastic constants: C 13 diamond, the hardest known material. *Physical review letters* **71**, 189-192 (1993).

207 Zhao, J., Wei, N., Fan, Z., Jiang, J.-W. & Rabczuk, T. The mechanical properties of three types of

carbon allotropes. *Nanotechnology* **24,** 095702 (2013).

208 Kim, B. G., Sim, H. & Park, J. C4 Carbon allotropes with triple-bonds predicted by first-principles calculations. *Solid State Communications* **169,** 50-56 (2013).

209 Kuc, A. & Seifert, G. Hexagon-preserving carbon foams: Properties of hypothetical carbon allotropes. *Physical Review B* **74,** 214104 (2006).

210 V A Saleev, A V Shipilova. Optical properties of lowest-energy carbon allotropes from the first-principles calculations. *Computer Optics* **41,** 476-483 (2017).

211 Li, Z., Gao, F. & Xu, Z. Strength, hardness, and lattice vibrations of Z-carbon and W-carbon: first-principles calculations. *Physical Review B* **85**, 144115 (2012).

212 Zhao, Z. *et al.* Novel superhard carbon: C-centered orthorhombic C 8. *Physical review letters* **107**, 215502 (2011).

213 Umemoto, K., Wentzcovitch, R. M., Saito, S. & Miyake, T. Body-Centered Tetragonal C 4: A Viable s p 3 Carbon Allotrope. *Physical review letters* **104**, 125504 (2010).

214 Chen, X.-Q., Niu, H., Franchini, C., Li, D. & Li, Y. Hardness of T-carbon: Density functional theory calculations. *Physical Review B* **84**, 121405 (2011).

215 Krainyukova, N. V. Capturing gases in carbon honeycomb. *Journal of Low Temperature Physics* **187**, 90-104 (2017).

216 Hu, M. *et al.* Low-energy 3D sp 2 carbons with versatile properties beyond graphite and graphene. *Dalton Transactions* **47**, 6233-6239 (2018).

217 Fthenakis, Z. G. Are the experimentally observed 3-dimensional carbon honeycombs all-sp 2 structures? The dangling p-orbital instability. *RSC Advances* **7**, 9790-9794 (2017).

218 Chen, Y. *et al.* Carbon kagome lattice and orbital-frustration-induced metal-insulator transition for optoelectronics. *Physical review letters* **113**, 085501 (2014).

219 Wang, J.-T., Nie, S., Weng, H., Kawazoe, Y. & Chen, C. Topological nodal-net semimetal in a graphene network structure. *Physical review letters* **120**, 026402 (2018).

220 Krainyukova, N. V. & Zubarev, E. N. Carbon honeycomb high capacity storage for gaseous and liquid species. *Physical review letters* **116**, 055501 (2016).

221 Hu, M. *et al.* Compressed glassy carbon: An ultrastrong and elastic interpenetrating graphene

network. *Science advances* **3**, e1603213 (2017).

222 Sharma, S. Glassy Carbon: A Promising Material for Micro-and Nanomanufacturing. *Materials* **11**, 1857 (2018).

223 Wei, Q., Zhang, Q., Yan, H., Zhang, M. & Wei, B. A new tetragonal superhard metallic carbon allotrope. *Journal of Alloys and Compounds* **769**, 347-352 (2018).

224 Liu, Y., Jiang, X., Fu, J. & Zhao, J. New metallic carbon: Three dimensionally carbon allotropes comprising ultrathin diamond nanostripes. *Carbon* **126**, 601-610 (2018).

225 Li, Z. *et al.* Superhard superstrong carbon clathrate. *Carbon* **105**, 151-155 (2016).

226 Wei, Q. *et al.* A new superhard carbon allotrope: Orthorhombic C20. *Physics Letters A* **382**, 1685-1689 (2018).

227 Pan, Y. *et al.* A superhard sp3 microporous carbon with direct bandgap. *Chemical Physics Letters* **689**, 68-73 (2017).

228 Liu, J., Zhao, T., Zhang, S. & Wang, Q. A new metallic carbon allotrope with high stability and potential for lithium ion battery anode material. *Nano energy* **38**, 263-270 (2017).

229 Wu, X. *et al.* Superhard three-dimensional carbon with metallic conductivity. *Carbon* **123**, 311-317 (2017).

230 Pan, Y. *et al.* Multithreaded conductive carbon: 1D conduction in 3D carbon. *Carbon* **115**, 584-588 (2017).

231 Chaikittisilp, W., Ariga, K. & Yamauchi, Y. A new family of carbon materials: synthesis of MOF-derived nanoporous carbons and their promising applications. *Journal of Materials Chemistry A* **1**, 14-19 (2013).

232 Wang, J. *et al.* Hierarchical porous carbons with layer-by-layer motif architectures from confined soft-template self-assembly in layered materials. *Nature communications* **8**, 15717 (2017).

233 Li, M., Zhang, X. & Zhao, Y. Superdense tI12 carbon: Unexpectedly high elastic moduli but low ideal strength. *Physics Letters A* **382**, 3125-3130 (2018).

234 Cui, H.-J. *et al.* The geometric and electronic transitions in body-centered-tetragonal C8: A first principle study. *Carbon* **120**, 89-94 (2017).

235 Cheng, C., Lv, Z.-L., Cheng, Y., Chen, X.-R. & Cai, L.-C. A possible superhard orthorhombic

carbon. *Diamond and Related Materials* **43**, 49-54 (2014).

236 Pang, D.-D. *et al.* Properties of a predicted tetragonal carbon allotrope: First principles study. *Diamond and Related Materials* **82**, 50-55 (2018).

237 Nulakani, N. V. R. & Subramanian, V. Superprismane: A porous carbon allotrope. *Chemical Physics Letters* **715**, 29-33 (2019).

238 Lv, Z.-L., Cui, H.-L., Wang, H., Li, X.-H. & Ji, G.-F. Theoretical study of the elasticity, ideal strength and thermal conductivity of a pure sp2 carbon. *Diamond and Related Materials* **71**, 73-78 (2017).

239 Hu, M. *et al.* Three dimensional graphdiyne polymers with tunable band gaps. *Carbon* **91**, 518-526 (2015).

240 Bu, H., Zhao, M., Wang, A. & Wang, X. First-principles prediction of the transition from graphdiyne to a superlattice of carbon nanotubes and graphene nanoribbons. *Carbon* **65**, 341-348 (2013).

241 Gao, X. & Shen, X. Face-to-face crosslinking of graphdiyne and related carbon sheets toward integrated graphene nanoribbon arrays. *Carbon* **125**, 536-543 (2017).

242 Zhang, Z. *et al.* Nanomechanics of carbon honeycomb cellular structures. *Carbon* **113**, 26-32 (2017).

243 Costa, D. G., Henrique, F. J., Oliveira, F. L., Capaz, R. B. & Esteves, P. M. n-Diamondynes: Expanding the family of carbon allotropes. *Carbon* **136**, 337-344 (2018).

244 Crassee, I., Sankar, R., Lee, W.-L., Akrap, A. & Orlita, M. 3D Dirac semimetal Cd3As2: A review of material properties. *Physical Review Materials.***2,** 120302 (2018).

245 Bai, Y. *et al.* First-principles investigation in the Raman and infrared spectra of sp3 carbon allotropes. *Carbon* **78**, 70-78 (2014).

246 He, C. & Zhong, J. M585, a low energy superhard monoclinic carbon phase. *Solid State Communications* **181**, 24-27 (2014).

247 Yang, X. *et al.* Novel Superhard s p 3 Carbon Allotrope from Cold-Compressed C 70 Peapods. *Physical review letters* **118**, 245701 (2017).

248 Weng, H. *et al.* Topological node-line semimetal in three-dimensional graphene networks.

Physical Review B **92**, 045108 (2015).

249 Fu, L. & Kane, C. L. Topological insulators with inversion symmetry. *Physical Review B* **76**, 045302 (2007).

250 Burkov, A. Topological semimetals. *Nature materials* **15**, 1145 (2016).

251 Samarth, N. Quantum materials discovery from a synthesis perspective. *Nature materials* **16**, 1068 (2017).

252 Feng, W. & Yao, Y. Three-dimensional topological insulators: A review on host materials. *Science China Physics, Mechanics and Astronomy* **55**, 2199-2212 (2012).

253 Weng, H., Dai, X. & Fang, Z. Topological semimetals predicted from first-principles calculations. *Journal of Physics: Condensed Matter* **28**, 303001 (2016).

254 Yang, S. A.Dirac and Weyl Materials: Fundamental Aspects and Some Spintronics Applications. 6, 1640003 (World Scientific).

255 Lu, L., Joannopoulos, J. D. & Soljačić, M. Topological photonics. *Nature Photonics* **8**, 821 (2014).

256 Barik, R. K., Shinde, R. & Singh, A. K. Multiple triple-point fermions in Heusler compounds. *Journal of Physics: Condensed Matter* **30**, 375702 (2018).

257 Türker, O. & Moroz, S. Weyl nodal surfaces. *Physical Review B* **97**, 075120 (2018).

258 Lu, L. *et al.* Experimental observation of Weyl points. *Science* **349**, 622-624 (2015).

259 Liu, Z. *et al.* A stable three-dimensional topological Dirac semimetal Cd 3 As 2. *Nature materials* **13**, 677 (2014).

260 Liu, Z. *et al.* Discovery of a three-dimensional topological Dirac semimetal, Na3Bi. *Science* **343**, 864-867 (2014).

261 Young, S. M. *et al.* Dirac semimetal in three dimensions. *Physical review letters* **108**, 140405 (2012).

262 Yang, H. *et al.* Prediction of triple point fermions in simple half-Heusler topological insulators. *Physical review letters* **119**, 136401 (2017).

263 Xie, Y., Cai, J., Kim, J., Chang, P.-Y. & Chen, Y. Hopf-chain networks evolved from triple points. *Physical Review B* **99**, 165147 (2019).

264 Zhu, Z., Winkler, G. W., Wu, Q., Li, J. & Soluyanov, A. A. Triple point topological metals.

Physical Review X **6**, 031003 (2016).

265 Xiao, M., Lin, Q. & Fan, S. Hyperbolic Weyl point in reciprocal chiral metamaterials. *Physical review letters* **117**, 057401 (2016).

266 Bradlyn, B. *et al.* Beyond Dirac and Weyl fermions: Unconventional quasiparticles in conventional crystals. *Science* **353**, aaf5037 (2016).

267 Bian, G. *et al.* Topological nodal-line fermions in spin-orbit metal PbTaSe 2. *Nature communications* **7**, 10556 (2016).

268 Huang, H., Liu, J., Vanderbilt, D. & Duan, W. Topological nodal-line semimetals in alkaline-earth stannides, germanides, and silicides. *Physical Review B* **93**, 201114 (2016).

269 Xu, Q., Yu, R., Fang, Z., Dai, X. & Weng, H. Topological nodal line semimetals in the CaP 3 family of materials. *Physical Review B* **95**, 045136 (2017).

270 Li, K., Li, C., Hu, J., Li, Y. & Fang, C. Dirac and nodal line magnons in three-dimensional antiferromagnets. *Physical review letters* **119**, 247202 (2017).

271 Yan, Z. & Wang, Z. Floquet multi-Weyl points in crossing-nodal-line semimetals. *Physical Review B* **96**, 041206 (2017).

272 Zhang, X., Jin, L., Dai, X. & Liu, G. Topological type-II nodal line semimetal and Dirac semimetal state in stable kagome compound Mg3Bi2. *The journal of physical chemistry letters* **8**, 4814-4819 (2017).

273 Li, C. *et al.* Rules for phase shifts of quantum oscillations in topological nodal-line semimetals. *Physical review letters* **120**, 146602 (2018).

274 Schoop, L. M. *et al.* Dirac cone protected by non-symmorphic symmetry and three-dimensional Dirac line node in ZrSiS. *Nature communications* **7**, 11696 (2016).

275 Huang, H., Jin, K.-H. & Liu, F. Topological nodal-line semimetal in nonsymmorphic Cmce-phase Ag 2 S. *Physical Review B* **96**, 115106 (2017).

276 Wang, J. Antiferromagnetic topological nodal line semimetals. *Physical Review B* **96**, 081107 (2017).

277 Gao, L. *et al.* Epitaxial Growth of Honeycomb Monolayer CuSe with Dirac Nodal Line Fermions. *Advanced Materials* **30**, 1707055 (2018).

278 Sun, J.-P., Zhang, D. & Chang, K. Coexistence of topological nodal lines, Weyl points, and triply degenerate points in TaS. *Physical Review B* **96**, 045121 (2017).

279 Behrends, J., Rhim, J.-W., Liu, S., Grushin, A. G. & Bardarson, J. H. Nodal-line semimetals from Weyl superlattices. *Physical Review B* **96**, 245101 (2017).

280Wang, X.-B. *et al.* Topological surface electronic states in candidate nodal-line semimetal CaAgAs. *Physical Review B* **96**, 161112 (2017).

281 Kawakami, T. & Hu, X. Symmetry-guaranteed nodal-line semimetals in an fcc lattice. *Physical Review B* **96**, 235307 (2017).

282 Niu, C. *et al.* Two-dimensional topological nodal line semimetal in layered X 2 Y (X= Ca, Sr, and Ba; Y= As, Sb, and Bi). *Physical Review B* **95**, 235138 (2017).

283 Chen, H. *et al.* Prediction of two-dimensional nodal-line semimetals in a carbon nitride covalent network. *Journal of Materials Chemistry A* **6**, 11252-11259 (2018).

284 Quan, Y., Yin, Z. & Pickett, W. Single Nodal Loop of Accidental Degeneracies in Minimal Symmetry: Triclinic CaAs 3. *Physical review letters* **118**, 176402 (2017).

285 Yan, Z. *et al.* Nodal-link semimetals. *Physical Review B* **96**, 041103 (2017).

286 Xiao, M., Sun, X.-Q. & Fan, S. Nodal chain semimetal in geometrically frustrated systems. *Physical Review B* **99**, 094206 (2019).

287 Huang, H., Jiang, W., Jin, K.-H. & Liu, F. Tunable topological semimetal states with ultraflat nodal rings in strained YN. *Physical Review B* **98**, 045131 (2018).

288 Shao, D.-F., Zhang, S.-H., Dang, X. & Tsymbal, E. Y. Tunable two-dimensional Dirac nodal nets. *Physical Review B* **98**, 161104 (2018).

289 Gavrilenko, V., Perov, A., Protogenov, A., Turkevich, R. & Chulkov, E. V. Chain of Dirac spectrum loops of nodes in crossed magnetic and electric fields. *Physical Review B* **97**, 115204 (2018).

290 Bzdušek, T., Wu, Q., Rüegg, A., Sigrist, M. & Soluyanov, A. A. Nodal-chain metals. *Nature* **538**, 75 (2016).

291 Zhou, Y., Xiong, F., Wan, X. & An, J. Hopf-link topological nodal-loop semimetals. *Physical Review B* **97**, 155140 (2018).

292 Chang, P.-Y. & Yee, C.-H. Weyl-link semimetals. *Physical Review B* **96**, 081114 (2017).

293 Chen, W., Lu, H.-Z. & Hou, J.-M. Topological semimetals with a double-helix nodal link. *Physical Review B* **96**, 041102 (2017).

294 Bi, R., Yan, Z., Lu, L. & Wang, Z. Nodal-knot semimetals. *Physical Review B* **96**, 201305 (2017).

295 Gong, C., Xie, Y., Chen, Y., Kim, H.-S. & Vanderbilt, D. Symmorphic intersecting nodal rings in semiconducting layers. *Physical review letters* **120**, 106403 (2018).

296 Wang, S.-S., Liu, Y., Yu, Z.-M., Sheng, X.-L. & Yang, S. A. Hourglass Dirac chain metal in rhenium dioxide. *Nature communications* **8**, 1844 (2017).

297 Feng, X., Yue, C., Song, Z., Wu, Q. & Wen, B. Topological Dirac nodal-net fermions in AlB 2-type TiB 2 and ZrB 2. *Physical Review Materials* **2**, 014202 (2018).

298 Yu, W. C. *et al.* Nonsymmorphic cubic Dirac point and crossed nodal rings across the ferroelectric phase transition in LiOsO 3. *Physical Review Materials* **2**, 051201 (2018).

299 Lian, J. *et al.* Multi-loop node line states in ternary MgSrSi-type crystals. *npj Computational Materials* **5**, 10 (2019).

300 Cai, J., Xie, Y., Chang, P.-Y., Kim, H.-S. & Chen, Y.-P. Nodal-chain network, intersecting nodal rings and triple points coexisting in nonsymmorphic Ba3Si4. *Physical Chemistry Chemical Physics* **20**, 21177-21183 (2018).

301 Fu, B.-B. *et al.* Dirac nodal surfaces and nodal lines in ZrSiS. *Science advances* **5**, eaau6459 (2019).

302 Liang, Q.-F., Zhou, J., Yu, R., Wang, Z. & Weng, H. Node-surface and node-line fermions from nonsymmorphic lattice symmetries. *Physical Review B* **93**, 085427 (2016).

303 Bzdušek, T. & Sigrist, M. Robust doubly charged nodal lines and nodal surfaces in centrosymmetric systems. *Physical Review B* **96**, 155105 (2017).

304 Wu, W. *et al.* Nodal surface semimetals: Theory and material realization. *Physical Review B* **97**, 115125 (2018).

305 Basov, D., Averitt, R. & Hsieh, D. Towards properties on demand in quantum materials. *Nature materials* **16**, 1077 (2017).

306 Schaffer, R., Lee, E. K.-H., Yang, B.-J. & Kim, Y. B. Recent progress on correlated electron systems with strong spin–orbit coupling. *Reports on Progress in Physics* **79**, 094504 (2016).

307 Abate, Y. *et al.* Recent progress on stability and passivation of black phosphorus. *Advanced Materials* **30**, 1704749 (2018).

308 Sheng, X.-L., Yu, Z.-M., Yu, R., Weng, H. & Yang, S. A. d orbital topological insulator and semimetal in the antifluorite Cu2S family: Contrasting spin Helicities, nodal box, and hybrid surface states. *The journal of physical chemistry letters* **8**, 3506-3511 (2017).

309 Zhang, X., Jin, L., Dai, X. & Liu, G. Highly anisotropic type-II nodal line state in pure titanium metal. *Applied Physics Letters* **112**, 122403 (2018).

310 Chan, Y.-H., Chiu, C.-K., Chou, M. & Schnyder, A. P. Ca 3 P 2 and other topological semimetals with line nodes and drumhead surface states. *Physical Review B* **93**, 205132 (2016).

311 Son, D. & Spivak, B. Chiral anomaly and classical negative magnetoresistance of Weyl metals. *Physical Review B* **88**, 104412 (2013).

312 Xiong, J. *et al.* Evidence for the chiral anomaly in the Dirac semimetal Na3Bi. *Science* **350**, 413-416 (2015).

313 Li, J. *et al.* Topological quantum catalyst: Dirac nodal line states and a potential electrocatalyst of hydrogen evolution in the TiSi family. *Science China Materials* **61**, 23-29 (2018).

314 Rajamathi, C. R. *et al.* Weyl semimetals as hydrogen evolution catalysts. *Advanced Materials* **29**, 1606202 (2017).

315 Lee, S. R., Sharma, P. A., Lima-Sharma, A. L., Pan, W. & Nenoff, T. M. Topological quantum materials for realizing Majorana quasiparticles. *Chemistry of Materials* **31**, 26-51 (2018).

316 Zhang, C. *et al.* Quantum Hall effect based on Weyl orbits in Cd 3 As 2. *Nature* **565**, 331 (2019).

317 Kong, D. *et al.* Ambipolar field effect in the ternary topological insulator (Bi x Sb 1–x) 2 Te 3 by composition tuning. *Nature nanotechnology* **6**, 705 (2011).

318 He, Q. L. *et al.* Tailoring exchange couplings in magnetic topological-insulator/antiferromagnet heterostructures. *Nature materials* **16**, 94 (2017).

319 Pesin, D. & MacDonald, A. H. Spintronics and pseudospintronics in graphene and topological insulators. *Nature materials* **11**, 409 (2012).

320 Wenchao, T., Wenbo, Y., Jing, S. & Yongkun, W. The Property, Preparation and Application of Topological Insulators: A Review. *Materials (Basel, Switzerland)* **10,** 814 (2017).

321 Schnyder, A. P. & Ryu, S. Topological phases and surface flat bands in superconductors without inversion symmetry. *Physical Review B* **84,** 060504 (2011).

322 Zhang *et al.* Topological insulators in Bi2Se3, Bi2Te3 and Sb2Te3 with a single Dirac cone on the surface. *Nature Physics* **5,** 438-442 (2009).

323 Xia, Y. *et al.* Observation of a large-gap topological-insulator class with a single Dirac cone on the surface. *Nature Physics* **5,** 398-402 (2009).

324 Cayssol, J. Introduction to Dirac materials and topological insulators. *Comptes rendus - Physique* **14,** 760-778 (2013).

325 Huang, H., Zhou, S. & Duan, W. Type-II Dirac fermions in the PtSe 2 class of transition metal dichalcogenides. *Physical Review B* **94**, 121117 (2016).

326 Xiao, R. *et al.* Manipulation of type-I and type-II Dirac points in PdTe 2 superconductor by external pressure. *Physical Review B* **96**, 075101 (2017).

327 Zhang, T.-T. *et al.* From type-II triply degenerate nodal points and three-band nodal rings to type-II Dirac points in centrosymmetric zirconium oxide. *The journal of physical chemistry letters* **8**, 5792-5797 (2017).

328 Park, C.-H., Yang, L., Son, Y.-W., Cohen, M. L. & Louie, S. G. New generation of massless Dirac fermions in graphene under external periodic potentials. *Physical review letters* **101**, 126804 (2008).

329 Nomura, K., Ryu, S., Koshino, M., Mudry, C. & Furusaki, A. Quantum Hall effect of massless Dirac fermions in a vanishing magnetic field. *Physical review letters* **100**, 246806 (2008).

330 Zhou, X., Fang, C., Tsai, W.-F. & Hu, J. Theory of quasiparticle scattering in a two-dimensional system of helical Dirac fermions: Surface band structure of a three-dimensional topological insulator. *Physical Review B* **80**, 245317 (2009).

331 Zhou, S. *et al.* First direct observation of Dirac fermions in graphite. *Nature physics* **2**, 595 (2006).

332 Peres, N., Neto, A. C. & Guinea, F. Dirac fermion confinement in graphene. *Physical Review B* **73**, 241403 (2006).

333 Lee, D.-H. Surface states of topological insulators: The Dirac fermion in curved two-dimensional spaces. *Physical review letters* **103**, 196804 (2009).

334 Li, G. & Andrei, E. Y. Observation of Landau levels of Dirac fermions in graphite. *Nature physics*

3, 623 (2007).

335 Woods, L. M. *et al.* Materials perspective on Casimir and van der Waals interactions. *Reviews of Modern Physics* **88,** 045003 (2016).

336 Kotov, V. N., Uchoa, B., Pereira, V. M., Guinea, F. & Neto, A. H. C. Electron-Electron Interactions in Graphene: Current Status and Perspectives. *Reviews of Modern Physics* **84,** 1067-1125 (2012).

337 Groth, C., Wimmer, M., Akhmerov, A., Tworzydło, J. & Beenakker, C. Theory of the topological Anderson insulator. *Physical review letters* **103**, 196805 (2009).

338 K, L. Z. *et al.* Discovery of a three-dimensional topological Dirac semimetal, Na3Bi. *Science (New York, N.Y.)* **343,** 864-867 (2014).

339 Xu, S. *et al.* Observation of a bulk 3D Dirac multiplet, Lifshitz transition, and nestled spin states in Na3Bi. *arXiv preprint arXiv:1312.7624* (2013).

340 Niu, C. *et al.* Robust dual topological character with spin-valley polarization in a monolayer of the Dirac semimetal Na3Bi. *Physical Review B* **95,** 5 (2017).

341 Kumar, J., Kapoor, P. & Ahluwalia, P. K. Na3Bi: A Robust Material Offering Dirac Electrons for Device Applications. *Journal of Electronic Materials* **44,** 3215-3219 (2015).

342 Du, Y. *et al.* CaTe: a new topological node-line and Dirac semimetal. *npj Quantum Materials* **2,** 3 (2017).

343 Ghimire, N. J., Khan, M. A., Botana, A. S., Jiang, J. S. & Mitchell, J. F. Anisotropic angular magnetoresistance and Fermi surface topology of the candidate novel topological metal Pd3Pb *Physical Review Materials* **2,** 081201 (2018).

344 Pal, P. B. Dirac, majorana, and weyl fermions. *American Journal of Physics* **79**, 485-498 (2011).

345 Jia, S., Xu, S.-Y. & Hasan, M. Z. Weyl semimetals, Fermi arcs and chiral anomalies. *Nature materials* **15**, 1140 (2016).

346 Q, L. B. *et al.* Observation of Fermi-Arc Spin Texture in TaAs. *Physical review letters* **115,** 217601 (2015).

347 Huang, S.-M. *et al.* A Weyl Fermion semimetal with surface Fermi arcs in the transition metal monopnictide TaAs class. *Nature Communications* **6,** 7373 (2015).

348 Su-Yang, X. *et al.* Spin Polarization and Texture of the Fermi Arcs in the Weyl Fermion Semimetal

TaAs. *Physical review letters* **116,** 096801 (2016).

349 Yang, L. X. *et al.* Weyl semimetal phase in the non-centrosymmetric compound TaAs. *Nature Physics* **11,** 728-732 (2015).

350 Yonghui, Z. *et al.* Pressure-Induced New Topological Weyl Semimetal Phase in TaAs. *Physical review letters* **117,** 146402 (2016).

351 Huang, S.-M. *et al.* New type of Weyl semimetal with quadratic double Weyl fermions. *Proceedings of the National Academy of Sciences* **113**, 1180-1185 (2016).

352 Chang, T.-R. *et al.* Prediction of an arc-tunable Weyl Fermion metallic state in Mo x W 1− x Te 2. *Nature communications* **7**, 10639 (2016).

353 Murakami, S. Phase transition between the quantum spin Hall and insulator phases in 3D: emergence of a topological gapless phase. *New Journal of Physics* **9,** 356 (2007).

354 A, B. A. & Leon, B. Weyl semimetal in a topological insulator multilayer. *Physical review letters* **107,** 127205 (2011).

355 Burkov, A. A., Hook, M. D. & Balents, L. Topological nodal semimetals. *Physical Review B* **84,** 235126 (2011).

356 Sun, Y., Wu, S.-C., Ali, M. N., Felser, C. & Yan, B. Prediction of Weyl semimetal in orthorhombic MoTe 2. *Physical Review B* **92**, 161107 (2015).

357 Zhang, C.-L. *et al.* Signatures of the Adler–Bell–Jackiw chiral anomaly in a Weyl fermion semimetal. *Nature communications* **7**, 10735 (2016).

358 Koepernik, K. *et al.* TaIrTe 4: A ternary type-II Weyl semimetal. *Physical Review B* **93**, 201101 (2016).

359 Dai, X., Lu, H.-Z., Shen, S.-Q. & Yao, H. Detecting monopole charge in Weyl semimetals via quantum interference transport. *Physical Review B* **93**, 161110 (2016).

360 Xu, S.-Y. *et al.* Discovery of a Weyl fermion semimetal and topological Fermi arcs. *Science* **349,** 6248 (2015).

361 Noam, M. *et al.* Fermi-arc diversity on surface terminations of the magnetic Weyl semimetal Co3Sn2S2. *Science (New York, N.Y.)* **365,** 1286-1291 (2019).

362 Fulga, I. & Stern, A. Triple point fermions in a minimal symmorphic model. *Physical Review B*

95, 241116 (2017).

363 Furusaki, A. Weyl points and Dirac lines protected by multiple screw rotations. *Science Bulletin* **62**, 788-794 (2017).

364 Pshenay-Severin, D., Ivanov, Y. V., Burkov, A. & Burkov, A. Band structure and unconventional electronic topology of CoSi. *Journal of Physics: Condensed Matter* **30**, 135501 (2018).

365 Cano, J., Bradlyn, B. & Vergniory, M. Multifold nodal points in magnetic materials. *arXiv preprint arXiv:1904.12867* (2019).

366 Song, H., Huang, S.-J., Fu, L. & Hermele, M. Topological phases protected by point group symmetry. *Physical Review X* **7**, 011020 (2017).

367 Ramires, A. & Lado, J. L. Impurity-induced triple point fermions in twisted bilayer graphene. *Physical Review B* **99**, 245118 (2019).

368 Hu, H., Hou, J., Zhang, F. & Zhang, C. Topological Triply Degenerate Points Induced by Spin-Tensor-Momentum Couplings. *Physical review letters* **120**, 240401 (2018).

369 Gao, W. *et al.* A possible candidate for triply degenerate point fermions in trigonal layered PtBi2. *Nature communications* **9,** 3249 (2018).

370 Owerre, S. Magnonic triply-degenerate nodal points. *EPL (Europhysics Letters)* **120**, 57002 (2018).

371 Wang, J.-R., Liu, G.-Z. & Zhang, C.-J. Topological quantum critical point in a triple-Weyl semimetal: Non-Fermi-liquid behavior and instabilities. *Physical Review B* **99**, 195119 (2019).

372 Cheung, C.-H. *et al.* Systematic analysis for triple points in all magnetic symmorphic systems and symmetry-allowed coexistence of Dirac points and triple points. *New Journal of Physics* **20**, 123002 (2018).

373 W.Winkler, G., Singh, S. & A.Soluyanov, A. Topology of triple-point metals *Chinese Physics B* **28**, 58-76 (2019).

374 Kim, J., Kim, H.-S. & Vanderbilt, D. Nearly triple nodal point topological phase in half-metallic GdN. *Physical Review B* **98,** 155122 (2018).

375 Takane, D. *et al.* Dirac-node arc in the topological line-node semimetal HfSiS. *Physical Review B* **94**, 121108 (2016).

376 Takane, D. *et al.* Observation of Dirac-like energy band and ring-torus Fermi surface associated with the nodal line in topological insulator CaAgAs. *npj Quantum Materials* **3**, 1 (2018).

377 Liu, Z., Wang, H., Wang, Z., Yang, J. & Liu, F. Pressure-induced organic topological nodal-line semimetal in the three-dimensional molecular crystal Pd (dddt) 2. *Physical Review B* **97**, 155138 (2018).

378 Salmankurt, B. & Duman, S. First-principles study of structural, mechanical, lattice dynamical and thermal properties of nodal-line semimetals ZrXY (X= Si, Ge; Y= S, Se). *Philosophical Magazine* **97**, 175-186 (2017).

379 Bian, G. *et al.* Drumhead surface states and topological nodal-line fermions in TlTaSe 2. *Physical Review B* **93**, 121113 (2016).

380 Yan, Z. & Wang, Z. Tunable Weyl points in periodically driven nodal line semimetals. *Physical review letters* **117**, 087402 (2016).

381 Feng, B. *et al.* Experimental realization of two-dimensional Dirac nodal line fermions in monolayer Cu 2 Si. *Nature communications* **8**, 1007 (2017).

382 Liu, J. *et al.* Strain-induced nonsymmorphic symmetry breaking and removal of Dirac semimetallic nodal line in an orthoperovskite iridate. *Physical Review B* **93**, 085118 (2016).

383 Hosen, M. M. *et al.* Tunability of the topological nodal-line semimetal phase in ZrSi X-type materials (X= S, Se, Te). *Physical Review B* **95**, 161101 (2017).

384 Yu, R., Wu, Q., Fang, Z. & Weng, H. From nodal chain semimetal to Weyl semimetal in HfC. *Physical review letters* **119**, 036401 (2017).

385 Molina, R. A. & González, J. Surface and 3D quantum Hall effects from engineering of exceptional points in nodal-line semimetals. *Physical review letters* **120**, 146601 (2018).

386 Xie, L. S. *et al.* A new form of Ca3P2 with a ring of Dirac nodes. *Apl Materials* **3**, 083602 (2015).

387 Rhim, J.-W. & Kim, Y. B. Landau level quantization and almost flat modes in three-dimensional semimetals with nodal ring spectra. *Physical Review B* **92**, 045126 (2015).

388 Sun, Y., Zhang, Y., Liu, C.-X., Felser, C. & Yan, B. Dirac nodal lines and induced spin Hall effect in metallic rutile oxides. *Physical Review B* **95**, 235104 (2017).

389 Nandkishore, R. Weyl and Dirac loop superconductors. *Physical Review B* **93**, 020506 (2016).

390 Xu, X. *et al.* Quantum oscillations in the noncentrosymmetric superconductor and topological nodal-line semimetal PbTaSe2. *Physical Review B* **99,** 104516 (2019).

391 He, L. *et al.* Pressure-induced superconductivity in the three-dimensional topological Dirac semimetal Cd3As2.*npj Quantum Materials* **1,** 16014 (2016).

392 Kim, H.-S., Chen, Y. & Kee, H.-Y. Surface states of perovskite iridates AIrO 3: signatures of a topological crystalline metal with nontrivial Z 2 index. *Physical Review B* **91**, 235103 (2015).

393 Chen, Y., Kim, H.-S. & Kee, H.-Y. Topological crystalline semimetals in nonsymmorphic lattices. *Physical Review B* **93**, 155140 (2016).

394 González, J. & Molina, R. Topological protection from exceptional points in Weyl and nodal-line semimetals. *Physical Review B* **96**, 045437 (2017).

395 Hosur, P., Dai, X., Fang, Z. & Qi, X.-L. Time-reversal-invariant topological superconductivity in doped Weyl semimetals. *Physical Review B* **90**, 045130 (2014).

396 Sun, K., Liu, W. V., Hemmerich, A. & Sarma, S. D. Topological semimetal in a fermionic optical lattice. *Nature Physics* **8**, 67 (2012).

397 Chiu, C.-K. & Schnyder, A. P. Classification of reflection-symmetry-protected topological semimetals and nodal superconductors. *Physical Review B* **90**, 205136 (2014).

.98 Ahn, J., Kim, D., Kim, Y. & Yang, B.-J. Band Topology and Linking Structure of Nodal Line Semimetals with Z 2 Monopole Charges. *Physical review letters* **121**, 106403 (2018).

399 Fletcher, J. *et al.* Evidence for a nodal-line superconducting state in LaFePO. *Physical Review Letters* **102**, 147001 (2009).

400 Krüger, F. & Zaanen, J. Fermionic quantum criticality and the fractal nodal surface. *Physical Review B* **78**, 035104 (2008).

401 Takahashi, R., Hirayama, M. & Murakami, S. Spinless hourglass nodal-line semimetals. *Physical Review B* **96**, 155206 (2017).

402 Rauch, T., Minh, H. N., Henk, J. & Mertig, I. Model for ferromagnetic Weyl and nodal line semimetals: Topological invariants, surface states, anomalous and spin Hall effect. *Physical Review B* **96**, 235103 (2017).

403 Chen, C. *et al.* Dirac line nodes and effect of spin-orbit coupling in the nonsymmorphic critical

semimetals M SiS (M= Hf, Zr). *Physical Review B* **95**, 125126 (2017).

404 Sun, J.-P. Topological Nodal Line Semimetal in Non-Centrosymmetric PbTaS. *Chinese Physics Letters* **34**, 077101 (2017).

405 Wang, R. *et al.* Nodal line fermions in magnetic oxides. *Physical Review B* **97**, 241111 (2018).

406 Shapourian, H., Wang, Y. & Ryu, S. Topological crystalline superconductivity and second-order topological superconductivity in nodal-loop materials. *Physical Review B* **97**, 094508 (2018).

407 Yu, J. Measuring Hopf links and Hopf invariants in a quenched topological Raman lattice. *Physical Review A* **99**, 043619 (2019).

408 Ezawa, M. Topological semimetals carrying arbitrary Hopf numbers: Fermi surface topologies of a Hopf link, Solomon's knot, trefoil knot, and other linked nodal varieties. *Physical Review B* **96**, 041202 (2017).

409 Tan, X. *et al.* Demonstration of Hopf-link semimetal bands with superconducting circuits. *Applied Physics Letters* **112**, 172601 (2018).

410 Kobayashi, S. *et al.* Crossing-line-node semimetals: General theory and application to rare-earth trihydrides. *Physical Review B* **95**, 245208 (2017).

411 Lee, C. H. *et al.* Imaging nodal knots in momentum space through topolectrical circuits. *arXiv preprint arXiv:1904.10183* (2019).

412 Sun, X.-Q., Zhang, S.-C. & Bzdušek, T. Conversion rules for Weyl points and nodal lines in topological media. *Physical review letters* **121**, 106402 (2018).

413 Zhou, Y., Xiong, F., Wan, X. & An, J. Hopf-link multi-Weyl-loop topological semimetals. *arXiv preprint arXiv:1801.04169* (2018).

414 Zhang, X., Jin, L., Dai, X., Chen, G. & Liu, G. Ideal inner nodal chain semimetals in Li2XY (X= Ca, Ba; Y= Si, Ge) materials. *The journal of physical chemistry letters* **9**, 5358-5363 (2018).

415 You, J.-Y. *et al.* Carboneyane: A nodal line topological carbon with sp − sp 2 − sp 3 chemical bonds. *Carbon* **152,** 909-914 (2019).

416 Hosen, M. M. *et al.* Experimental observation of drumhead surface states in SrAs3. *Scientific Reports* **10,** 2776 (2020).

417 Mikitik, G. P. & Sharlai, Y. V. Magnetization of topological line-node semimetals. *Physical Review*

B **97,** 085122 (2018).

418 Wang, J. *et al.* Pseudo Dirac nodal sphere semimetal. *Physical Review B* **98**, 201112 (2018).

419 Loos, P.-F. & Bressanini, D. Nodal surfaces and interdimensional degeneracies. *The Journal of chemical physics* **142**, 214112 (2015).

420 Yang, S. A., Li, X., Bristow, A. D. & Sipe, J. E. Second harmonic generation from tetragonal centrosymmetric crystals. *Physical Review B* **80,** 165306 (2009).

421 Morimoto, T. & Furusaki, A. Weyl and Dirac semimetals with Z2 topological charge. *Physical Review B* **89,** 235127 (2014).

422 Zhang, D.-W. *et al.* Quantum simulation of exotic PT-invariant topological nodal loop bands with ultracold atoms in an optical lattice. *Physical Review A* **93,** 043617 (2016).

423 Brzezicki, W., Cuoco, M., Forte, F. & Oleś, A. M. Topological phases emerging from spin-orbital physics. *Journal of Superconductivity and Novel Magnetism* **31**, 639-645 (2018).

424 Zhang, L. *et al.* Structural and electronic properties of germanene on MoS 2. *Physical review letters* **116**, 256804 (2016).

425 Grimme, S., Brandenburg, J. G., Bannwarth, C. & Hansen, A. Consistent structures and interactions by density functional theory with small atomic orbital basis sets. *The Journal of chemical physics* **143**, 054107 (2015).

426 Ridolfi, E., Le, D., Rahman, T., Mucciolo, E. & Lewenkopf, C. A tight-binding model for MoS2 monolayers. *Journal of Physics: Condensed Matter* **27**, 365501 (2015).

427 Liu, M.-H. *et al.* Scalable tight-binding model for graphene. *Physical review letters* **114**, 036601 (2015).

428 Zhu, Q., Oganov, A. R., Salvadó, M. A., Pertierra, P. & Lyakhov, A. O. Denser than diamond: ab initio search for superdense carbon allotropes. *Physical Review B* **83**, 193410 (2011).

429 Yang, L., Park, C.-H., Son, Y.-W., Cohen, M. L. & Louie, S. G. Quasiparticle energies and band gaps in graphene nanoribbons. *Physical Review Letters* **99**, 186801 (2007).

430 Khomyakov, P. *et al.* First-principles study of the interaction and charge transfer between graphene and metals. *Physical Review B* **79**, 195425 (2009).

431 Ortix, C., Yang, L. & van den Brink, J. Graphene on incommensurate substrates: trigonal warping

and emerging Dirac cone replicas with halved group velocity. *Physical Review B* **86**, 081405 (2012).

432 Jiang, X., Zhao, J., Li, Y. L. & Ahuja, R. Tunable Assembly of sp3 Cross‐Linked 3D Graphene Monoliths: A First‐Principles Prediction. *Advanced Functional Materials* **23**, 5846-5853 (2013).

433 Hu, J. *et al.* Three-dimensional honeycomb carbon: Junction line distortion and novel emergent fermions. *Carbon* **141**, 417-426 (2019).

434 Chen, Y. *et al.* Nexus networks in carbon honeycombs. *Physical Review Materials* **2**, 044205 (2018).

435 Greilich, A. *et al.* Optical control of spin coherence in singly charged (In, Ga) As/GaAs quantum dots. *Physical review letters* **96**, 227401 (2006).

436 Cragg, D. M., Sherrington, D. & Gabay, M. Instabilities of an m-Vector Spin-Glass in a Field. *Physical Review Letters* **49**, 158 (1982).

437 Kan, M. *et al.* Tuning magnetic properties of graphene nanoribbons with topological line defects: From antiferromagnetic to ferromagnetic. *Physical Review B* **85**, 155450 (2012).

438 Ruffieux, P. *et al.* On-surface synthesis of graphene nanoribbons with zigzag edge topology. *Nature* **531**, 489 (2016).

439 Güçlü, A. D., Grabowski, M. & Hawrylak, P. Electron-electron interactions and topology in the electronic properties of gated graphene nanoribbon rings in Möbius and cylindrical configurations. *Physical Review B* **87**, 035435 (2013).

440 Gröning, O. *et al.* Engineering of robust topological quantum phases in graphene nanoribbons. *Nature* **560**, 209 (2018).

441 Rizzo, D. J. *et al.* Topological band engineering of graphene nanoribbons. *Nature* **560**, 204 (2018).

442 Cao, T., Zhao, F. & Louie, S. G. Topological phases in graphene nanoribbons: junction states, spin centers, and quantum spin chains. *Physical review letters* **119**, 076401 (2017).

443 Okuyama, R., Izumida, W. & Eto, M. Topology in single-wall carbon nanotube of zigzag and armchair type. *Journal of Physics: Conference Series* **969,** 012137 (2018).

444 Izumida, W., Okuyama, R., Yamakage, A. & Saito, R. Angular momentum and topology in semiconducting single-wall carbon nanotubes. *Physical Review B* **93,** 195442 (2016).

445 Okuyama, R., Izumida, W. & Eto, M. Topological Phase Transition in Metallic Single-Wall

Carbon Nanotube. *Journal of the Physical Society of Japan* **86,** 013702 (2017).

446 Yao, Y., Ye, F., Qi, X.-L., Zhang, S.-C. & Fang, Z. Spin-orbit gap of graphene: First-principles calculations. *Physical Review B* **75**, 041401 (2007).

447 Gomes, K. K., Mar, W., Ko, W., Guinea, F. & Manoharan, H. C. Designer Dirac fermions and topological phases in molecular graphene. *Nature* **483**, 306 (2012).

448 Sigrist, M. & M. Rice, T. Paramagnetic effect in high T c superconductors-a hint for d-wave superconductivity. *Journal of the Physical Society of Japan* **61**, 4283-4286 (1992).

449 Monthoux, P., Balatsky, A. & Pines, D. Toward a theory of high-temperature superconductivity in the antiferromagnetically correlated cuprate oxides. *Physical review letters* **67**, 3448 (1991).

450 Kitaev, A. Periodic table for topological insulators and superconductors. AIP Conference Proceedings. 1134, 22-30 (2009).

451 Gao, Y. *et al.* A class of topological nodal rings and its realization in carbon networks. *Physical Review B* **97**, 121108 (2018).

452 Zyuzin, A. A. & Zyuzin, A. Y. Flat band in disorder-driven non-Hermitian Weyl semimetals. *Physical Review B* **97**, 041203 (2018).

453 Yin, H. *et al.* Stone-Wales graphene: A two-dimensional carbon semimetal with magic stability. *Physical Review B* **99**, 041405 (2019).

454 Kim, B. G. & Choi, H. J. Graphyne: Hexagonal network of carbon with versatile Dirac cones. *Physical Review B* **86**, 115435 (2012).

455 Gülseren, O., Yildirim, T., Ciraci, S. & Kılıç, Ç. Reversible band-gap engineering in carbon nanotubes by radial deformation. *Phys. Rev. B* **65**, 155410 (2002).

456 Schnyder, A. P., Ryu, S., Furusaki, A. & Ludwig, A. W. Classification of topological insulators and superconductors in three spatial dimensions. *Physical Review B* **78**, 195125 (2008).

457 Matsuura, S., Chang, P.-Y., Schnyder, A. P. & Ryu, S. Protected boundary states in gapless topological phases. *New Journal of Physics* **15**, 065001 (2013).

458 Teo, J. C. & Kane, C. L. Topological defects and gapless modes in insulators and superconductors. *Physical Review B* **82**, 115120 (2010).

459 Georgi, H. *Lie algebras in particle physics: from isospin to unified theories*. (CRC Press, 2018).

460 Charlier, J.-C., Michenaud, J.-P. & Gonze, X. First-principles study of the electronic properties of simple hexagonal graphite. *Physical Review B* **46**, 4531 (1992).

461 Fidkowski, L. & Kitaev, A. Effects of interactions on the topological classification of free fermion systems. *Physical Review B* **81**, 134509 (2010).

462 Gao, Y., Xie, Y., Chen, Y., Gu, J. & Chen, Z. Spindle nodal chain in three-dimensional α′ boron. *Physical Chemistry Chemical Physics* **20**, 23500-23506 (2018).

463 Zhang, H. *et al.* Dirac nodal lines and tilted semi-Dirac cones coexisting in a striped boron sheet. *The journal of physical chemistry letters* **8**, 1707-1713 (2017).

464 Gupta, S., Kutana, A. & Yakobson, B. I. Dirac Cones and Nodal Line in Borophene. *The journal of physical chemistry letters* **9**, 2757-2762 (2018).

465 Feng, B. *et al.* Dirac fermions in borophene. *Physical review letters* **118**, 096401 (2017).

466 Ma, F. *et al.* Graphene-like two-dimensional ionic boron with double dirac cones at ambient condition. *Nano letters* **16**, 3022-3028 (2016).

467 Zhou, X.-F. *et al.* Semimetallic two-dimensional boron allotrope with massless Dirac fermions. *Physical Review Letters* **112**, 085502 (2014).

468 Kim, G.-M., Sung, H.-J., Han, W. H., Lee, I.-H. & Chang, K. J. Self-Encapsulation of Silicene in Cubic Diamond Si: Topological Semimetal in Covalent Bonding Networks. *The Journal of Physical Chemistry C* **123**, 1839-1845, doi:10.1021/acs.jpcc.8b10475 (2019).

469 Drummond, N. D., Zólyomi, V. & Fal'ko, V. I. Electrically tunable band gap in silicene. *Physical Review B* **85**, 075423 (2012).

470 Pere, M., Martha, A. & Thomas, H. An atlas of two-dimensional materials. . *Chemical Society reviews* **43**, 6537-6554 (2014).

471 Cahangirov, S., Topsakal, M., Aktürk, E., Şahin, H. & Ciraci, S. Two- and One-Dimensional Honeycomb Structures of Silicon and Germanium. *Physical Review Letters* **102**, 236804 (2009).

472 Rachel, S. & Ezawa, M. Giant magnetoresistance and perfect spin filter in silicene, germanene, and stanene. *Physical Review B* **89**, 195303 (2014).

473 Ezawa, M. Monolayer Topological Insulators: Silicene, Germanene, and Stanene *Journal of the Physical Society of Japan* **84**, 121003 (2015).

474 Ezawa, M. Topological electronics and topological field effect transistor in silicene, germanene and stanene. *IEEE 15th International Conference on Nanotechnology* **1**, 604-608 (2015).

475 Beekman, M., Wei, K. & Nolas, G. S. Clathrates and beyond: Low-density allotropy in crystalline silicon. *Applied Physics Reviews* **3** (2016).

476 Chen, P.-S., Fan, S.-T., Lan, H.-S. & Liu, C. W. Band calculation of lonsdaleite Ge. *Journal of Physics D: Applied Physics* **50**, 015107 (2017).

477 Dimoulas, A. Silicene and germanene: Silicon and germanium in the "flatland". *Microelectronic Engineering* **131**, 68-78, doi:10.1016/j.mee.2014.08.013 (2015).

478 Fan, Q. *et al.* Novel silicon allotropes: Stability, mechanical, and electronic properties. *Journal of Applied Physics* **118**, 185704, doi:10.1063/1.4935549 (2015).

479 Fan, Q., Chai, C., Wei, Q. & Yang, Y. Two novel silicon phases with direct band gaps. *Phys Chem Chem Phys* **18**, 12905-12913, doi:10.1039/c6cp00195e (2016).

480 Fan, Q. *et al.* t-Si64 : A Novel Silicon Allotrope. *Chemphyschem* **20**, 128-133, doi:10.1002/cphc.201800903 (2019).

481 Guo, Y., Wang, Q., Kawazoe, Y. & Jena, P. A New Silicon Phase with Direct Band Gap and Novel Optoelectronic Properties. *Sci Rep* **5**, 14342, doi:10.1038/srep14342 (2015).

482 He, C. *et al.* Direct and quasi-direct band gap silicon allotropes with remarkable stability. *Phys Chem Chem Phys* **18**, 9682-9686, doi:10.1039/c6cp00451b (2016).

483 Matthes, L. & Bechstedt, F. Influence of edge and field effects on topological states of germanene nanoribbons from self-consistent calculations. *Physical Review B* **90**, 165431, doi:10.1103/PhysRevB.90.165431 (2014).

484 Schwarz, U. *et al.* A 3D network of four-bonded germanium: a link between open and dense. *Angew Chem Int Ed Engl* **47**, 6790-6793, doi:10.1002/anie.200800914 (2008).

485 Xu, C., Wang, Y., Han, R., Tu, H. & Yan, Y. Topological node line semimetal state in two-dimensional tetragonal allotrope of Ge and Sn. *New Journal of Physics* **21**, 033005, doi:10.1088/1367-2630/ab0457 (2019).

486 Zhou, N., Zhou, P., Li, J., He, C. & Zhong, J. Si-Cmma: A silicon thin film with excellent stability and Dirac nodal loop. *Physical Review B* **100**, 115425, doi:10.1103/PhysRevB.100.115425 (2019).

487 Kim, D. Y., Stefanoski, S., Kurakevych, O. O. & Strobel, T. A. Synthesis of an open-framework allotrope of silicon. *Nat Mater* **14**, 169-173, doi:10.1038/nmat4140 (2015).

488 Liu, Z. *et al.* All-Silicon Topological Semimetals with Closed Nodal Line. *J Phys Chem Lett* **10**, 244-250, doi:10.1021/acs.jpclett.8b03345 (2019).

489 Lee, E., Kim, R., Ahn, J. & Yang, B. Higher-Order Band Topology and Corner Charges in Monolayer Graphdiyne. *arXiv:1904.11452* (2019).

490 Xu, C. & Balents, L. Topological superconductivity in twisted multilayer graphene. *Physical review letters* **121**, 087001 (2018).

491 Cao, Y. *et al.* Correlated insulator behaviour at half-filling in magic-angle graphene superlattices. *Nature* **556**, 80 (2018).

492 Chebrolu, N. R., Chittari, B. L. & Jung, J. Flatbands in twisted bi-bilayer graphene. *arXiv preprint arXiv:1901.08420* (2019).

493 Jorio, A. & Cançado, L. G. Raman spectroscopy of twisted bilayer graphene. *Solid State Communications* **175**, 3-12 (2013).

494 Guinea, F. & Walet, N. R. Electrostatic effects, band distortions, and superconductivity in twisted graphene bilayers. *Proceedings of the National Academy of Sciences* **115**, 13174-13179 (2018).

495 Yin, L.-J. *et al.* Landau quantization and Fermi velocity renormalization in twisted graphene bilayers. *Physical Review B* **92**, 201408 (2015).

496 Isobe, H., Yuan, N. F. & Fu, L. Unconventional superconductivity and density waves in twisted bilayer graphene. *Physical Review X* **8**, 041041 (2018).

497 Thomson, A., Chatterjee, S., Sachdev, S. & Scheurer, M. S. Triangular antiferromagnetism on the honeycomb lattice of twisted bilayer graphene. *Physical Review B* **98**, 075109 (2018).

498 Kim, K. *et al.* Tunable moiré bands and strong correlations in small-twist-angle bilayer graphene. *Proceedings of the National Academy of Sciences* **114**, 3364-3369 (2017).

499 Morell, E. S., Correa, J., Vargas, P., Pacheco, M. & Barticevic, Z. Flat bands in slightly twisted bilayer graphene: Tight-binding calculations. *Physical Review B* **82**, 121407 (2010).